

# Modeling and Control of the Current Density Profile in Tokamaks and its Relation to Electron Transport

THÈSE N° 4360 (2009)

PRÉSENTÉE LE 3 AVRIL 2009  
À LA FACULTÉ SCIENCES DE BASE  
CRPP ASSOCIATION EURATOM  
PROGRAMME DOCTORAL EN PHYSIQUE

ÉCOLE POLYTECHNIQUE FÉDÉRALE DE LAUSANNE

POUR L'OBTENTION DU GRADE DE DOCTEUR ÈS SCIENCES

PAR

Costanza ZUCCA

acceptée sur proposition du jury:

Prof. G. Gremaud, président du jury  
Dr O. Sauter, directeur de thèse  
Dr T. Goodman, rapporteur  
Dr X. Litaudon, rapporteur  
Prof. H. Zohm, rapporteur



ÉCOLE POLYTECHNIQUE  
FÉDÉRALE DE LAUSANNE

Suisse  
2009



# Version abrégée

La densité de courant dans le plasma d'un tokamak influence fortement les phénomènes de transport. Par conséquent, sa compréhension et son contrôle représentent des défis cruciaux pour la fusion thermonucléaire contrôlée. Parmi les nombreux thèmes relatifs aux études du transport, trois sujets ont été abordés dans le cadre de cette thèse : premièrement, la modélisation de l'évolution de la densité de courant dans des décharges avec des Barrières de Transport Interne électroniques (eITBs) dans le Tokamak à Configuration Variable (TCV); deuxièmement, l'étude de la diffusion du courant et l'inversion des propriétés du transport électronique observées lors des décharges de Swing ECCD sur TCV; troisièmement, l'analyse du façonnage de la densité de courant obtenu par ECCD local, lui-même réalisé par une variante améliorée du système EC pour le contrôle des dents de scie et des scénarios à cisaillement renversé dans le Réacteur Expérimental Thermonucléaire International (ITER).

Le travail dédié à l'étude des eITBs sur TCV a été réalisé dans le but d'identifier quels paramètres principaux, directement liés à la densité de courant, ont un rôle important dans l'amélioration du confinement créé lors des scénarios avancés. Dans ce contexte, la densité de courant doit être modélisée, puisqu'il n'y a aucune mesure disponible sur TCV pour l'instant. Puisque le modèle Rebut-Lallia-Watkins (RLW) a été validé sur les plasmas chauffés par chauffage ohmique sur TCV, le facteur d'échelle correspondant a souvent été utilisé pour la mesure de l'amélioration du confinement sur TCV. Les nombreuses simulations interprétatives réalisées sur différentes décharges de TCV ont montré que l'amélioration du confinement thermique, caractérisée par le facteur  $H_{RLW}$ , augmente linéairement avec la valeur absolue du cisaillement magnétique minimal à l'extérieur de  $\rho > 0.3$ , où  $\rho$  indique une coordonnée radiale normalisée. Ces investigations, réalisées avec le code de transport ASTRA, ont confirmé l'observation générale, formulée suite à des

études précédentes, que la formation de la barrière de transport est corrélée au cisaillement magnétique renversé. Ceci a été confirmé dans tout les cas étudiés, indépendamment des différents schémas de chauffage et de génération de courant utilisés. Il a été observé que l'amélioration du confinement avec un cisaillement magnétique négatif est graduelle mais constante, et qu'elle ne dépend pas des valeurs spécifiques du facteur de sécurité. Par conséquent, la transition de confinement standard à confinement amélioré s'avère lisse, bien qu'elle soit très rapide.

Le système flexible EC sur TCV n'a pas seulement permis d'obtenir une forte amélioration du confinement global pour produire des régimes eITB, mais il a également permis la réalisation d'études de transport sur des plasmas caractérisés par un bas confinement, dans lesquels le profil du cisaillement magnétique a été modifié localement autour du rayon de déposition. Par exemple, l'injection périodique et alternée de co- et counter-ECCD a été réalisée sur TCV, au cours de la même décharge de plasma, en maintenant la même quantité de puissance EC totale. Un tel schéma de chauffage est le principe des expériences de Swing ECCD, qui ont été initialement réalisées à des rayons de déposition proches de l'axe dans le plasma, pour maximiser l'absorption de la puissance EC, et donc la variation du cisaillement magnétique. Le code ASTRA, interfacé avec les données expérimentales et avec le code CQL3D pour le calcul des sources de chauffage et de courant EC, a à nouveau été utilisé comme outil fiable pour l'analyse de transport et la planification de nouvelles expériences. Les simulations ont montré les effets du Swing ECCD sur le cisaillement magnétique et sur le profil de température électronique autour du rayon auquel les ondes EC sont absorbées. Il résulte que les deux profils sont modulés à la même fréquence que celle du Swing ECCD. De plus, la variation maximale du cisaillement magnétique est indépendante des modèles de transport utilisés pour les simulations, ce qui met en évidence la robustesse de la modélisation. En outre, les résultats numériques ont motivé des expériences ultérieures réalisées à des rayons de déposition EC se trouvant plus hors axe. Les expériences sont en accord qualitatif avec des prédictions gyrocinétiques récentes pour lesquelles une inversion des propriétés de transport a lieu lorsque la valeur du cisaillement magnétique est plus grand.

Le but de l'étude liée au projet ITER a été d'analyser les capacités d'une variante possible

du système EC qui a été proposé récemment dans l'intention d'optimiser l'action combinée des Lanceurs Upper et Equatorial EC, et donc de permettre un domaine d'opération plus large pour ITER. Cette variante ne modifiera pas les buts principaux pour lesquels le système EC d'ITER a été conçu, c'est à dire la stabilisation des Modes Tearing Néoclassiques (NTMs) et de l'instabilité des dents de scie. Ceci est essentiel et a été analysé attentivement dans cette étude. En plus de permettre une excellente performance dans le contrôle des NTMs et de la période des dents de scie, la variante suggérée ouvre le chemin vers une exploitation plus vaste des ondes EC pour ITER. Le design de base actuel d'ITER prévoit que tout les lanceurs EC ne produisent que du co-ECCD. La modélisation numérique réalisée a montré que la possibilité de produire du counter-ECCD, avec une seule série de miroirs équatoriaux parmi les trois, offre un meilleur contrôle de la densité de courant du plasma. Le counter-ECCD pourrait aussi être balancé avec du co-ECCD pour fournir du chauffage EC pur, sans courant net produit. Ceci constituerait un avantage supplémentaire si l'on trouvait que les ondes EC sont nécessaires pour assister la transition L-H pendant le ramp-up du plasma. L'importance de la perte d'une série de miroirs équatoriaux en co-ECCD a été estimée comme étant négligeable, parce que la différence entre co-ECCD produit en utilisant 20MW du Lanceur Equatorial hors axe, ou co-ECCD produit par 2/3 du Lanceur Equatorial et 1/3 du Lanceur Upper est faible. Par conséquent, l'analyse présentée apporte une forte démonstration du gain substantiel en flexibilité si la variante du système EC d'ITER était acceptée comme design de base.

**Mots clés :** plasma, fusion, modélisation, densité de courant, transport, amélioration du confinement, eITB, TCV, ITER, EC, contrôle.

# Summary

The current density in tokamak plasmas strongly affects transport phenomena, therefore its understanding and control represent a crucial challenge for controlled thermonuclear fusion. Within the vast framework of tokamak studies, three topics have been tackled in the course of the present thesis: first, the modelling of the current density evolution in electron Internal Transport Barrier (eITB) discharges in the Tokamak à Configuration Variable (TCV); second, the study of current diffusion and inversion of electron transport properties observed during Swing Electron Cyclotron Current Drive (Swing ECCD) discharges in TCV; third, the analysis of the current density tailoring obtained by local ECCD driven by the improved EC system for sawtooth control and reverse shear scenarios in the International Thermonuclear Experimental Reactor (ITER).

The work dedicated to the study of eITBs in TCV has been undertaken to identify which of the main parameters, directly related to the current density, played a relevant role in the confinement improvement created during these advanced scenarios. In this context, the current density has to be modeled, there being no measurement currently available on TCV. Since the Rebut-Lallia-Watkins (RLW) model has been validated on TCV ohmic heated plasmas, the corresponding scaling factor has often been used as a measure of improved confinement on TCV. The many interpretative simulations carried on different TCV discharges have shown that the thermal confinement improvement factor,  $H_{\text{RLW}}$ , linearly increases with the absolute value of the minimum shear outside  $\rho > 0.3$ ,  $\rho$  indicating a normalized radial coordinate. These investigations, performed with the transport code ASTRA, therefore confirmed a general observation, formulated through previous studies, that the formation of the transport barrier is correlated with the magnetic shear reversal. This was, indeed, found to be true in all cases studied, regardless of the different heating and current drive schemes employed. The increase of confinement with the negative

magnetic shear was observed to be gradual, but constant, and did not depend on specific values of the safety factor. Therefore, the transition from standard to improved confinement appeared to be smooth, although it can be very fast.

The flexible EC system in TCV allowed us to attain strong global confinement improvement to produce eITB regimes. It also permitted us to perform transport studies on plasmas characterized by low confinement, in which we modified the magnetic shear profile, locally, around the deposition location. For instance, alternate and periodic injection of co- and counter-ECCD within the same plasma discharge has been realized on TCV, while maintaining the same amount of total input EC power. Such a heating scheme has been the basis of Swing ECCD experiments, which were initially carried out using nearly on-axis EC deposition locations in the plasma, in order to maximize the EC power absorption, and therefore the magnetic shear variation. ASTRA, interfaced with the experimental data and the CQL3D code for the computation of the EC heating and current drive sources, has again been used as a reliable tool for transport analysis and planning of new experiments. The simulations have pointed out the effects of Swing ECCD on the magnetic shear and on the electron temperature profile around the radius at which the EC waves are absorbed. Both profiles turned out to be modulated at the same frequency as the frequency of the Swing ECCD. Moreover, the maximum magnetic shear variation has been observed to be independent of the transport models used for the simulations, therefore underlying the robustness of the modeling. Additionally, the numerical results have motivated further experiments with more off-axis EC deposition, which were found roughly in agreement with recent gyrokinetic predictions, according to which, at higher positive values of the magnetic shear, an inversion of the transport properties should occur.

The aim of the study regarding the ITER project has been to analyse the capabilities of a possible variant of the EC system, recently proposed with the intent to optimize the combined action of the Upper and Equatorial EC Launchers and, therefore, to allow a broader operational domain for ITER. This variant will maintain the main goals for which the ITER EC system has originally been designed, namely the stabilization of Neoclassical Tearing Modes (NTMs) and of the sawtooth instability. This is a necessary feature that has been carefully analyzed in the present study. Besides allowing excellent

performance in controlling NTMs and the sawtooth period, the suggested variant paves a way for further exploitation of EC waves for ITER. The present ITER base-line design has all EC launchers providing only co-ECCD. The performed numerical modeling has shown that the possibility to drive counter-ECCD with one of the three rows of equatorial mirrors offers greater control of the plasma current density. The counter-ECCD may also be balanced with co-ECCD to provide pure EC heating, with no net driven current. This would be an additional asset if EC waves were found to be needed to assist the L-H transition during plasma ramp-up. The overall decrease in co-ECCD, by turning one row to counter-ECCD, is estimated to be negligible, because the difference between full off-axis co-ECCD using all 20MW from the Equatorial Launcher or co-ECCD driven by 2/3 from the Equatorial Launcher and 1/3 from the Upper Launcher is small. Therefore the latter analysis provides, in our opinion, a strong evidence of the substantial gain in flexibility if the suggested variant of the ITER EC system were accepted as the base-line design.

**Keywords:** plasma, fusion, modeling, current density, transport, improved confinement, eITB, TCV, ITER, EC, control.



# Contents

<b>1</b>	<b>Introduction</b>	<b>2</b>
<b>2</b>	<b>Modeling of the current density</b>	<b>11</b>
2.1	Introduction . . . . .	11
2.2	Brief overview on the safety factor measurement . . . . .	13
2.3	Equilibrium reconstructions . . . . .	14
2.3.1	Tokamak equilibrium . . . . .	14
2.3.2	The LIUQE equilibrium code . . . . .	15
2.3.3	The CHEASE equilibrium code . . . . .	17
2.3.4	Computation of the inductive and bootstrap current components . . . . .	18
2.3.5	Computation of the external current drive component . . . . .	19
2.3.6	Profile mapping and iteration . . . . .	20
2.4	1- $\frac{1}{2}$ D transport modeling . . . . .	21
2.4.1	Interpretative time evolution simulations . . . . .	21
2.4.2	Predictive transport simulations . . . . .	22
<b>3</b>	<b>Modeling of TCV electron Internal Transport Barriers</b>	<b>23</b>
3.1	Introduction . . . . .	23
3.2	The TCV tokamak . . . . .	24
3.3	Experiments on eITBs in TCV . . . . .	24
3.4	Simulations of eITBs . . . . .	26
3.4.1	eITBs with small ohmic perturbations applied after the barrier formation . . . . .	26
3.4.2	eITBs with small ohmic perturbations applied before the barrier formation . . . . .	32

3.4.3	Time evolution of eITBs obtained with different heating schemes . . .	34
3.4.4	Improving the eITBs simulations accuracy by experimental con- straints . . . . .	40
3.4.5	Negative central current density . . . . .	44
3.4.6	Comparison of steady state ASTRA $q$ profiles with CHEASE reconstructions . . . . .	45
3.5	Summary and conclusions . . . . .	48
<b>4</b>	<b>Swing ECCD discharges on TCV</b>	<b>50</b>
4.1	Introduction . . . . .	50
4.2	Swing ECCD experiments on TCV . . . . .	51
4.2.1	Experimental set-up . . . . .	51
4.2.2	Electron transport properties . . . . .	52
4.2.3	Scan in the deposition location . . . . .	56
4.3	Modeling of Swing ECCD . . . . .	58
4.3.1	Rebut-Lallia-Watkins model . . . . .	60
4.4	Numerical results . . . . .	61
4.4.1	Interpretative simulations results . . . . .	62
4.4.2	Predictive simulations results . . . . .	67
4.4.3	Discussion on the numerical results . . . . .	71
4.5	MHD activity in Swing ECCD discharges . . . . .	74
4.6	Summary and conclusions . . . . .	75
<b>5</b>	<b>Modeling of ITER discharges with local EC Heating &amp; Current Drive</b>	<b>78</b>
5.1	Introduction . . . . .	78
5.2	ITER external heating systems and main design parameters . . . . .	79
5.3	Present ITER EC system . . . . .	79
5.3.1	Description . . . . .	79
5.3.2	Limitations . . . . .	83
5.3.3	Revised variant . . . . .	84
5.4	ITER operation scenarios . . . . .	88
5.4.1	Inductive operation (Scenario 2) . . . . .	92
5.4.2	Hybrid operation (Scenario 3) . . . . .	93

5.4.3	Steady-state operation (Scenario 4-type I and II)	94
5.5	Model for ITER discharges	96
5.6	Control of the sawtooth instability	99
5.6.1	Self-consistent transport results	100
5.6.2	Equilibrium results	102
5.7	Advantages of counter-ECCD	108
5.7.1	Pure EC Heating	108
5.7.2	Unvaried control capabilities of the system	112
5.7.3	Increase of the $q$ profile control	114
5.8	Current redistribution	118
5.9	Summary and conclusions	119
<b>6</b>	<b>Conclusions and perspectives</b>	<b>122</b>
6.1	Conclusions	122
6.2	Perspectives	123
<b>A</b>	<b>ITER model implemented in ASTRA</b>	<b>125</b>
A.1	Ion densities	125
A.2	Impurity radiation	125
A.3	NBI heating	126
A.4	Gas puff neutrals	127
A.5	Transport model (based on ITER-H98(y,2) empirical scaling)	127
A.6	Particle transport	128
A.7	Heat sources and sinks	128
A.8	Sawtooth oscillations	128
<b>B</b>	<b>Fits for the ITER EC profiles</b>	<b>129</b>

# Chapter 1

## Introduction

An important branch of plasma physics research aims at demonstrating that thermonuclear fusion is a valid option for generating power, in the long term future, in an environmentally, politically and economically suitable way [1], [2], [3]. Fusion is a nuclear reaction in which light nuclei fuse together to form heavier ones: during this process, a very large amount of energy can be released. However, a substantial energy barrier must be overcome before the electrostatic repulsion between the positively charged protons in the light nuclei is, eventually, surpassed by the attractive nuclear force, which is strong at close distances. Only then fusion can occur. The condition for fusion reactions to reach ignition, i.e. to self-sustain, has been mathematically formulated by Lawson [4]: it states that the value of the energy confinement time ( $\tau_E$ , measured in s) multiplied by the ion density ( $n$ , in  $\text{m}^{-3}$ ) at the required temperature ( $T$ , in keV) must exceed a certain constant. In formulae:

$$n T \tau_E > 3 \times 10^{21} \text{m}^{-3} \text{ keV s.}$$

Fusion reactions power the Sun and other stars: in the core of a star, the gravitational force of its very large mass provides sufficient high attraction to ignite the reaction. The mass needed, however, is so great that this sort of confinement, the so-called gravitational confinement, is impossible on Earth. In man-made controlled fusion, the only two confinement principles achievable are inertial and magnetic confinement. Inertial confinement is realized by applying a rapid energy pulse to the surface of a pellet of fusion fuel, causing it to simultaneously implode and heat to very high pressure and temperature, so as to reach high enough fusion rate. Magnetic confinement is, instead, realized by generating a high

toroidal magnetic field so that the charged ions of fusion fuel follow spiral orbits around the field lines. The fuel is therefore trapped along the field lines and can be heated to the required temperature by external means. At these temperatures, well above typical ionization energies (13.6 eV in the hydrogen case), the fusion reactants exist in the plasma state.

The tremendous progress made in the field of fusion research over the last decades has recently led the fusion community to take the next step; it has, together, designed the International Thermonuclear Experimental Reactor (ITER) experiment [5]. The aim of ITER is to show that fusion can be used to generate electrical power, and to gain the necessary data to design and operate the first electricity-producing plant. This project is the result of long negotiations between most of the industrialized countries in the world, including the European Union, Japan, India, the People's Republic of China, the Republic of Korea, the Russian Federation and the USA. ITER will be constructed in Europe, at Cadarache, in the South of France.

The ITER project is based on the tokamak concept, which is nowadays regarded as the most advanced concept for a prototype thermonuclear fusion reactor, based on magnetic confinement. A tokamak is constituted by a large toroidal vacuum vessel, inside which the plasma is created, and a set of coils to generate the required magnetic field. The plasma is stabilized and confined by a strong toroidal magnetic field of several tesla [T], generated by the toroidal coils. A poloidal component of the magnetic field is produced by an electrical current, the so-called plasma current,  $I_p$ , flowing toroidally in the plasma. This current is induced via transformer action. The primary coil of the transformer is a solenoid located around the central column of the device, with a time-varying current,  $I_{OH}$ , circulating inside it, whereas the toroidal plasma acts as the secondary winding of the transformer. The last component of the tokamak's total magnetic field,  $B$ , is a vertical magnetic field generated with the purpose to stabilize the instability arising from the presence of the plasma current. Besides stabilizing the plasma, the vertical magnetic field allows to reach various shapes of the plasma cross-section.

As mentioned in the previous paragraph, the operation of a tokamak requires the generation of the plasma current. The inductive component of the plasma current,  $j_{ohm}$ , is

driven by the toroidal electric field,  $E_{\parallel}$ , induced by the variation of the magnetic flux through the torus. In other words,  $\langle j_{\text{ohm}} B \rangle = \sigma_{\text{neo}} \langle E_{\parallel} B \rangle$ , where  $\sigma_{\text{neo}}$  is the so-called local neoclassical conductivity, due to charged particles collisions, and the “ $\langle . \rangle$ ” symbol denotes a magnetic flux surface average that will be clarified in Sec. 2.1. The toroidal current is also a source of plasma heating through Joule’s effect; since the resistivity scales as  $T_e^{-3/2}$  ( $T_e$  being the electron temperature), i.e. the plasma approaches an ideal conductor with increasing temperature, ohmic heating loses its effectiveness as the temperature increases. In addition, magnetic induction makes the tokamak operation unavoidably pulsed. Thus, in order to obtain a steady state continuous plasma discharge, the plasma current must be sustained by a combination of non-inductive external drives and by the self-generated pressure-driven (bootstrap) current that spontaneously occurs in tokamak plasmas, described in Sec. 2.3.4.

Reactor-relevant, non-inductive, external, current drive methods are applied either by injecting neutral particles with directed momentum into the plasma, or by accelerating plasma particles by electromagnetic waves, so that they carry the current. The former scheme consists of the injection of high energy, high power beams of hydrogen or deuterium atoms. Due to collisions between the neutral atoms and the plasma ions, Neutral Beam Injection (NBI) methods produce a beam current of fast charged particles circulating around the torus. The slowing down of these fast particles by collisions with the plasma electrons then causes the electrons to drift toroidally, producing a plasma current. To date, most of NBI systems have been based on the neutralization of positive ions, but, for ITER, a negative-ion based (nNBI) system is being designed since, at the high energy required (1MeV), the neutralization of positive ions becomes very inefficient. ITER’s nNBI system will consist of two beams of 16.5MW each, for a nominal total input NBI power of 33MW, driving a total current of few MA [6]. NBI systems have been successfully installed on many tokamaks, such as the Joint European Torus (JET) [7], DIII-D [8], ASDEX Upgrade (AUG) [9], and the Japan Torus-60 Upgrade (JT-60U) [10].

A number and variety of electromagnetic wave-based current drive schemes exist. Along with the NBI system, three other methods have been chosen as heating and current drive schemes for ITER: the momentum-carrying traveling Lower Hybrid (LH) waves and the

negligible momentum-content Ion and Electron Cyclotron (IC and EC) waves. LH waves, at a frequency between the IC and EC frequencies (a few GHz), have a component of the electric field parallel to the magnetic field ( $k_{\parallel} \neq 0$ ), so they can accelerate electrons moving along the field lines because they deliver net toroidal momentum to the electrons. The momentum absorption by electrons leads to the production of current that is destroyed only by collisions with the ion species. In other words, LH waves drive the current when they are absorbed by Landau damping on the plasma electrons: the electrons absorbing the power have a velocity parallel to the magnetic field lines which matches the wave phase velocity and these synchronous electrons ‘surf’ along the wave.

Contrary to NBI and LH methods, IC and EC waves transfer little parallel momentum: absorption increases the perpendicular energy of the plasma species (ions or electrons). However, charged particles that already have a parallel velocity in the required direction can be heated preferentially. As a consequence, in the vicinity of the fast particles, the velocity distribution function is deviated from a Maxwellian distribution. The fast tail particles slow down with a reduced collisional frequency because the increase of particle energy makes the collisional frequency decrease ( $\nu \sim T_e^{-3/2}$ ), therefore the asymmetry at higher energy is smoothed out on a slower time-scale. In other words, the preferentially heated particles collide less often than do those particles circulating in the opposite toroidal direction, resulting in a net electric current. Significant steady state current can be sustained by radio frequency methods in a tokamak, provided the particle distribution has a substantial runaway tail. The ranges of frequencies for IC and EC waves are, respectively, a few tens of MHz and about a hundred GHz. For detailed reviews of electromagnetic wave-based current drive methods, see, for instance, [11], [12], [13], [14].

Finally, the spontaneously-generated bootstrap (BS) current [15] is a current parallel to the magnetic field that is driven by the radial pressure gradient through the pressure anisotropy it generates in an inhomogeneous magnetic field. It is, therefore, originated by a typically neoclassical effect. In a toroidal geometry, a certain amount of particles (of the order of the square root of the tokamak inverse aspect ratio,  $\sqrt{r/R}$ , where  $r$  and  $R$  are, respectively, the plasma minor and major radii) are subject to magnetic mirror reflection because of the  $1/R$  dependence of the toroidal magnetic field. These trapped particles’

gyro-centers execute nearly closed orbits with a finite width (the so-called banana width) in the low field region. In presence of a pressure gradient, and due to collisions and friction with passing particles, an asymmetry in the velocity distribution arises, leading to the generation of a parallel current. The latter is usually referred to as the banana current and is the origin of the bootstrap current. To date, the bootstrap current plays an important role in optimizing advanced tokamaks. In TCV recent discharges, for instance, the bootstrap fraction has reached 100%, with the current being entirely self-generated by the plasma in stationary conditions of intense EC Resonance Heating (ECRH) [16], [17].

Besides making the operation continuous by fully replacing the inductive component of the plasma current, auxiliary non-inductive current drive is useful to control instabilities and to optimize confinement, by tailoring the current density profile. Confinement properties reflect the capability of the plasma to retain the physical quantities that are provided externally to maximize its reactivity - such as energy, particle content and angular momentum. In a tokamak, the most significant energy losses are due to the radial transport of particle and thermal energy, occurring from the core to the edge of the vacuum vessel. Since collisions between the plasma particles cannot explain the large losses experimentally observed, the mechanism of radial transport is yet to be completely understood. This “anomalous” radial transport is the object of extensive investigation, because its reduction has a strong impact on the performance of a tokamak. The investigation can be approached from different perspectives, both experimentally, analytically, and numerically.

A key ingredient in the understanding of anomalous transport is the profile of the plasma current density, since it was found to have a complex relationship with a variety of externally controlled quantities, such as the density, toroidal magnetic field, plasma shape and the net input power. Indeed, the importance of the plasma current density arises from its strong link to plasma confinement properties. The understanding and knowledge of the plasma current density are therefore crucial for performing operation. This has motivated us to provide accurate modeling of the current density in a tokamak under different operational regimes. The performed modeling included both equilibrium simulations (for steady state, interpretative reconstructions) and transport simulations (for time evolution and



predictive reconstructions). The validation of these two methods involved comparison, at steady state, of the reconstructed profiles and, when possible, use of experimentally measured constraints, such as Magneto Hydro Dynamic (MHD) activity, profile flattening, etc.

The first goal of this work has been to analyze the behavior of the current density under different heating conditions in the Tokamak à Configuration Variable (TCV). TCV is a medium size tokamak located at the Centre de Recherches en Physique des Plasmas (CRPP) in the Ecole Polytechnique Fédérale de Lausanne (EPFL). It was originally designed to investigate the effect of plasma shape on confinement and stability. The powerful and flexible EC Heating and Current Drive (ECH&CD) system of TCV allows transport studies which can address specific issues of great relevance for fusion research. Given the large shape flexibility of the TCV plasma cross-section, an accurate description of its magnetic surface configuration is required. Moreover, since the auxiliary heating sources provide a very strong external current drive, an accurate description of the plasma current density evolution is imperative.

Transport modeling on TCV has been devoted to the simulation of the plasma current density evolution in discharges characterized by either low or improved electron confinement (respectively L-mode and advanced scenarios). L-mode experiments with modulation of ECCD, at constant total input power, have been performed at TCV, with the purpose to decouple the contributions of heating oscillations from those of the current density oscillations. In these Swing ECCD discharges, co- and counter-ECCD have been alternatively injected at a constant frequency, maintaining the same absolute value of total driven current and the same power deposition profile. Swing ECCD therefore resulted in modulations of the magnetic shear as well as of the central electron temperature (and thus, by implication, of confinement properties). The work concerning Swing ECCD plasmas aimed at providing a better insight into the magnetic shear profile modification in these discharges. Modeling of the plasma current density has been carried out with the ASTRA transport code [18] - employed in both predictive and interpretative modes - with two magnetic shear-dependent models for the calculation of the electron energy diffusion coefficient. In this context, the modulation of local current density was identified as the only actuator for the transport properties modifications. This analysis has confirmed the

synergy between electron transport and magnetic shear, both of which were modulated around the EC deposition region. The study has also allowed to completely decouple the effects of the current profile modification from those of a slight plasma heating misbalance, or a non-constant plasma elongation, which have proved to be key concepts at the basis of Swing ECCD as well as a rather delicate experimental issue. Moreover, the numerical results have validated a previous simplified modeling of the current density modulation based on electrodynamics calculations [19].

Improved electron confinement scenarios in TCV are usually associated with the presence of a so-called electron Internal Transport Barrier (eITB) [20] and references therein, characterizing a region in the plasma with an extremely strong pressure gradient. The dynamics regulating transport barriers and confinement improvement are rather complex mechanisms. Previous experimental observations suggested that a better confinement level was achieved through magnetic shear reversal [21], therefore the present transport modeling addressed the role played by the local value of the magnetic shear for the confinement improvement. The numerical results have shown that the formation of the barrier is associated with a negative magnetic shear, in all cases studied, regardless of the different heating and current drive schemes used. The local confinement improvement is consistent with a linear and continuous increase as the local magnetic shear decreases. In particular, the detailed simulations carried out excluded the existence of an effect peculiar to specific values of the safety factor,  $q$ , such as to low order rational  $q$  surfaces, as had been hypothesized on other machines.

Another goal of this work has been to provide the transport code ASTRA with a comprehensive model to supply the ITER device with self-consistent numerical tools for prediction of plasma response under specific heating conditions. The application of this model has allowed us to provide realistic studies of the profile control capabilities which are expected on ITER by injecting very localized EC into the plasma. Recently, much effort has been made to improve the EC system on ITER (which dates back to several years ago) in order to cover adequately the largest possible operational domain, taking into account the most recent results from other machines, the better understanding of EC waves capabilities, and the different current drive characteristics delivered by the two types of

EC antennas used in ITER [22]. It should be stressed that the EC system should assist reaching the main operational scenarios useful for the control and physics studies that will be carried out in ITER. For this reason, minor modifications to the present design have recently been suggested [93]. The final part of this thesis has therefore addressed the impact of this revision on the device performance, based on realistic plasma response and control. The numerical modeling has shown that the variant EC system would provide considerable advantages concerning the control of instabilities and the plasma confinement improvement, with neither losses in reliability, nor in physics applications. Given the benefits of such a revision and the urge to supply ITER with the most flexible and performant EC system, we therefore recommend that the presented variant be taken as the new base-line design.

## Outline

In **Chapter 2**, we first define important physical quantities, such as safety factor and magnetic shear, and the notion of flux surface average. After a brief overview on experimental methods to measure the safety factor profile, we then introduce the concept of equilibrium reconstructions for tokamak plasmas. We highlight the conceptual differences between equilibrium reconstructions using different equilibrium codes available for TCV, namely LIUQE and CHEASE. We also present in detail a method for the most accurate, steady state reconstruction available at TCV, which includes various steps and iterations. In the second part of the chapter, we present the modeling based on 1- $\frac{1}{2}$ D transport tokamak codes for predictive simulations. This includes the diffusion equations describing transport quantities and magnetic flux time evolutions, followed more closely by what is implemented in the ASTRA code. The transport modeling is necessary for both time evolution, interpretative reconstructions, and predictive simulations.

**Chapter 3** contains the results of the interpretative modeling of TCV advanced scenario discharges. After a brief description of the TCV device, we analyze a typical TCV advanced scenario discharge obtained with strong EC heating and current drive. Afterwards we present the modeling results of various TCV discharges, performed with different heating schemes. The modeling results allow us to draw important conclusions about the

confinement improvement, and to better understand the formation and sustainment of the so-called electron Internal Transport Barriers (eITBs) in TCV. ASTRA is used here as an indirect diagnostic tool for both steady-state and time-evolution simulations. We then discuss how it is possible to simulate the current density profile for the case in which a current hole appears in the plasma centre and the consequences of this approximation. To check the accuracy of the ASTRA equilibrium, a comparison between the steady state transport simulations and the LIUQE equilibrium reconstructions is shown.

**Chapter 4** is devoted to the analysis of the relation between the magnetic shear and plasma confinement properties during Swing ECCD discharges in TCV. We first provide a description of the experimental set-up used, followed by the analysis of discharges with Swing ECCD. Then we present the ASTRA modeling, which has been carried out in both interpretative and predictive ways, using two different transport models: the Rebut-Lallia-Watkins model and a modified version of the former model. The modeling underlines the importance of the value of the local magnetic shear for the transport modulation (induced by the shear oscillation itself) and is in agreement with predictions from gyrokinetic theory.

**Chapter 5** presents the detailed ASTRA modeling of ITER discharges with local EC heating and current drive. Following a brief introduction to the ITER tokamak, we present the differences between the present ITER EC system and a variant recently proposed to cover a wider range of physics applications. A description of ITER's foreseen operational scenarios, and of the transport model used, is then included. An analysis is presented on the efficiencies in controlling the sawtooth period, of the present and variant EC systems, based on both steady state and transport simulations. The results are explained on the basis of a theoretical study of the key parameters for the control of the sawtooth instability. Unlike at present, the variant of the EC system foresees counter-ECCD; therefore, a detailed study of the increased control capabilities of the safety factor profile are shown, with emphasis on the gain in flexibility without major losses in control.

In **Chapter 6** conclusions are drawn on the work presented and proposals for future work are outlined.

# Chapter 2

## Modeling of the current density

### 2.1 Introduction

In Chap. 1, the detailed description of the plasma current density distribution,  $j$ , in a tokamak has been identified as an important issue, since it appears to be a key factor in transport theory. As a result of the superposition of the three components of the magnetic field in a tokamak (toroidal, poloidal and vertical), the magnetic topology is such that the field lines are frozen into an ensemble of nested magnetic flux surfaces,  $\Psi(R, z)$ , as shown in Fig. 2.1. In the ideal Magnetohydrodynamics (MHD) approximation, the pressure in the plasma is constant along the magnetic field lines. Likewise, the lines of the current density lie on the magnetic surfaces. Each magnetic surface characterizes a radial labeling, generally indicated with  $\rho$  and defined, for instance, as the square root of the normalized poloidal magnetic flux,  $\rho = \sqrt{\Psi_{\text{norm}}}$ . This allows one to plot all the relevant physical quantities as 1D, flux-surface-averaged profiles, often indicated by the symbol “< . >”. In this way, flux surfaces are defined by the simple equation  $\rho(R, z) = \text{const}$ .

The blue, magenta and green color-coded field lines in Fig. 2.1 circle the torus with a finite angle (pitch angle) relative to the toroidal direction. Thus, along a field line, also the quantity  $q = d\Phi/d\Psi$  is constant (with  $\Phi$  and  $\Psi$  respectively being the toroidal and poloidal magnetic fluxes). This quantity, strongly linked to the current density, is the safety factor and is so called because of the role it plays in determining stability. The value of  $q$  is determined by the ratio of toroidal to poloidal turns of the magnetic field line. One can observe a difference in the pitch angles of the magnetic field lines with

respect to a horizontal plane. This additional property is defined as magnetic shear,  $s = r/q \, dq/dr$ , and is strongly interlinked with both the distribution of the plasma current inside the plasma and that of the safety factor. The specific values and the radial

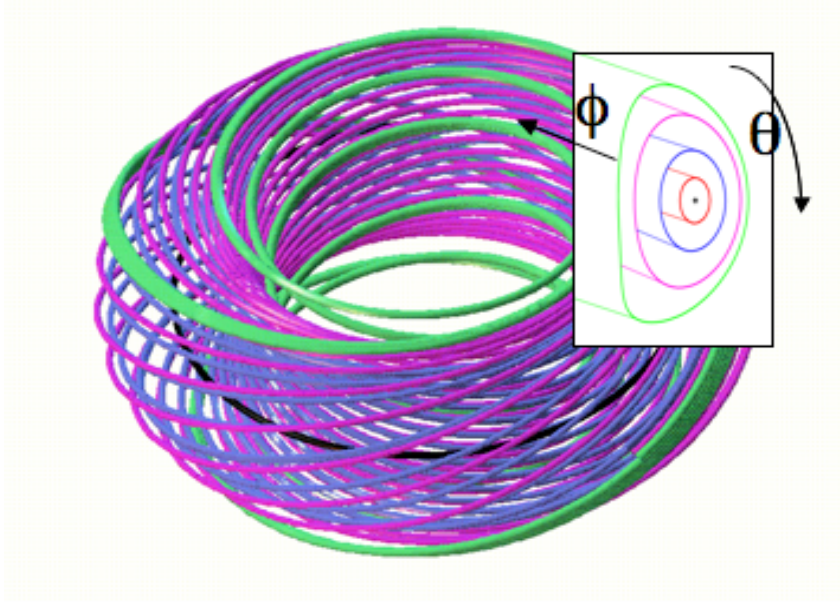


Figure 2.1: *The magnetic field lines topology of a tokamak.  $\phi$  and  $\theta$  respectively indicate the toroidal and poloidal angles.*

distribution of  $q$  are critical parameters in theories of the sawtooth oscillation [23]; other MHD instabilities such as, for instance, Neoclassical Tearing Modes [24] (NTMs); as well as for the formation of transport barriers [25]. Therefore, much effort is being expended to accurately determine this quantity. For a large aspect-ratio tokamak of circular cross-section, the approximated relation between  $q$  and the toroidal component of  $j$ ,  $j_\phi$ , can be shown to be [26]:

$$q(r) = \frac{r^2 B_\phi}{R_0 \mu_0} \frac{1}{\int_0^r j_\phi(r') r' dr'} = \frac{2\pi r^2 B_\phi}{R_0 \mu_0 I(r)}, \quad (2.1)$$

where  $r$  is the minor radius,  $B_\phi$  is the toroidal magnetic field (essentially a constant),  $R_0$  is the tokamak major radius,  $\mu_0$  is the vacuum permeability and  $I(r)$  is the toroidal current inside the flux surface  $r$ .

## 2.2 Brief overview on the safety factor measurement

The measurement of the current density, or alternatively of the safety factor, is a challenging topic in plasma physics research, and a number of differing diagnostics have been developed in order to provide accurate information on this fundamental quantity. Among these diagnostics, some of the most successful are Motional Stark Effect (MSE), polarimetry and soft X-ray diagnostics.

MSE diagnostics [27], [28] have been installed on several machines, and are recognized as the main method to determine the magnetic pitch angle from which the poloidal field and the  $q$  profile can be derived. The Stark effect is the shifting and splitting of spectral lines of atoms due to the presence of an external static electric field. An MSE diagnostic relies on the availability of a sufficiently powerful neutral beam injector and on a sensitive detection system to determine polarization. With an appropriate choice of beam species and velocity and of geometry, this effect can be used to determine the magnetic pitch angle in the plasma.

Polarimetry has also been successfully installed on different machines [29]. It produces a laser beam with a linear polarization rotating at the Far Infrared (FIR) frequency. A linearly polarized wave can be decomposed into right and left circularly polarized components, which have different refractive indices. This difference gives rise to a rotation of the polarization vector known as the Faraday effect. When crossing the plasma, the laser beam is split into various channels and one reference channel. Faraday rotation angles relative to the reference detector are therefore measured by standard coherent detection. The application of inversion algorithms yields the local electron density and the distribution of the poloidal magnetic field of the tokamak. From the distribution of this magnetic field the profiles of the safety factor and the current density are calculated. A new, 10-channel FIR polarimeter is currently being installed on TCV [30], with an expected sensitivity able to accurately measure the profiles of the current density and of the safety factor for typical scenarios with negative magnetic shear.

Several MHD instabilities occur in tokamaks, and they can be detected and studied by measuring their magnetic perturbations. By making measurements at different toroidal and poloidal locations, the structure of magnetic perturbations can be determined, along with their amplitude and frequency. The structure may obviously vary across the radius, for instance there may be an  $m = 1, n = 1$  in the centre and an  $m = 3, n = 1$  struc-

ture near the plasma edge (where  $m$  and  $n$  are, respectively, the poloidal and toroidal mode numbers). Fast magnetic diagnostics and tomographic systems are available on most tokamaks to measure and identify MHD modes and islands. For instance, TCV is equipped with a set of fast and spatially well resolved diagnostics, including Soft X-ray (XTOMO [31] and DMPX [32]) and magnetic coils, and these measurements can be used to constrain the reconstructed or simulated current density profile [33], as will be shown in Sec. 3.4.4.

It should be noted that the main aim of the diagnostics described above is to provide valuable profile input to equilibrium reconstruction codes (such as EFIT [34] on DIII-D and JET, or LIUQE [35] on TCV), since it has been shown that the constraints imposed by experimental data can substantially improve the reliability of the equilibrium procedure [35]. While the diagnostics have been constructed and used successfully, they are technically challenging and/or the interpretation of the data is difficult to automate in actual experimental situations. Therefore, the  $q$  profile data are not routinely available. Given the difficulty in obtaining precise and reliable measurements of the safety factor, it is clear that numerical modeling of this quantity is still imperative. Moreover, in many tokamaks, such as TCV, there are no measurements of the current density profile presently available, thus the modeling is the only way of describing this key quantity.

## 2.3 Equilibrium reconstructions

### 2.3.1 Tokamak equilibrium

The ideal MHD equilibrium equation for an axisymmetric toroidal plasma can be written as a differential equation for the poloidal magnetic flux function  $\Psi$  and is known as Grad-Shafranov equation [36]. It contains two arbitrary functions of the poloidal magnetic flux,  $p(\Psi)$  and  $T(\Psi)$ , respectively related to the pressure and current profiles, and takes the form:

$$\Delta^* \Psi = -\mu_0 R j_\phi = -\mu_0 R^2 p'(\Psi) - T(\Psi) T'(\Psi), \text{ with } \Delta^* \Psi = R \frac{\partial}{\partial R} \frac{1}{R} \frac{\partial \Psi}{\partial R} + \frac{\partial^2 \Psi}{\partial z^2}, \quad (2.2)$$

$p' = dp/d\Psi$  and  $T' = dT/d\Psi$ . The problem of equilibrium is therefore reduced to knowing the solution of Eq. 2.2,  $\Psi(R, z)$ . The equilibrium is partly determined by the externally imposed conditions such as the total current, the applied toroidal magnetic field



and heating, and partly by the plasma behavior. The pressure profile is governed by the transport properties and by instabilities, and the current profile is principally determined by the temperature-dependent electrical conductivity, by the external current drives and by the bootstrap current.

Equilibrium reconstruction is of crucial importance for the correct interpretation of experimental data in modern tokamaks. In principle, the reconstruction of the plasma equilibrium alone is sufficient to determine the safety factor profile. The main division among the many existing equilibrium codes is between fixed and free boundary codes. Fixed boundary codes require as an input the detailed description of the plasma boundary, that is, the values of the spatial coordinates of the so-called Last Closed Flux Surface (LCFS). Free boundary codes, instead, calculate more realistically the plasma equilibrium response from the descriptions of the currents flowing within the poloidal and vertical magnetic coils. In the next two Sections, a brief description of the two equilibrium codes mainly used in the course of this work will be given.

### **2.3.2 The LIUQE equilibrium code**

As previously mentioned, among the main features that make TCV unique in its category are its coil system and vacuum vessel, which allow to produce plasma cross sections with very flexible shapes [37]. On the other hand, having such an extended flexibility of magnetic configurations, the problem of TCV equilibrium reconstruction requires specifically built numerical tools. The free-boundary LIUQE code [35] is traditionally employed for the equilibrium reconstruction of TCV experimental discharges because it was one of the very first codes developed with the purpose of solving extremely shaped equilibria, as in the case of the large variety of TCV cross sections. Strictly speaking, on TCV it provides the first equilibrium reconstruction over which all measured local quantities are then mapped in order to obtain magnetic flux surface averaged profiles for the subsequent ease of data analysis. A rapid and accurate determination of the magnetic flux coordinates is highly desirable and a number of free boundary equilibrium codes have been adapted to very shaped equilibria, exhibiting large elongations or extreme triangularities. These codes mainly differ in the numerical method employed for the solution of the equilibrium problem. Among them, we mention EFIT [34], DINA [38], ESC [39], SPIDER [40], and TSC [41].

LIUQE finds a solution to the Grad-Shafranov equation, with arbitrary source functions, such that the measurements are reproduced as well as possible. More specifically, the two source functions,  $p'$  and  $TT'$ , are expressed as a linear combination of arbitrary basis functions  $U_i(\Psi)$  and  $V_j(\Psi)$ :

$$p'(\Psi) = \sum_{i=0}^{N_p} a_i U_i(\Psi), \quad (2.3)$$

$$T(\Psi)T'(\Psi) = \sum_{j=0}^{N_T} b_j V_j(\Psi), \quad (2.4)$$

where  $a_i$  and  $b_j$  are constants to be computed iteratively such as to obtain the best least-square fit to the measurements. The default measurements employed by LIUQE on TCV are magnetic measurements close to the vessel wall and a diamagnetic loop signal. The measured pressure profile can also be provided to the code input, in which case the reconstructions are usually referred to as kinetic equilibria. To improve the accuracy of the TCV equilibrium reconstruction, an interferometer/polarimeter is planned to be installed that will provide Faraday rotation measurements, as discussed in Sec. 2.1. Being based on a least squared method approximation, the accuracy of the LIUQE reconstruction can vary depending on the plasma scenario. For instance, in cases of non-monotonic safety factor profiles, the standard reconstruction methods [35], [42] do not perform satisfactorily, so the plasma flux surfaces and profiles are not determined accurately. An example is shown in Fig. 2.2, which illustrates three LIUQE reconstructions of the safety factor profiles obtained with various constraints imposed by the measurements, compared with the  $q$  profile resulting from a transport calculation in interpretative mode (which will be explained in Sec. 2.4.1). This can be explained by the fact that we are not using any experimental information on the (hollow) current profile, therefore there is no constraint whatsoever on the source function  $TT'$ , which highly influences the safety factor profile. Contrary to experimental evidence and theoretical predictions, the solution to which LIUQE then converges is typically that of a monotonic safety factor profile. For this reason, for extremely tailored plasmas it is necessary to rely upon other tools than LIUQE reconstructions of the current density profile.

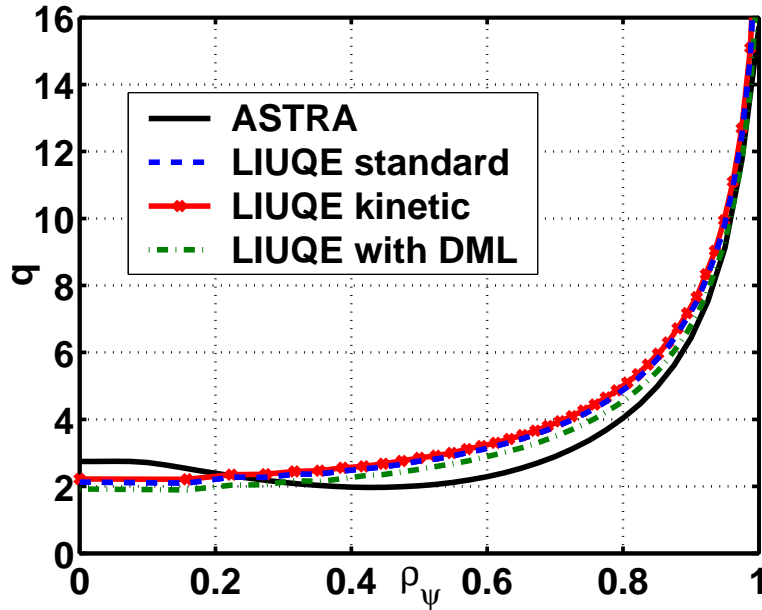


Figure 2.2: Comparison of various  $q$  profiles obtained with different methods for TCV discharge #25956. For this plasma,  $q$  is expected to be non-monotonic, as the ASTRA simulation correctly calculates. The LIUQE reconstructions fail to reproduce a non-monotonic  $q$ , even using other experimental constraints to improve the accuracy of the equilibrium, such as the DML signal or the pressure profile measurements.

### 2.3.3 The CHEASE equilibrium code

CHEASE [43] is a fixed boundary equilibrium code which solves the Grad-Shafranov equation in variational form, once the pressure and current density profiles, as well as the plasma boundary, are specified. During the present analysis, CHEASE has been employed in different ways to provide reliable equilibrium reconstructions. Firstly, it has been used to check the sufficient accuracy of the equilibrium calculation of the ASTRA transport code by extracting the input profiles of  $p'$  and  $TT'$  (and the plasma boundary) from the output of the transport code, as will be shown in Sec. 3.4.6. Secondly, it has allowed a preliminary steady-state analysis of the effect of local ECCD on ITER's standard, hybrid and advanced scenarios, as shown later in Chap. 5. Thirdly, it has been used within an iterative scheme for the accurate equilibrium reconstruction of TCV plasmas at steady state. In order to carry out this iterative scheme, which is exposed in Sec. 2.3.6, one needs to provide CHEASE with input profiles extracted from experimental data. The pressure

profiles have been obtained from the Thomson Scattering (TS) diagnostic for the electrons species and from the Charge eXchange Resonant Scattering (CXRS) diagnostic for the ion species (when available). As to the current flux function  $T$ , it has been prescribed in CHEASE in the form of the averaged parallel current density,  $I_{\parallel}$ . Indeed, CHEASE can treat three different options for specifying the current profile. The right hand side of Eq. 2.2, which is related to  $j_{\phi}$ , can be given by the  $p'$  function and any function between  $TT'$  (as in Eq. 2.2), or the surface-averaged toroidal current density  $I^*$ , or the averaged parallel current density  $I_{\parallel}$  [43]:

$$j_{\phi} = \frac{1}{R} \frac{C_0}{C_2} I^*(u) + \left( \frac{1}{R} \frac{C_1}{C_2} - R \right) p'(u), \quad \text{or} \quad j_{\phi} = \frac{1}{yR} I_{\parallel}(u) + \frac{1}{y} \left( \frac{1}{R} \frac{C_1}{C_2} - Ry \right) p'(u), \quad (2.5)$$

where  $y = 1 + C_2/C_3 T^2(u)$ , the  $C_i$  coefficients are surface integrals and  $u$  denotes a function of the normalized poloidal flux,  $u = u(\Psi_{\text{norm}})$ . The averaged parallel current density profile is given by the contribution of the various current density components described in Chap. 1 of this thesis. These components have been computed separately in the way described in the following Sections.

### 2.3.4 Computation of the inductive and bootstrap current components

In order to correctly evaluate the plasma conductivity and the bootstrap coefficients, and therefore the inductive and bootstrap current components respectively, it is necessary to employ neoclassical transport coefficients that account for different realistic magnetic equilibrium configurations and a large range of variation of three key parameters: the plasma aspect ratio, the plasma collisionality and the effective charge number,  $Z_{\text{eff}}$ . By solving the Fokker-Planck equation with the full collision operator, Refs. [44], [45] have provided a simple set of analytical fits for all the neoclassical transport coefficients, valid for arbitrary aspect ratio and collisionality in general realistic geometry. These formulas have then been used, along with the measured profiles  $T_e(\rho), T_i(\rho), n_e(\rho)$  and the measured scalar quantity  $Z_{\text{eff}}$ , to calculate the inductive and self-generated current components. Since in this context the parallel electric field is assumed to have a uniform radial profile, the calculations described here are a good approximation only at steady state.

It should be noted that modeling of the plasma effective charge profile from X-ray measurements is not carried out systematically on TCV. This could have an effect on the  $q$

profile, in particular if the inductive current component is large, but this is not the case for most of the simulations presented in this thesis. In TCV,  $Z_{\text{eff}}$  is typically estimated to vary between 1.5 and 4, and in the analysis that will follow in the next Chapters it was fixed to 3, unless differently specified. However,  $Z_{\text{eff}}$  not being precisely known, it is important to validate all the  $q$  profile reconstructions by performing sensitivity studies on the value of  $Z_{\text{eff}}$ , as will be shown below, for instance, in the discussion related to Fig. 3.16.

### 2.3.5 Computation of the external current drive component

On TCV, the external current drive is generated by injection of EC waves ( $j_{\text{cd}} = j_{\text{eccd}}$ ) with a non-zero toroidal angle. Modeling of the auxiliary heating in a tokamak is a delicate topic, which requires calculation of three crucial quantities: the location at which the injected waves are absorbed, the current drive efficiency and the current drive profile. The most accurate calculation of the ECCD current component in TCV is realized by the quasi-linear CQL3D code [46]. CQL3D solves the bounce-averaged Fokker-Planck equation for the electron distribution function in 3D (2D in the velocity space and 1D in the radial direction). For TCV discharges, CQL3D is coupled to the linear TORAY-GA [47] ray-tracing code, which determines the ray paths with the cold plasma dispersion relation. Different processes occurring in the plasma are taken into account by CQL3D, therefore a number of terms appear in the Fokker-Planck equation to be solved: the relativistic Coulomb collisions operator, the DC wave electric field operator, the RF quasi-linear diffusion operator (arising from quasi-linear wave-particle interaction) and finally the radial particle diffusion operator, which was shown to have a major role in EC wave-driven experiments in TCV [48], [49].

Radial electron diffusion on TCV has recently been linked in eITBs to radial electron heat diffusion [50]. Therefore, in this work the particle diffusion coefficient,  $D_r$ , has been chosen to be proportional to the electron heat diffusion coefficient,  $\chi_e$ . The following proportionality between these two diffusion coefficients was assumed:  $D_r = D_0 \chi_e$ .  $\chi_e$  has been evaluated from the experimental profiles with power balance considerations. The proportionality parameter  $D_0$  has been adjusted to match the total driven current to the experimentally inferred value, i.e. from  $I_{\text{eccd}} = I_p - I_{\text{bs}} - I_{\text{ohm}}$ , where  $I_{\text{bs}}$  and  $I_{\text{ohm}}$  are calculated using the measured profiles, the formulas in Refs. [44], [45] and assuming

steady state ( $E_{\parallel} = V_{\text{loop}}/2\pi R_0 = \text{const}$ , where  $E_{\parallel}$  and  $V_{\text{loop}}$  respectively are the parallel electric field and loop voltage).

Besides CQL3D, the computation of auxiliary heating in TCV discharges is sometimes carried out with the TORAY-GA code. However, it is worth pointing out that a linear code, as TORAY-GA is, assumes the current drive efficiency independent of the total injected power, therefore it fails in accurately calculating the ECCD component for TCV, typically slightly underestimating it. The other reason why a quasi-linear code becomes necessary, besides the effect of radial diffusion, is because of the large amount of EC power available on the relatively small volume of the machine, which renders the EC power density of TCV one of the highest worldwide.

### 2.3.6 Profile mapping and iteration

In Fig. 2.3, the CHEASE loop for the equilibrium reconstruction at steady state using measured and calculated quantities as input is shown. An initial equilibrium, typically the one from the LIUQE reconstruction, is used to map the measured local quantities, such as Thomson Scattering and CXRS (when available) data, to provide  $p'$  as an input to CHEASE. This initial equilibrium is also used to compute the current components separately with the methods described in the previous Sections, and therefore obtain  $I_{\parallel}$ , which is employed as an input to CHEASE, too (see Eq. 2.5). CHEASE is then run and provides a new, complete equilibrium, which is used to map again the experimental data and compute the current components. The scheme is iterated until convergence is reached, typically two or three iterations are sufficient.

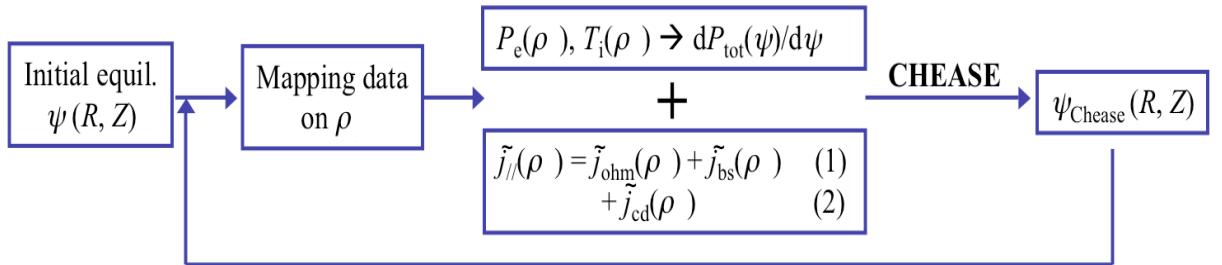


Figure 2.3: *Iterative process for an accurate steady state equilibrium reconstruction on TCV, using CHEASE.*

## 2.4 1- $\frac{1}{2}$ D transport modeling

Transport in tokamaks is usually described by means of particle and heat diffusion. For instance, for each plasma species the local energy diffusion coefficients in a plasma determine the temperature profiles obtained for a given heating power density profile. Various core transport codes are available, such as CRONOS [51], PRETOR [52], JETTO [53], BALDUR [54]. In the course of this thesis, transport simulations have been carried out with the tokamak simulation ASTRA code [18]. ASTRA solves a basic set of four 1D flux-surface-averaged diffusive equations, along with a variety of modules describing additional heating, current drive and other non-diffusive processes in tokamak plasmas. The equilibrium reconstruction is self-consistently ensured by a 2D fixed-boundary 3-moment equilibrium solver which solves the Grad-Shafranov equation and updates the magnetic flux surfaces. Axisymmetric geometry and quasi-neutrality are assumed, and equilibria are up-down symmetric.

In this work, two separated simulating schemes have been adopted while using ASTRA, which will be referred to as steady state and transient simulations, depending on whether the modeled regime of the discharge is a steady state or a transient phase. In other words, the first group is provided with one set of experimental profiles (for one chosen time only, or rather profiles averaged over the steady state period), thus allowing to reach a true steady state, i.e. the final state of the run has a uniform residual radial loop voltage profile. The second type of simulations use, instead, experimental profiles that are updated every time step, with a linear interpolation in-between experimental profiles, thus spanning the entire time evolution of the current density profile.

Another distinction that should be made in the various transport simulating schemes employed in this thesis is between interpretative and predictive simulations, whose principles are detailed in the two following Sections.

### 2.4.1 Interpretative time evolution simulations

Interpretative transport modeling is peculiar in the sense that it does not employ a theory-based transport model, but rather uses the experimentally measured profiles to solve the poloidal flux diffusive equation. Indeed, since the experimental profiles of  $T_e$ ,  $T_i$  and  $n_e$  are imposed, the only diffusive equation employed in the present modeling can be formally

written as:

$$\frac{\partial \psi}{\partial t} = \frac{V'}{2\pi\rho} \tilde{E}_{\parallel} = \frac{V'}{2\pi\rho} \frac{\tilde{j}_{\parallel} - \tilde{j}_{\text{bs}} - \tilde{j}_{\text{cd}}}{\sigma_{\parallel}}, \quad (2.6)$$

where  $\tilde{E}_{\parallel}$ ,  $\tilde{j}_{\parallel}$ ,  $\tilde{j}_{\text{bs}}$  and  $\tilde{j}_{\text{cd}}$  are appropriate flux surface averaged quantities,  $\sigma_{\parallel}$  is the neo-classical conductivity,  $\rho$  is the radial label of the magnetic surface and  $V' = \partial V/\partial\rho$ ,  $V$  being the volume enclosed by the surface  $\rho$ .

In this context, ASTRA has been employed as an indirect diagnostic tool for the reconstruction of the  $q$  profile, there being no measurement presently available on TCV.

## 2.4.2 Predictive transport simulations

In this approach, equations for the time evolution of a large set of physical quantities describing the plasma, which can include  $T_e$ ,  $T_i$ ,  $n_e$ ,  $n_{\alpha}$ ,  $v_{\phi}$ ,  $\psi$ , must be solved self-consistently. These equations typically take the form:

$$\frac{1}{V'} \frac{\partial}{\partial t} (V'G) + \frac{1}{V'} \frac{\partial}{\partial \rho} \left( V' \langle \Gamma_G \cdot \nabla \rho \rangle_{\rho} \right) = \langle S_G \rangle, \quad (2.7)$$

where  $V' = \partial V/\partial\rho$ ,  $G = G(\rho(R, z), t)$  is one of the physical quantities mentioned above, and  $\Gamma_G$  and  $S_G$  indicate respectively the flux and the source corresponding to the physical quantity  $G$ . The equations are coupled to one another by several different physical mechanisms, so that the fluxes and sources of each physical quantity  $G$  in general depend on the other physical quantities as well. This is exhaustively explained in Ref. [55].

For the determination of the transport coefficients, predictive simulations make use of transport models, and the final results of the simulations strongly depend on the specific transport model adopted. In this thesis, a detailed description of the specific transport model used precedes each section containing the numerical results of the predictive investigation. However, the main aim of the present work is to obtain a prediction for the time evolution of the current density profile rather than an analysis of various transport models.



# Chapter 3

## Modeling of TCV electron Internal Transport Barriers

### 3.1 Introduction

Advanced regimes characterized by high core confinement, known as internal transport barriers (ITBs) [56], [57], have been achieved in many tokamaks. ITBs have been observed with a variety of different heating regimes, such as Lower Hybrid Current Drive (LHCD) [58] and Ion Cyclotron Resonance Heating (ICRH) [59] on Tore Supra, LHCD and ICRH on JET [60], Neutral Beam Injection (NBI) power on ASDEX Upgrade [9], EC Resonance Heating (ECRH) and NBI [8] on DIII-D, ECRH and ECCD on TCV [20], [61].

Improving the energy confinement time in scenarios compatible with steady state operation is one of the main goals of present tokamak research. Therefore ITBs are largely studied, since they allow to explore new territories for tokamak advanced operation. As a consequence, one of ITER's operational scenarios is planned to be an advanced one, with a plasma current of 9MA sustained by about 50% of bootstrap current, characterized by the presence of an ITB and improved confinement, allowing for a long, steady state pulse. This will be discussed in more detail in Chap. 5.

## 3.2 The TCV tokamak

TCV started operation in November 1992 and its program is based on flexible plasma shaping and heating for studies of confinement, transport and control [62]. The flexibility of its shaping and control systems, making TCV a unique research tool worldwide, is matched by that of its ECH and ECCD systems. The second harmonic frequency ( $f_{2ec} = 82.7\text{GHz}$ ) system consists of two clusters of three gyrotrons each, at a nominal power of 0.5MW per gyrotron, usually operating in X-mode polarization (X2) [63]. The third harmonic frequency ( $f_{3ec} = 118\text{GHz}$ ) system consists of three gyrotrons, for a total nominal power of 1.5MW, in X-mode polarization (X3) [64]. In the present work, we have considered only TCV discharges with ohmic and/or EC heating in X2. The principal design parameters of the machine are reported in Table 3.1.

Parameters	Symbol	Value
Major radius	$R_0$	0.88m
Minor radius	$a$	0.25m
Nominal aspect ratio	$A = R_0/a$	3.5
Vacuum vessel elongation	$\kappa_{\text{TCV}}$	3
Maximum plasma current	$I_p$	1.2MA
Maximum central magnetic field	$B_0$	1.5T
Discharge duration		<4s
Edge plasma elongation	$\kappa_a$	0.9 – 2.82
Edge plasma triangularity	$\delta_a$	(-0.8) – (+0.9)

Table 3.1: *Main TCV technical parameters.*

## 3.3 Experiments on eITBs in TCV

In TCV, electron ITBs (eITBs) typically occur in steady-state, fully-non-inductive discharges sustained by the EC Current Drive (ECCD) [21], [65], [61] and are characterized by extremely steep electron pressure gradients so that a high fraction of bootstrap current is generated [66]. The first stable plasmas in which all the current was driven by ECCD were successfully obtained in 1999 [67]. In 2002 fully non-inductive eITBs were

first created [68], and are now routine on the TCV machine and considerable control has been acquired on the formation and sustainment of the barrier.

In TCV eITBs, the current density is tailored to be maximum off-axis, with the resulting safety factor profile having a minimum off-axis. This scenario is referred to as negative or reverse magnetic shear and it is related to an enhanced confinement level attained by turbulence suppression mechanisms. Indeed, gyrokinetic simulations of TCV discharges [69] have assessed the stabilization of Trapped Electron Modes (TEM) in the presence of negative magnetic shear and Shafranov shift. These discharges have dominant auxiliary heating to electrons and turbulence is mainly due to TEM. Reverse shear thus represents an attractive option for advanced scenarios in tokamaks, because these can operate continuously with fully non-inductively sustained plasma current.

In the past TCV campaigns, many experiments have been conducted to elucidate the role of the current density profile evolution, from peaked to hollow, for the eITB formation and sustainment [21], [65], [61], particularly addressing the importance of a zero-shear surface occurrence for the existence of the barrier.

The operational recipe for generating the eITBs discussed in this chapter can be divided into the following different operational phases:

1. The discharge is initiated as a canonical ohmic discharge, at low plasma current ( $I_p \sim 100\text{kA}$ ), reaching a stationary ohmic phase after beginning of the flat-top, with constant total plasma current.
2. A dominant off-axis ECCD phase follows, typically with deposition between  $\rho = 0.2$  and  $0.5$ , which allows complete or partial replacement of the transformer-driven plasma current (in part because of the non-negligible contribution of the bootstrap current,  $I_{bs}/I_p > 50\%$ ).
3. The steady state eITB phase is observed, with an established barrier in the electron channel; it can be enhanced by providing ECH power deposited in the plasma center.
4. An additional fourth stage is sometimes dedicated to further tailor the total current density profile, with either prescribed surface voltage or co-/counter-ECCD on-axis.

Variations on this basic scenario are, of course, possible, and some of the most relevant ones will be discussed in the following subsections.

## 3.4 Simulations of eITBs

Recently, it has been stated that - in spite of the unavoidable uncertainties on the current density profile reconstruction - the reversal of the magnetic shear,  $s$ , is the key ingredient for TCV improved central electron confinement [21], [55]. In this Section, we present the investigation of the current density,  $j$ , and safety factor,  $q$ , profiles produced by specific heating and current drive in eITB scenarios. We have focussed our simulations on a recent series of dedicated experiments with various current perturbations. We have used the newly developed numerical scheme based on the coupling between the quasi-linear CQL3D Fokker-Planck code [46] and the ASTRA transport code [18], as described in Chap. 2. The main results have been published in Ref. [81], and are detailed here below.

### 3.4.1 eITBs with small ohmic perturbations applied after the barrier formation

Time traces of relevant physical quantities for some fully ECCD-sustained TCV plasmas are reported in Fig. 3.1. An eITB is formed by replacing the inductive current with co-ECCD generated by two off-axis beams, launched from the low-field side, at 0.4s, with toroidal angle  $\phi = 23^\circ$ , and a total power of approximately 0.9MW. At the same time, the current in the transformer coils,  $I_{OH}$ , is kept constant, yielding an edge loop voltage  $V_{loop} = 0$ . After 0.45s, a 0.45MW on-axis ECH beam is added, with  $\phi = 0^\circ$ , to form a more well-defined barrier. This steady-state fully-non-inductively-sustained phase is then perturbed, from 1.4s to the end of the pulse, by a small positive or negative surface loop voltage, resulting in the addition of centrally peaked ohmic current density contributions [21]. This modifies the total current density profile, shaping it to be centrally hollow or peaked depending on the sign of the perturbation, but leaves the power input essentially unchanged, since  $P_{ohm} \sim 3\text{--}6\text{kW} \ll 1.35\text{MW} = P_{EC}$ . Performing a fine, shot-to-shot scan of  $V_{loop}$  from -60 to +90mV, a smooth change in the barrier strength is observed, indicating a change of local confinement properties [21]. This is shown in Figs. 3.1b and 3.1c, which show, respectively, the central electron temperature,  $T_e(0)$ , and the Rebut-Lallia-Watkins scaling,  $H_{RLW} = \tau_{Ee}/\tau_{RLW}$  [70]. The latter is used because the RLW scaling predicts well the ohmic L-mode regime before the EC is turned on ( $H_{RLW} = 1$  for  $t \leq 0.4\text{s}$ ), and it is a good scaling for electron transport. These experiments have demonstrated the funda-

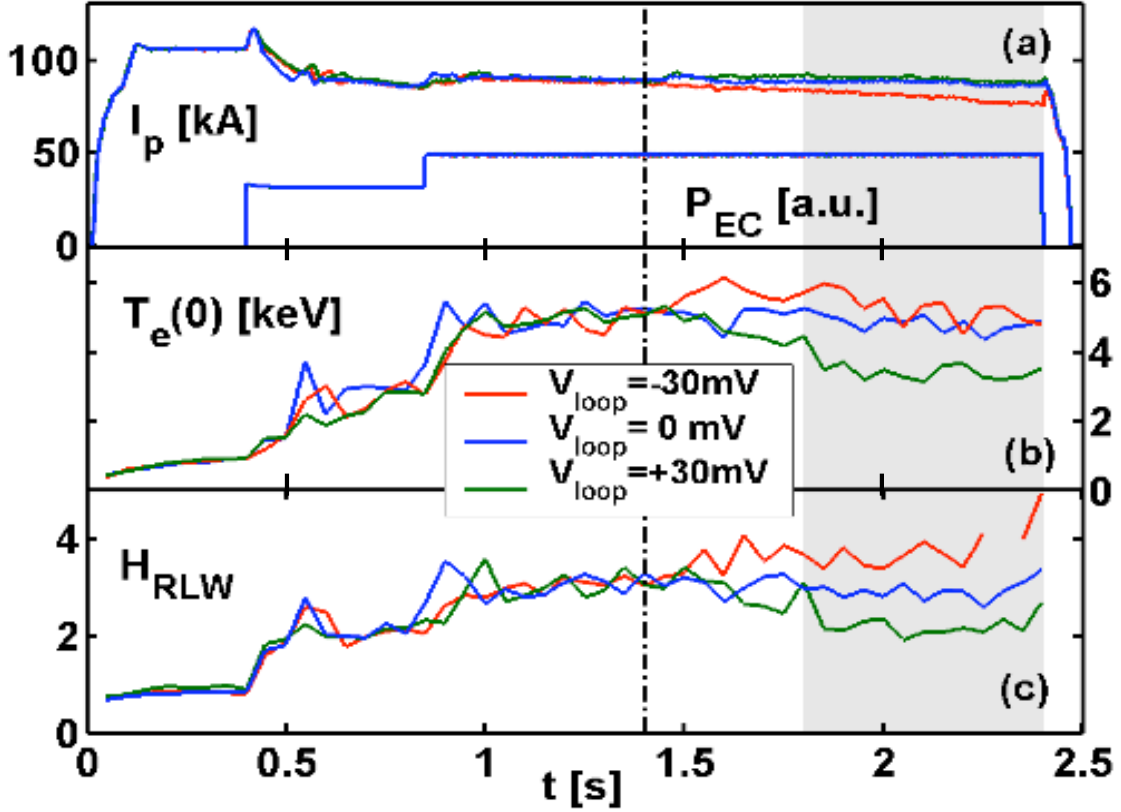


Figure 3.1: Time traces of (a) the plasma current and EC power, (b) the central electron temperature and (c)  $H_{\text{RLW}} = \tau_{Ee}/\tau_{\text{RLW}}$ , for a series of discharges with different constant slopes in the ohmic transformer current imposed at 1.4s (indicated by the black dash-dotted vertical line). The grey band indicates the steady-state phase. Here we show the cases with no perturbation throughout the discharge (#25956), with a +30mV (#25957) and -30mV perturbation (#25953).

mental role of the plasma current density tailoring as the main mechanism regulating the strength of the eITB. It is therefore interesting to know the range of variations of the  $j$  and  $q$  profiles in these experiments.

Steady state modeling of the total current density profile for the scenarios described above has been carried out. The aim of these simulations is to evaluate the  $j$  modification following the imposed  $V_{\text{loop}}$  variation and to find out whether such a perturbation, when all other actuators are held constant, can alone modify the degree of shear reversal. The experimental profiles of  $T_e$  and  $n_e$  at  $t = 1.4\text{s}$  are shown in Fig. 3.2, before any edge

perturbation is applied. The barrier is seen in both  $T_e$  and  $n_e$  because of the significant

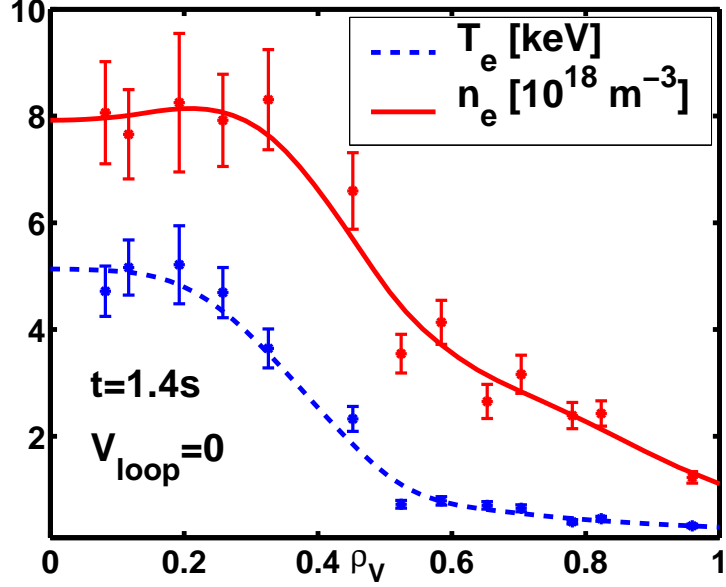


Figure 3.2: *Electron density (red) and temperature (blue) experimental profiles at  $t = 1.4s$  for a discharge without ohmic perturbation (#25956). Before any perturbation is applied, all discharges exhibit comparable profiles.*

thermodiffusive pinch contribution in the eITBs, leading to  $\frac{\nabla n_e}{n_e} \approx 0.45 \frac{\nabla T_e}{T_e}$  [50]. Fig. 3.3 shows the various current density components (solid lines) for this steady state scenario. Here, only the  $j_{bs}$  and the  $j_{eccd}$  currents are contributing to sustain the total current, since the inductive transformer is no longer active.  $j_{eccd}$  is rather flat in the center while  $j_{bs}$  has an off-axis peaked profile due to the large local gradients, as seen from Fig. 3.2, which typically occur in advanced scenarios with eITBs. The calculated  $q$  profile, also shown in Fig. 3.3, has  $q_0 = 2.75$  and  $q_{min} = 1.97$  at  $\rho_V = \sqrt{V_{norm}} = 0.34$ , indicating a slightly reversed shear. A sensitivity study of the value of  $Z_{eff}$  has shown that the shear is still slightly reversed even if the ECCD were only 80% of the inferred one; this provides the dashed profiles of Fig. 3.3. The inductive current component is strongly affected by the value of the effective charge, but here  $j_{ohm}$  is intrinsically zero,  $V_{loop}$  being zero. The value of  $Z_{eff}$  nevertheless influences the  $j_{eccd}$  calculation.

The simulation described above is consistent with the experimental pre-perturbation phase, during which a weak barrier is identified, as seen in Fig. 3.2. Successively, we have imposed on this simulated scenario (which is common to all discharges) a positive

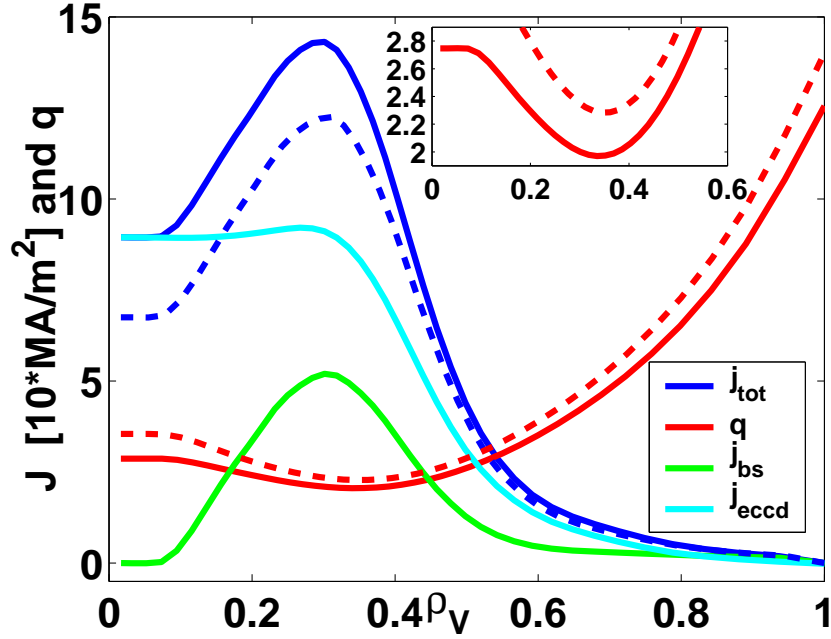


Figure 3.3: Radial profiles of the safety factor and current density components calculated by ASTRA using only experimental inputs and fixing the surface voltage to  $0mV$  (#25956). The dashed lines show the corresponding profiles obtained with 80% of ECCD, indicating that the  $q$  profile is still slightly non-monotonic.

or negative surface voltage,  $V_{loop} = \pm 30mV$ , which experimentally leads to the removal or enhancement of the barrier, respectively. All other profiles in the simulation are held constant in time, in particular  $n_e$  and  $T_e$ , i.e. the same as the standard (pre-perturbation) case. The different behaviors of the final states are clear from Fig. 3.4 (left), which shows the total current density profiles of the three cases and the ohmic components (small diagram) at  $t = 2s$ . In the first perturbed case, after penetration of the negative, centrally peaked  $j_{ohm}$  into the plasma, the total current density profile becomes significantly hollow, as also evident from the  $q$  profile, which is now characterized by  $q_{min} = 2.61$  at  $\rho_V = 0.39$  and  $q_0 > 10$  (red in Fig. 3.4, right plot). In the opposite case, the addition of a positively peaked inductive current density leads to a  $q$  profile which becomes monotonic ( $q_0 = q_{min} = 1.2$ , green line in Fig. 3.4, right plot).

The current redistribution time,  $\tau_{CRT}$ , has been simulated from the total current diffusion into the plasma to be about 100-200ms and is essentially proportional to the central value of the electron temperature ( $\tau_{CRT} \sim T_{e,0}^{3/2}$ ), as expected. The shear profiles are also

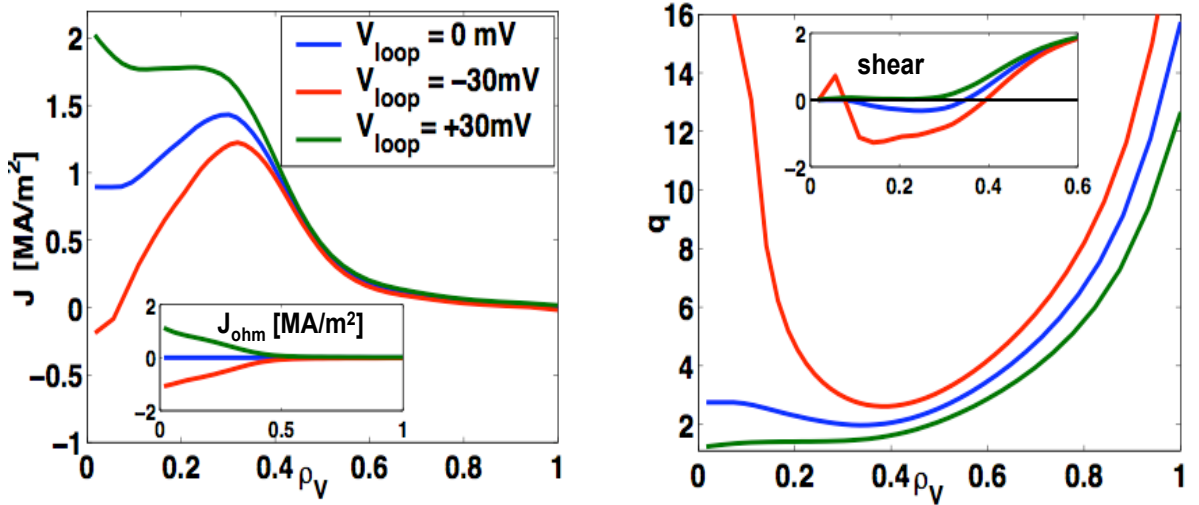


Figure 3.4: *Left plot: steady state current density profiles resulting from varying the surface voltage value from 0mV to +30mV or -30mV. The inductive current density profiles are also shown in the upper right plot, following the same  $V_{\text{loop}}$  variation. With a -30mV perturbation ( $I_{\text{ohm}} = -29\text{kA}$ ), the negatively peaked inductive current makes the current density profile become more hollow, whereas a +30mV perturbation ( $I_{\text{ohm}} = 31\text{kA}$ ) makes the current density profile essentially peaked. Right plot: steady state safety factor profiles resulting from varying the surface voltage value from 0mV to +30mV or -30mV. The shear profiles are also shown in the upper right plot, following the same  $V_{\text{loop}}$  variation. The  $q$  profile becomes monotonic or very reversed if one applies, respectively, a positive or negative perturbation.*

reported in Fig. 3.4 (top right diagram) for these three cases: when no perturbation is applied, the magnetic shear is negative inside  $\rho_V = 0.34$ , as already mentioned. After imposing a negative inductive current density, the depth of the shear reversal increases by about a factor 2, and the value of  $\rho(s = 0)$  is shifted slightly further off-axis by  $\Delta\rho = 0.05$ . This is consistent with the experimental observation that the foot of the barrier is located approximately at the same radial position, regardless of the barrier strength [21]. On the other hand, the co-ohmic perturbation results in a complete removal of the  $s \leq 0$  surfaces, and we essentially do not observe any confinement improvement anymore. The simulated profiles are consistent with the hypothesis that the presence of an eITB is related to the existence of an  $s \leq 0$  region in the plasma.

The experimental conditions following the imposed co-/counter-inductive perturbation



are subject to change, so the modeling presented so far simulates the current density profile diffusion assuming constant power and transport. These results are instructive because they provide the  $q_0$  and  $q_{\min}$  modifications that one can obtain with just such inductive current perturbations. Adding the relative effect on confinement, i.e. using the effective  $T_e$  and  $j_{\text{eccd}}$  profiles, provides an effect in the same direction as the corresponding ohmic perturbation. In the case when the applied voltage is negative, for instance, the final experimental  $T_e$  profile is steeper than that of the unperturbed state, because the barrier is stronger. This makes  $j_{\text{bs}}$  increase off-axis. Moreover the self-consistent  $j_{\text{eccd}}$  calculation also results in a more localized off-axis profile, since the local radial diffusion decreases with enhanced confinement, so that the  $j$  profile is even more hollow than that of Fig. 3.4, left. We have used the measured profiles averaged on the steady state period reached after the ohmic perturbation to model the self-consistent final states following the inductive scan [81]. When the voltage is negative, the self-consistent shear profile is still very reversed, although not significantly more extended in location or depth (solid green lines in the top diagram of Fig. 3.5, right). When the surface voltage is positive,

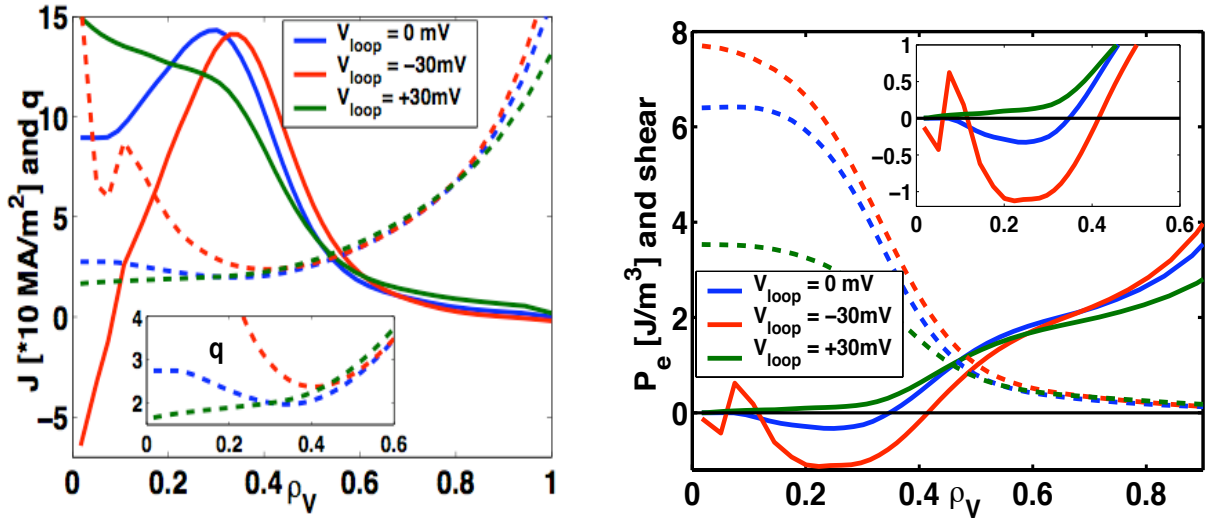


Figure 3.5: *Left plot: self-consistent total current density (solid) and safety factor (dashed) profiles at steady state for the inductive current scan. The small plot reports a zoom of the  $q$  profile. Right plot: self-consistent shear (solid) and electron pressure (dashed) profiles at steady state for the inductive current scan. The small plot reports a zoom of the shear profile.  $V_{\text{loop}} = 0$  case corresponds to TCV discharge #25956, +30mV to #25957 and -30mV to #25953.*

the self-consistent  $q$  profile is slightly more monotonic than that of the non-consistent use of the experimental profiles (Fig. 3.5 versus Fig. 3.4). Therefore these simulations are fully consistent with the fact that the confinement improvement is lost with monotonic  $q$  profiles. On the other hand, with more reverse  $q$  profiles, the barrier is more pronounced. If we define the foot of the barrier as the point where the local confinement starts to be improved, that is the location where there is a change in the local normalized gradient, we see that it is located outside  $q_{\min}$ . Therefore, when one says the  $s \leq 0$  is needed to sustain an eITB, it could also be  $s \leq 0.5$  or  $s \leq 1$ . Fig. 3.5 shows that  $s$  varies very rapidly outside  $q_{\min}$ : thus, the location of  $s = 0.5$  or  $s = 1$  are within the error bar of the determination of the foot of the barrier.

### 3.4.2 eITBs with small ohmic perturbations applied before the barrier formation

Various experiments have been devoted to investigate whether specific values of  $q$  are required for the confinement improvement, specifically a low-order rational  $q$  value. This is related not only to the eITB formation, but also to its sustainment. To carry on this study at TCV, a shot-to-shot scan of inductive current preceding the barrier formation has been done, aiming to span different low-order rational  $q$  surfaces during the formation and the sustainment of the eITB. Experimental time traces of three of these shots are plotted in Fig. 3.6, showing respectively the plasma current, the current in the ohmic transformer, the total EC power and the  $H_{\text{RLW}}$  factor. For the reference shot, #29867, the ohmic transformer current is held constant after 0.5s. Therefore, no surface voltage is applied while the power is ramped from 0.6s to 1.0s, nor during the following steady phase, during which the eITB is sustained. At steady state, the simulated value of  $q_{\min} i_s \sim 2.9$  for this reference case [81]. For the other shots of the scan, at  $t = 0.5$ s, either positive or negative constant surface voltage (about  $|30 \div 90|$ mV) is applied, so the measured  $I_p$  is varied from 90kA to respectively 102kA or 85kA. This is done while keeping the same EC power density for each shot. The difference in plasma current implies different  $q$  profiles at the time of the barrier formation and in the starting phase. Reconstruction of the safety factor has been done at steady state, to evaluate the variation of the minimum in  $q$  and thus to study the role it plays for the sustainment of the eITB. Simulation results can also be compared to those of shots presented in Sec.3.4.1, for which a comparable

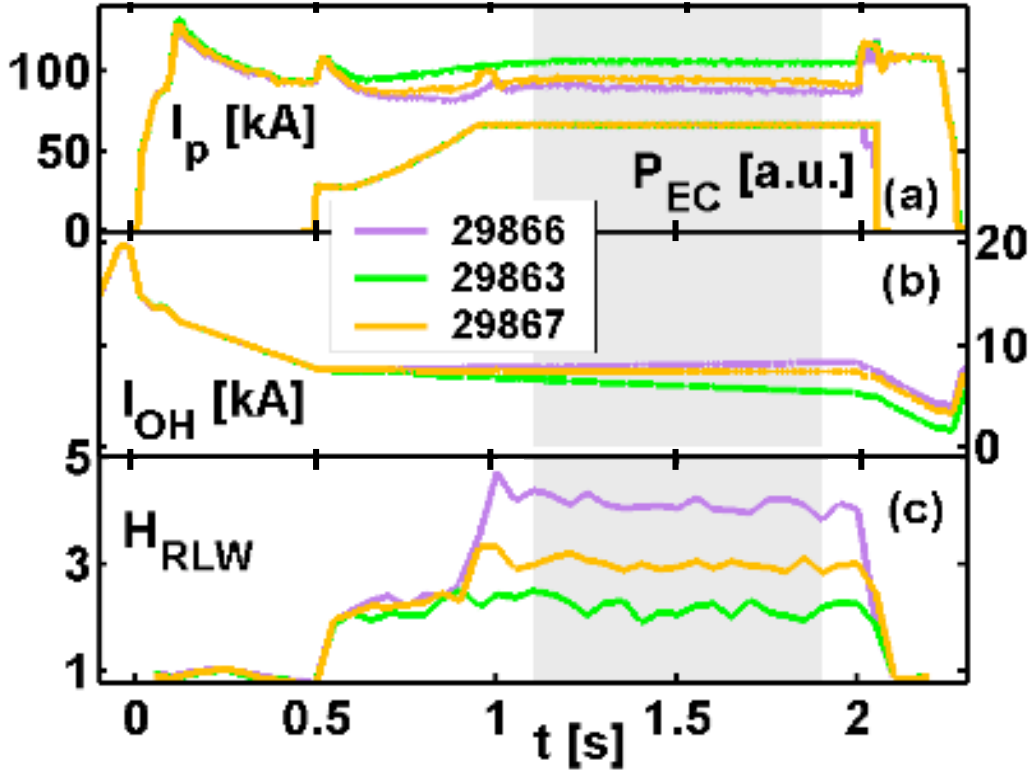


Figure 3.6: Time traces of (a) the plasma current, (b) the transformer current, (c) the total EC power and (d)  $H_{\text{RLW}} = \tau_{Ee}/\tau_{\text{RLW}}$  for three discharges with different inductive current before the barrier formation.

amount of central EC heating relative to the total deposited power was provided. The new discharges (#29863, 29866 and 29867) were sustained by two central beams in ECH and three off-axis beams in co-ECCD mode (for a total of 2.25MW), while those discussed in Sec. 3.4.1 (#25952, 25953, 25956 and 25957) were sustained by one on-axis gyrotron for heating and two gyrotrons aiming off-axis to drive the additional co-current (for a total of 1.35MW). The reconstructed safety factor and magnetic shear profiles for these two series of discharges are reported in Fig. 3.7, showing the  $q$  profiles at stationary state. The simulated values of  $q_{\text{min}}$  vary between 1.9 and 3.1 so that  $\Delta q_{\text{min}}$  is around unity. Taking into account uncertainties of the  $q$  profile reconstruction, at least two low order rational  $q$  surfaces were crossed during the scan of  $q_{\text{min}}$ . If any of these low order rational values were required for the formation of a barrier, the barrier should not be systematically triggered, but only occur during the evolution of certain discharges. One would expect to observe a

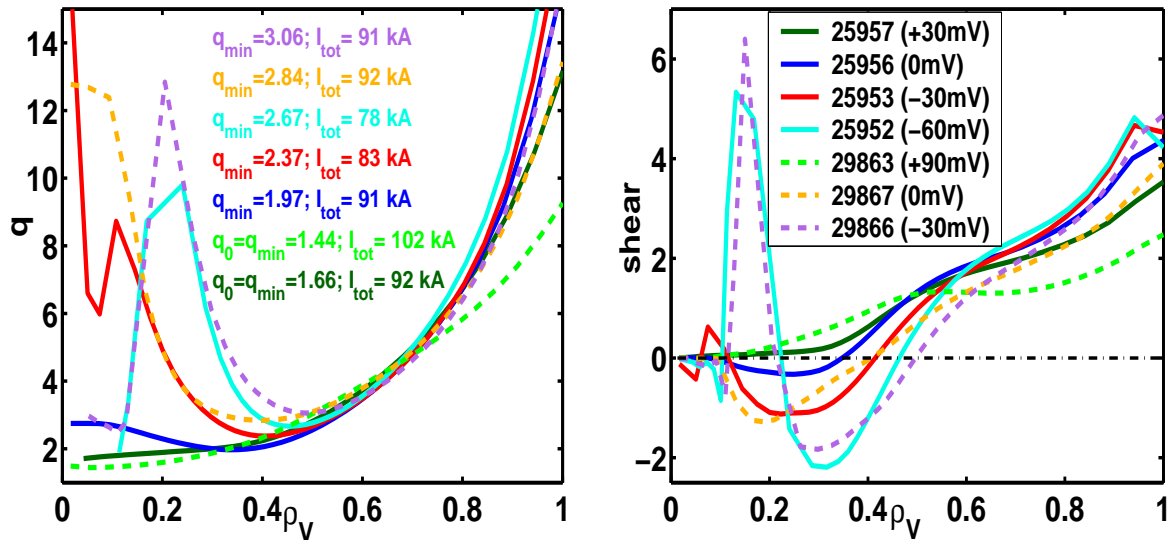


Figure 3.7: *Left: safety factor profiles of the two scans at steady state, showing that  $q_{\min}$  is varied between about 1.97 and 3.06. The plasma current values are also indicated. Right: corresponding shear profiles of the two scans from the ASTRA simulations.*

discontinuous behavior at some point in the scan. There seems to be no evident threshold behavior, neither in triggering nor sustainment, as inferred from the Soft X-ray traces and from the experimental  $H_{\text{RLW}}$  factor; the latter increases when the supplied surface voltage becomes more negative [65]. This implies that no particular  $q_{\min}$  is required for the performance improvement of TCV eITBs. For each shot, the corresponding  $H_{\text{RLW}}$  averaged over the steady state phase has been plotted as a function of the minimum value of the shear outside  $\rho_V > 0.3$  (Fig. 3.8), underlying once again a smooth and linear increase of the confinement properties with the more and more negative local shear. This is consistent with the conjecture that transport generally decreases steadily as shear is decreased from positive to negative values [71]. For positive values of  $s_{\min}$ ,  $H_{\text{RLW}}$  is systematically between 2 and 2.5 and no barrier is experimentally observed, consistent with earlier simulations showing  $H_{\text{RLW}} \sim 2$  for central heating [72].

### 3.4.3 Time evolution of eITBs obtained with different heating schemes

The analysis presented so far is a good tool for the understanding of the relation between the shear reversal and the existence and performance of a transport barrier, but it does not

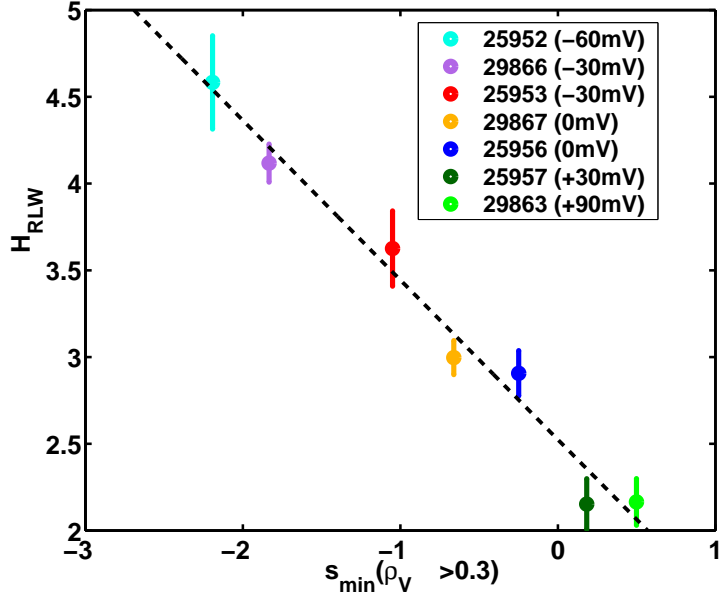


Figure 3.8:  $H_{\text{RLW}}$  as a function of the minimum value of the reconstructed magnetic shear outside  $\rho_V = 0.3$ . The linear growth indicates a smooth confinement improvement.

allow us to carry out the study of its triggering on the basis of temporal considerations. The eITB typically forms during the slow evolution of the plasma current density from peaked to flat and reversed. The speed of the barrier formation is rapid as compared to the current redistribution time [61]. Time traces of two TCV discharges are reported in Fig. 3.9, showing the plasma current and the total EC power supplied (Fig. 3.9a, respectively upper and lower traces), the central electron temperature (Fig. 3.9b) and the  $H_{\text{RLW}}$  factor (Fig. 3.9c). For one of the two plasmas (#21654, indicated as late ECH) an eITB is triggered in the same way as discussed previously in Fig. 3.1, by replacing the inductive current component with off-axis ECCD; after a few current redistribution times a central ECH beam is also introduced into the plasma to form a well established barrier and to broaden the profiles. For the second discharge (#21649, indicated as early ECH) the on-axis gyrotron in the heating mode has been added simultaneously to ECCD at  $t = 0.4\text{s}$ . With such an early/late ECH switch, the purpose is to investigate the influence of a central beam on the time-scale of the barrier formation. The final steady states of these two discharges are comparable. This can be seen from the experimental electron temperature and density profiles reported in Fig. 3.10 (lowest plots), which are obtained from the time average over the final steady state phase, [1.2, 1.6 s]. The other subplots

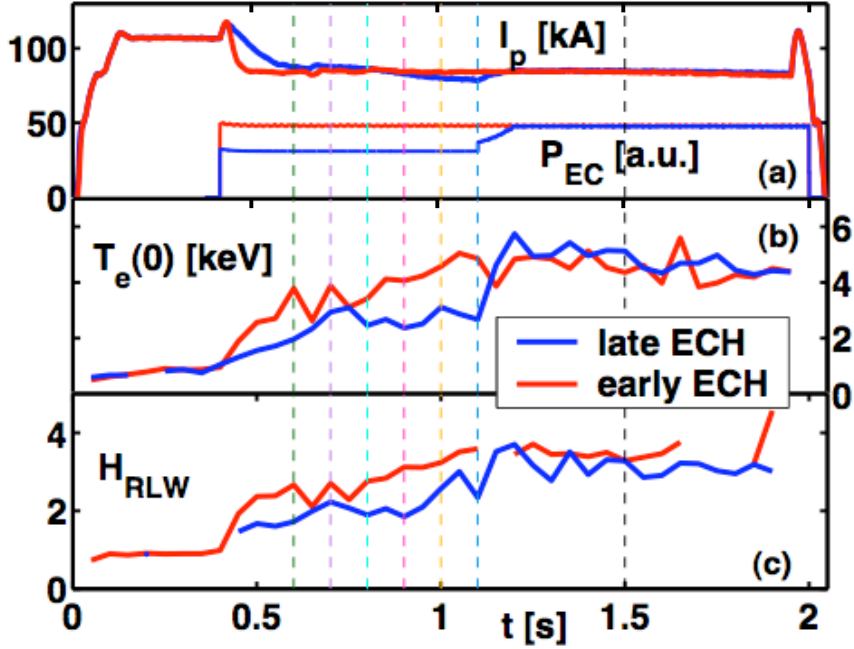


Figure 3.9: Time traces of (a) the plasma current and EC power, (b) the central electron temperature and (c)  $H_{\text{RLW}} = \tau_{Ee}/\tau_{\text{RLW}}$ , for two discharges with different heating timings. In the late ECH case (#21654), the ECH heating is gradually increased during the discharge, reaching full power at 1.2s, while in the early ECH case (#21649) the full power is injected all at once from 0.45s. The vertical dashed lines indicate the simulated times shown in Figs. 3.12 and 3.13.

of Fig. 3.10 show the profiles of  $T_e$  and  $n_e$  at different times during the evolution of the two discharges (respectively 0.5s, 0.7s and the average over the phase 0.8-0.9s). As in Fig. 3.9, with a central beam,  $T_e(0)$  immediately increases, but this is not necessarily due to a significant confinement improvement. Moreover,  $\tau_{\text{CRT}}$  is expected to increase, so that the current density will redistribute on a slower time-scale. For the indicated late ECH case, soft X-ray measurements along a central chord indicate a rapid increase (50%) in the emissivity at approximately  $t = 0.65\text{s}$ , Fig. 3.11. This state is followed by a steady phase of higher confinement level. One can estimate a barrier to be formed at about 0.67s. The situation is somewhat more complicated if the central beam is applied simultaneously to the external current drive (Fig. 3.11). The soft X-ray emissivity is higher than the late ECH case before the barrier formation, since the temperature is higher. One observes

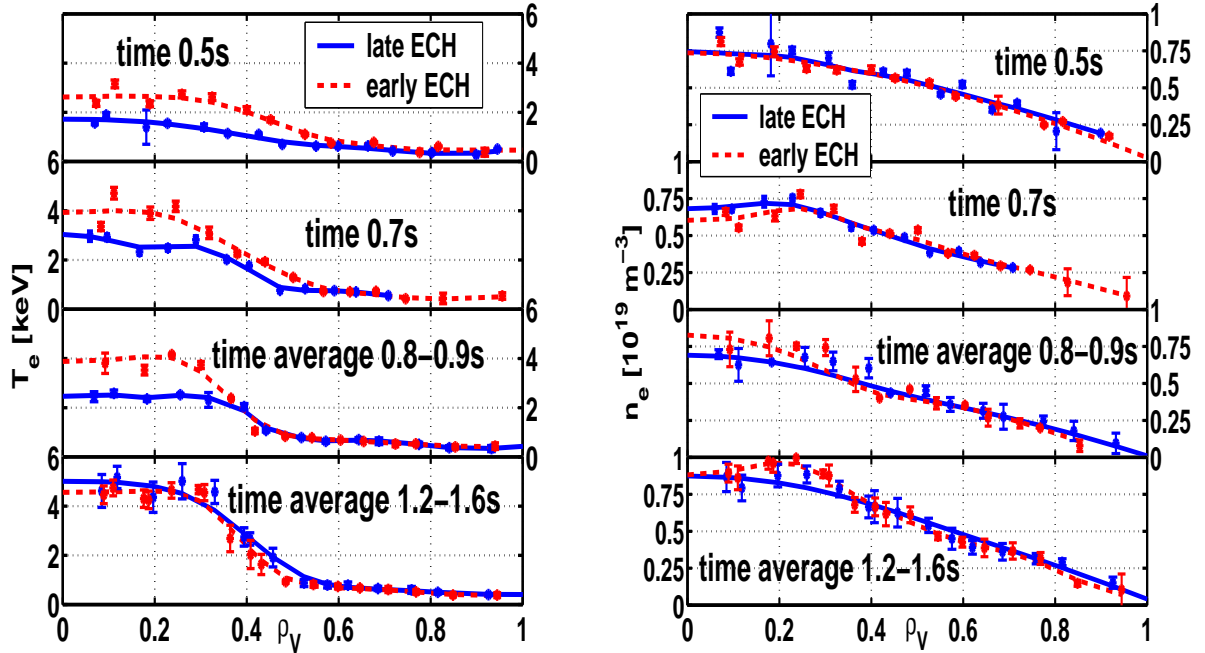


Figure 3.10: *Left plots: electron temperature experimental profiles at different times for the analyzed discharges. The profiles are comparable during the final steady state phase, when the heating is equal, whereas they differ during the initial heating phase. Right plots: electron density experimental profiles at different times for the analyzed discharges. The profiles are approximately comparable throughout the whole plasma discharge.*

again a 50% increase from  $t = 0.65$ s, followed by a steady phase lasting 100ms, after which a further confinement improvement occurs. This coincides with the eITB appearance and then the emissivity signal keeps on gradually increasing for about 250ms before the final steady state is attained. The barrier can thus be estimated to have completely appeared at 0.82-0.83s, which is almost 200ms later as compared to the late ECH discharge. The local position of the foot is approximately  $\rho_V = 0.5$  for both discharges. The exact time evolution is somewhat complicated because of MHD modes in the early ECH discharge starting around 0.75s. This mode is not expected to influence the barrier strength since it is slightly outside the foot of the barrier, however it can influence the detailed time evolution of the  $q$  profile, as discussed in Ref. [73]. In the early ECH case, the power is turned on at 0.4s and  $I_{OH}$  is set to a constant value. Nevertheless the full barrier is only reached near 1s, as indicated by the soft X-ray time trace. That is after about 600

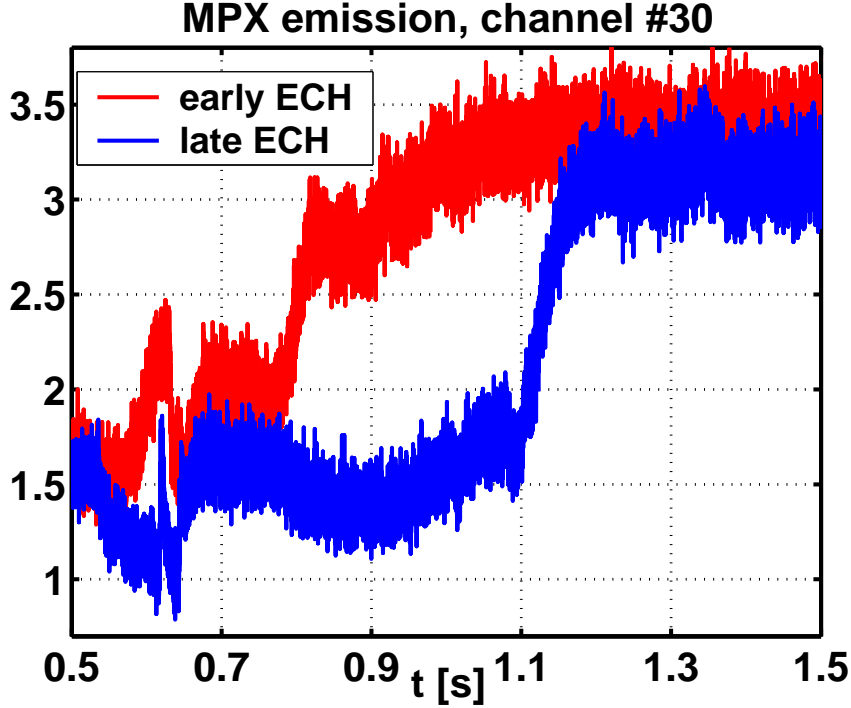


Figure 3.11: *Soft X-ray emission detected by a Multiwire Proportional X-ray counter for the two analyzed discharges, characterized by late (#21654) or early (#21649) EC injection.*

confinement times and 4 current redistribution times. On the other hand, in the late ECH case, the full power is set at 1.2s, the last gyrotron being ramped up between 1.1s and 1.2s. The soft X-ray trace essentially follows “instantly” the input power, that is on the local confinement time of about 1ms. Part of the difference could come from the MHD mode, however it is interesting to see the differences expected from the simulations.

To compare the time scale of the barrier formation, the transient phase during the eITB appearance has been modelled for these two plasma discharges. The modeling is interpretative, therefore the profiles of  $T_e$ ,  $n_e$ ,  $T_i$  and  $j_{\text{eccd}}$  have been imposed during these simulations. We are interested in comparing the different diffusion times of the current density profiles for the early/late ECH cases. Therefore, the imposed profiles of  $T_e(\rho, t)$  and  $n_e(\rho, t)$  have been varied every 50ms, which is the time resolution of the Thomson Scattering. The profiles of  $j_{\text{eccd}}$  have instead been calculated every 100ms, since they require long calculations with CQL3D. However, the usual procedure to determine the value of  $I_{\text{eccd}}$  from the difference between the other components of the total current is only valid



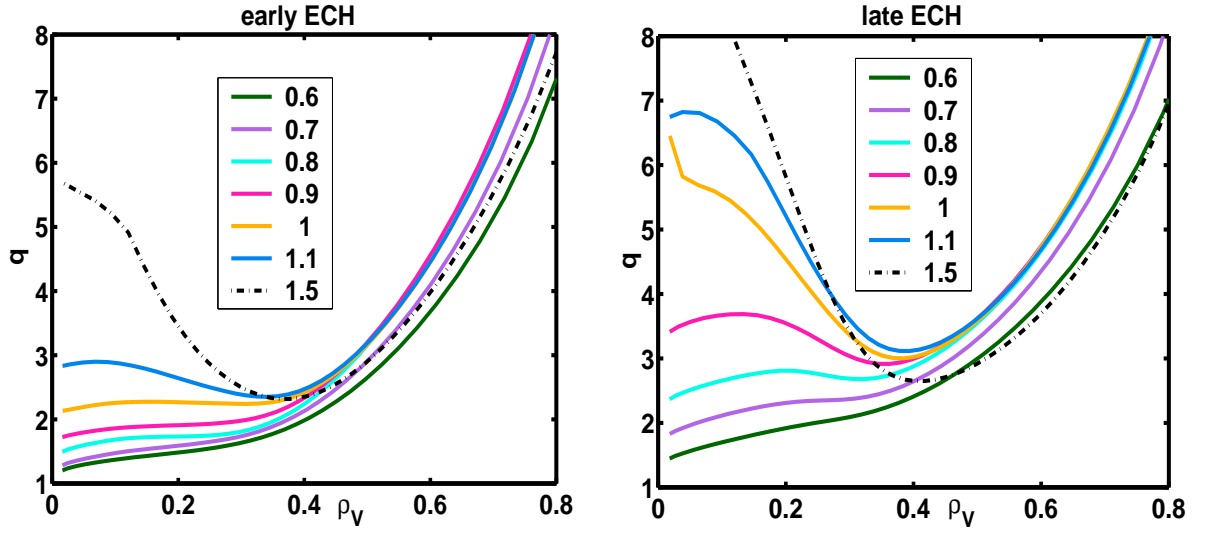


Figure 3.12: Safety factor profiles of the two analyzed discharges during their different evolutions due to the different heating schemes. The final state is comparable, but the evolution is slower with an early central beam.

at steady state. It is nevertheless possible to assume that the proportionality coefficient between the electron heat and particle diffusion coefficients,  $D_0$  (see Sec. 2.3.5), does not vary much during each discharge. Therefore, in this case the value of  $D_0$  determined at steady state ( $t \geq 1.2$ s) has also been used, for each discharge, in the Fokker-Planck calculations of  $j_{\text{eccd}}$  at the previous times. The values of  $D_0$  used throughout the simulations are  $D_0 = 0.18$  and  $D_0 = 0.15$  respectively for the early and late case. Results of the simulated magnetic shear and safety factor profiles, calculated by constraining  $I_p = I_p^{\text{exp}}$ , are reported in Figs. 3.12 and 3.13. First of all, the difference between the time-scales of these two shots is clear: whereas at 0.6s the two plasmas have roughly comparable profiles, at 0.7s they have already evolved very differently. For the late ECH case the magnetic shear near  $\rho_V = 0.3$  rapidly decreases, reaching values clearly negative (Fig 3.13, right). On the contrary, the early ECH plasma displays a slow evolution and only arrives at  $s = 0$  between 0.9s and 1.0s. However, there is an extended region, between  $\rho_V = 0.1-0.25$  and appearing from 0.8s, where the magnetic shear is very low, smaller than 0.1. The simulated zero-shear appears at  $t = 0.73$ s in the late ECH case, at a radial location of about  $\rho_V = 0.28$ . For the early ECH simulation, instead, this occurs at  $t = 0.95$ s, over the large region mentioned,  $\rho_V = 0.1-0.25$ . Therefore, again, the results of the early ECH modeling are in rough agreement with the hypothesis that the barrier shows up once

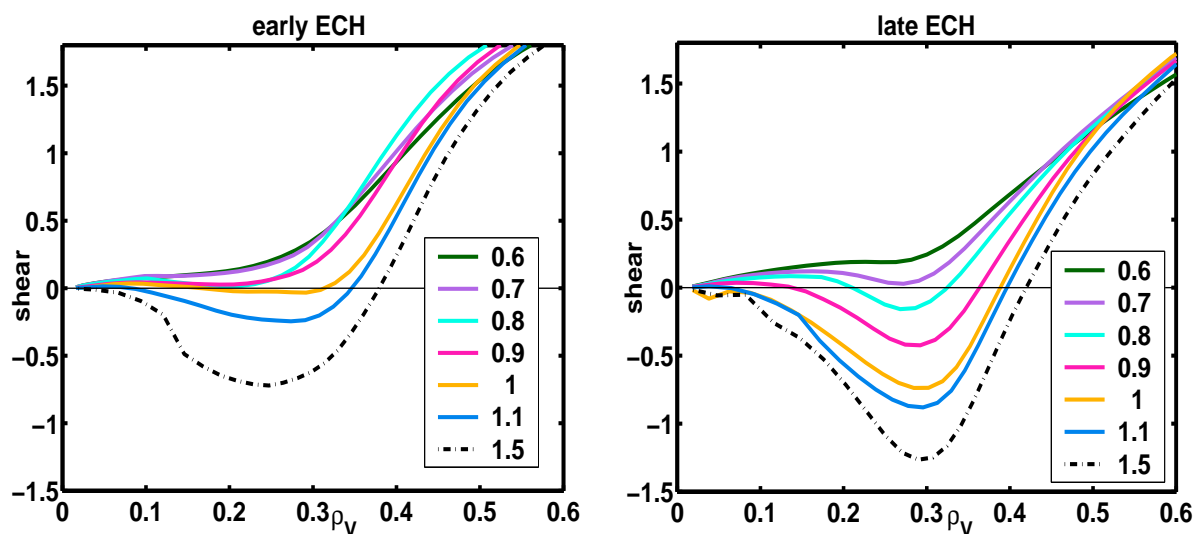


Figure 3.13: *Shear profiles of the two analyzed discharges during their different evolutions due to the different heating schemes.*

a zero-shear surface has occurred in the plasma. Another possible explanation, still in agreement with the reconstructed results, is that a small, yet positive threshold of the value of  $s$  is necessary for the barrier triggering instead of a zero-shear surface. Indeed, the shear profile is already fairly flat at  $t = 0.8\text{s}$  for the hotter plasma, with a value below  $s = 0.1$ . As already mentioned, the final states of the two discharges are comparable. This is well reproduced by the steady state ASTRA simulation of the final states at  $t = 1.5\text{s}$ , as evident from the dash-dotted  $q$  profiles in Fig. 3.12. The large difference in the time taken to full performance shown in Fig. 3.11 is consistent with the simulations shown in Figs. 3.12 and 3.13, and the fact that one needs sufficient negative shear to reach full performance.

### 3.4.4 Improving the eITBs simulations accuracy by experimental constraints

Concerning the temporal evolution of the reconstructed profiles, another discharge has been analyzed during the change in confinement. The peculiarity of this plasma resides in the presence of a clear tearing mode, which occurs at the same time as the barrier formation. The location and width of the mode have been determined using the signals from the DMPX as  $\rho_V = 0.42$  and  $3\text{cm}$  [65] respectively. This activity has been identified

to be a  $m=3/n=1$  magnetic island from magnetic and soft X-ray measurements, and it can be taken into account in order to remove a degree of freedom from the modeling, because it means we have an idea of the position of the  $q = 3$  surface [65]. For all these non-inductive discharges, the deposited power in the plasma center is negligible, since there is little ohmic power provided and the ECH deposition is outside  $\rho_V = 0.1$ . The Fokker-Planck modeling of the electron distribution function requires the radial particle diffusion coefficient,  $D_r$ , to be provided.  $D_r$  is assumed to be proportional to the heat diffusion coefficient,  $\chi_e$  (see Sec. 2.3.5). The latter is estimated from power balance, but since no power is deposited in the center,  $\chi_e$  is ill-determined in this region ( $\rho_V \leq 0.2$ ). The proportionality coefficient between the heat and particle diffusion coefficients is here assumed to be  $D_0 = 0.12$ , as this value causes the simulated  $I_{\text{eccd}}$  to match the estimated experimental total driven current. To provide an estimate of the central particle diffusion coefficient,  $D_r(0)$ , its value has been spanned from 0.06 to  $1.2\text{m}^2/\text{s}$  in the computation of the ECCD profile (as shown in Fig. 3.14), so as to obtain a scan of  $j_{\text{eccd}}$ . This is also

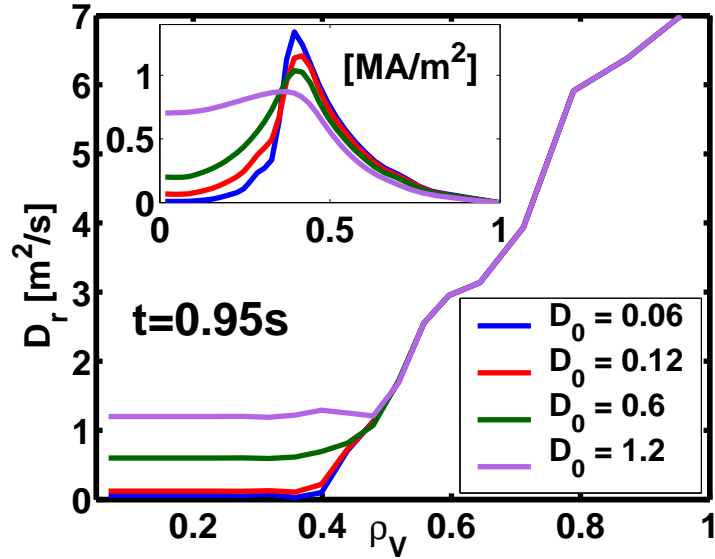


Figure 3.14: Profiles of the particle diffusion coefficient used to determine the ECCD current density profile, with different central values used in the calculations. The zoom reports the corresponding  $j_{\text{eccd}}$  profiles obtained.

used to simulate the increased transport in the very core which can be inferred from the flat profiles inside  $\rho \leq 0.4$  and that could be due to small current density near the axis. The corresponding simulated driven currents are shown in the small diagram in Fig. 3.14.

Increasing the central radial particle transport has the effect of broadening the ECCD profile in the center.

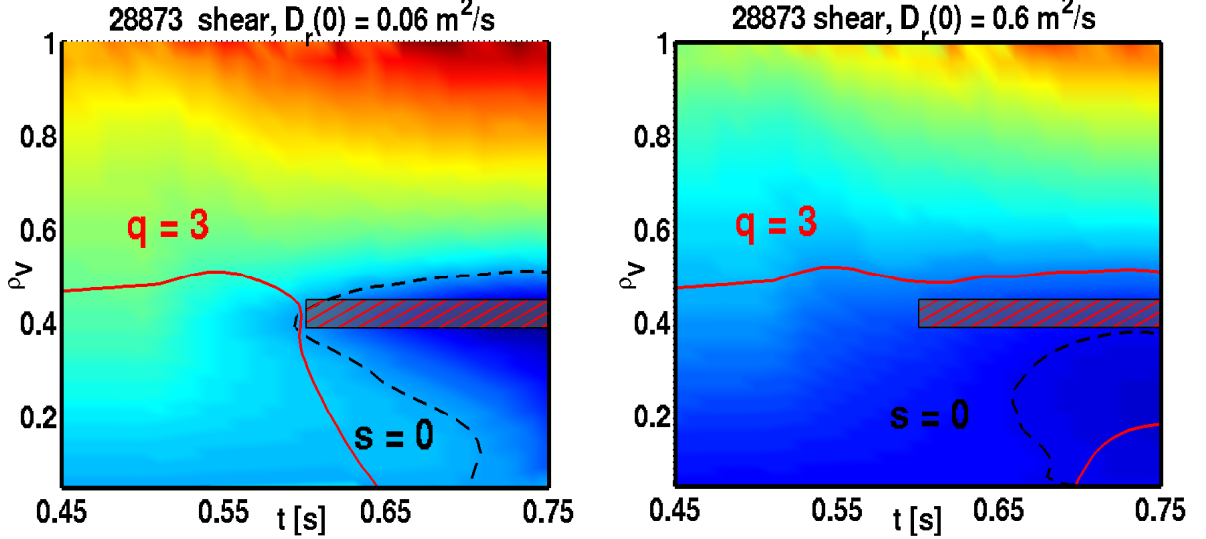


Figure 3.15: *Contour plots of the shear time evolution of a discharge exhibiting a 3/1 mode, for two different values of the central particle diffusion coefficient  $D_r(0)$ . The  $q = 3$  and  $s = 0$  surfaces are indicated by the solid red line and dashed black line, respectively. The striped band reports the experimental location and time occurrence of the mode. When the particle diffusion is small (left plot), the  $q = 3$  surface appears simultaneously to the mode, but disappears about 50ms after. With a higher particle diffusion, instead, the mode stays in the plasma throughout the whole discharge, with  $s \sim 0.5$  at  $t = 0.6$ s and near  $\rho_V \sim 0.4$ .*

Each of these  $j_{\text{eccd}}$  profiles has then been used in the ASTRA simulation and the contour plots of the resulting magnetic shear evolution for two of these cases are shown in Fig. 3.15, with the thick dashed line being the zero-shear surface and the red solid one indicating the  $q = 3$  surface. For  $D_r(0) = 0.06\text{m}^2/\text{s}$  (Fig. 3.15, left), the  $q = 3$  surface coincides with the  $s = 0$  surface at approximately the same experimental time as the barrier triggering identification. Experimental analysis shows that the mode occurs at about  $t = 0.6$ s, simultaneously to the barrier formation, and that it remains inside the plasma for at least some  $\tau_{\text{CRT}}$ : however, the left-hand numerical example shows the  $q = 3$  surface disappearing after a short time ( $q_{\text{min}} > 3$ ). If  $D_r(0) = 0.6\text{m}^2/\text{s}$ , the  $q = 3$  surface instead stays in the plasma for a much longer time, as shown in Fig. 3.15 (right). This is consistent with the experimental observation that the 3/1 mode remains in the plasma for a long

time. Furthermore, a high diffusion coefficient in the center is also consistent with the observed flat central density and temperature profiles. In the latter case,  $s = 0$  appears somewhat later, at  $t = 0.65$ s, than the barrier formation observed at  $t = 0.6$ s. This could be within the errorbar of the reconstruction or could mean that the barrier forms when  $s$  becomes small but still positive, as pointed out previously in this section. At  $t = 0.6$ s, the minimum magnetic shear is about 0.5, near  $\rho_V \sim 0.4$ . Finally, since the effective charge plays a role in the current diffusion, a study of the sensitivity of the reconstructed  $s$  profile on the value of  $Z_{\text{eff}}$  is illustrated for the case of  $D_r(0) = 0.6\text{m}^2/\text{s}$  (Fig. 3.16). If

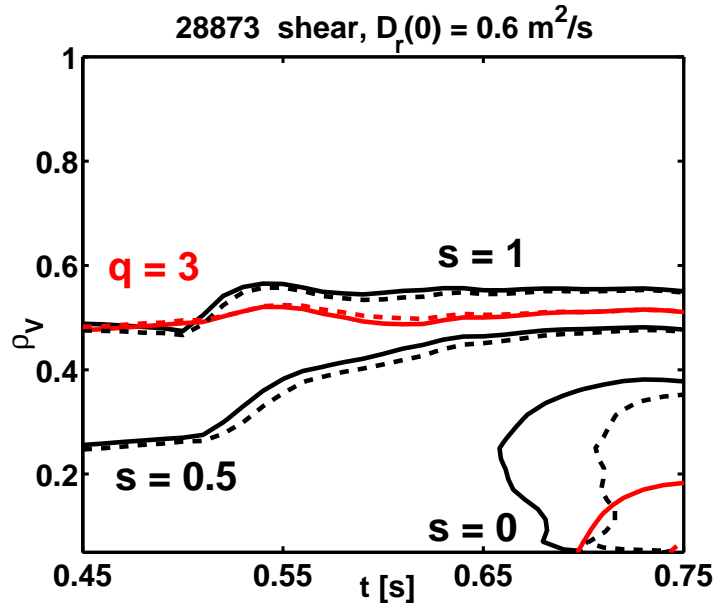


Figure 3.16: *Study of the sensitivity so the value of  $Z_{\text{eff}}$  for the reconstructed shear assuming a central particle diffusion coefficient of  $D_r(0) = 0.6\text{m}^2/\text{s}$ . The solid lines refer to  $Z_{\text{eff}} = 4$  and the dashed lines to  $Z_{\text{eff}} = 2$ .*

$Z_{\text{eff}}$  is changed from 4 to 2, the analysis indicates that the formation of the  $s = 0$  surface is delayed by about 50ms. Therefore, the argument of the proximity to magnetic shear reversal is still in rough agreement for a scan in  $Z_{\text{eff}}$  from 4 to 2 (respectively solid and dashed lines). However, the  $s = 0.5$  and  $s = 1$  surfaces are essentially unaffected by the value of the effective charge.

### 3.4.5 Negative central current density

It is worth pointing out that, on TCV, when a very peaked negative inductive current is generated, the total plasma current density could, in principle, become negative near the plasma center (negative with respect to the total plasma current direction). The possibility of obtaining this flip in the plasma current density sign, or as it is often referred to a “current hole”, has been the object of various investigations, both experimental and theoretical. For instance, recent experiments on JET [74], [75] and JT60-U [76], [77] have pushed the core current density to very low values using off-axis, non-inductive current drive. Large central current holes (regions of nearly zero current density) are produced because off-axis, non-inductive current drive in the same direction as the ohmic current induces a back electromotive force inside the non-inductive current drive radius that decreases the core current density. In Ref. [78], it has been shown that, if an appropriate plasma rotation velocity is provided, then normal equilibrium is not forbidden for reversed current. By “normal” equilibrium it is meant an axisymmetric equilibrium with nested magnetic surfaces around the magnetic axis and with the pressure decreasing from the plasma center to the periphery. On the other hand, more general axisymmetric equilibria with reversed current density and poloidal field have been computed, with different topology of the magnetic surfaces [79]. These equilibria are characterized by the presence of axisymmetric magnetic islands. The question of the relevance of the proposed equilibrium solutions to experiments is open. Even though the existence of an axisymmetric equilibrium with negative central current has been shown to be possible [78], [79], ASTRA and CHEASE cannot solve such a case. Therefore, in order to simulate such scenarios, a fictitious on-axis current step had to be added, namely a Heaviside current density, with negligible additional total current. Fig. 3.17 reports the original ECCD component profile in black solid, whereas the step-like profiles are the additional CD component, at different radial locations, used to avoid the central current density hole.

The corresponding  $q$  profiles are shown in Fig. 3.18, with a zoom of the  $q$  profile in the right plot. The safety factor is influenced in a way that, by gradually shifting more and more on-axis the boundary of the Heaviside current density, the radial location of  $q_{\min}$  moves outwards and the values of  $q_{\min}$  increase. Various scans of the applied voltage and of the current step location have been performed, resulting in Fig. 3.19, which shows the values of  $q_{\min}$  as a function of the radial location of the extra current density, for various

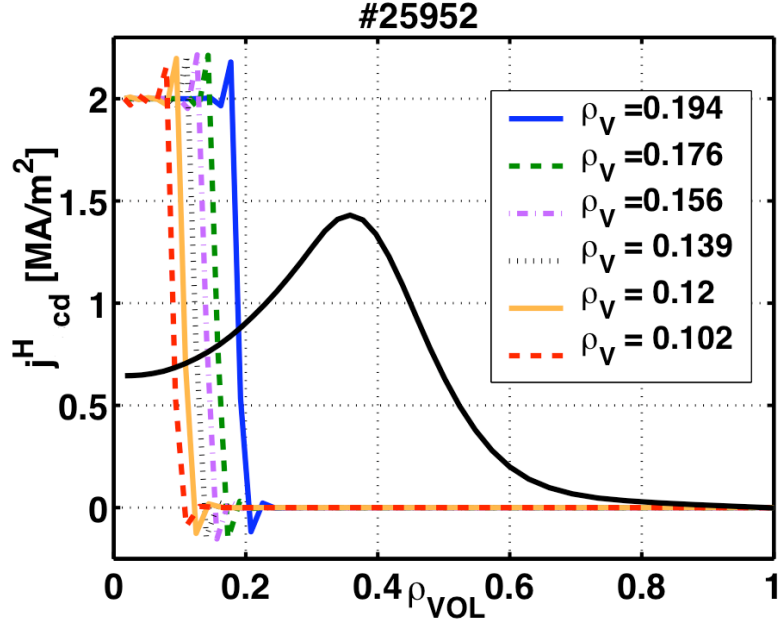


Figure 3.17: Various Heaviside current density components used in the simulations. The legend reports their radial location. The ECCD component is also shown in solid black.

values of the applied  $V_{\text{loop}}$  in the simulations. With an extra current density, the values of  $q_{\text{min}}$  are generally slightly underestimated. In the figure, the radial coordinate used is the minor radius in [m], which corresponds in this case roughly to  $\rho_V < 0.2$ . Modifying the current density profile within  $r = 0.05\text{m}$  mainly perturbs the  $q$  reconstruction inside  $\rho_V = 0.2$  ( $\rho_\psi = 0.3$ ).

### 3.4.6 Comparison of steady state ASTRA $q$ profiles with CHEASE reconstructions

A correct description of the equilibrium magnetic fields and current densities in transport simulations is of great importance in tokamak physics, because transport and geometrical effects are linked together and should therefore be described self-consistently. The transport equations in ASTRA are coupled to a 3-moment approach equilibrium solver, which allows for a fast solution of the Grad-Shafranov equation and a self-consistent determination of the transport and equilibrium within the ASTRA loop. For certain cases, however, namely in the simulations of discharges with high bootstrap current fraction, leading to an eITB and a very reverse magnetic shear, the equilibrium can show rather extreme radial

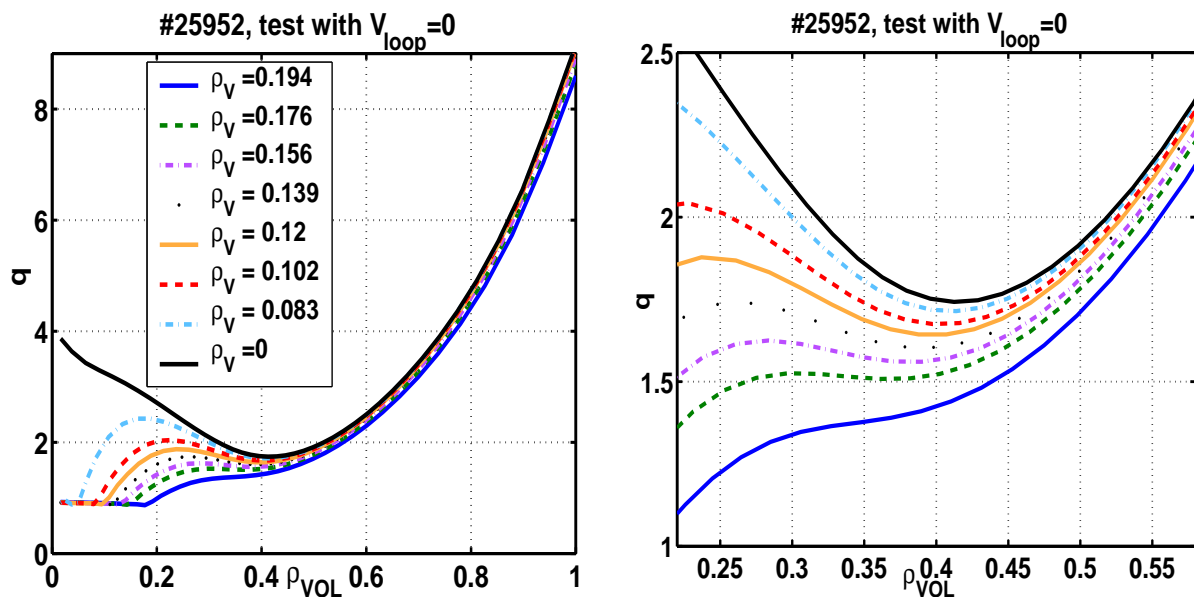


Figure 3.18: *Safety factor profiles simulated for different radial locations of the extra Heaviside current density. The value of  $q_{\min}$  increases by shifting more on-axis the location. The radial location of  $q_{\min}$  moves outwards, and the values of  $q_{\min}$  are, generally, slightly underestimated.*

profiles, which become more difficult to correctly simulate. For instance, some fundamental quantities such as the plasma collisionality,  $\nu_e^*$ , and the trapped fraction,  $f_t$ , profiles have sometimes shown inconsistencies with the CHEASE calculated profiles in the center. This obviously influences the accuracy of the neoclassical transport coefficients, such as the neoclassical conductivity and the bootstrap coefficients in the centre. Therefore, it is important to check that the ASTRA modeling still provides sufficient accuracy for the equilibrium calculation, by comparing the steady state  $q$  profiles with the CHEASE profiles obtained from the ASTRA output. Fig. 3.20 shows, for two different TCV discharges (one with monotonic  $q$ , #25957, on the top diagrams, and one with reverse magnetic shear, #25952, on the bottom diagrams) the  $q$  and  $j$  profiles from ASTRA and CHEASE simulations. The difference for  $\rho_\psi < 0.25$  is due to different ways of clamping the central current density profile in the case of very reverse magnetic shear. Besides this difference in the centre, however, the profiles are in excellent agreement, confirming the accuracy of the ASTRA equilibrium. This is also evident from the  $j_{\text{bs}}$  and  $\sigma_{\text{neo}}$  profiles shown in Fig. 3.21. The robustness of the final considerations on the  $q_{\min}$  and the negative magnetic shear is thus confirmed. Even though to a certain extent less accurate, the



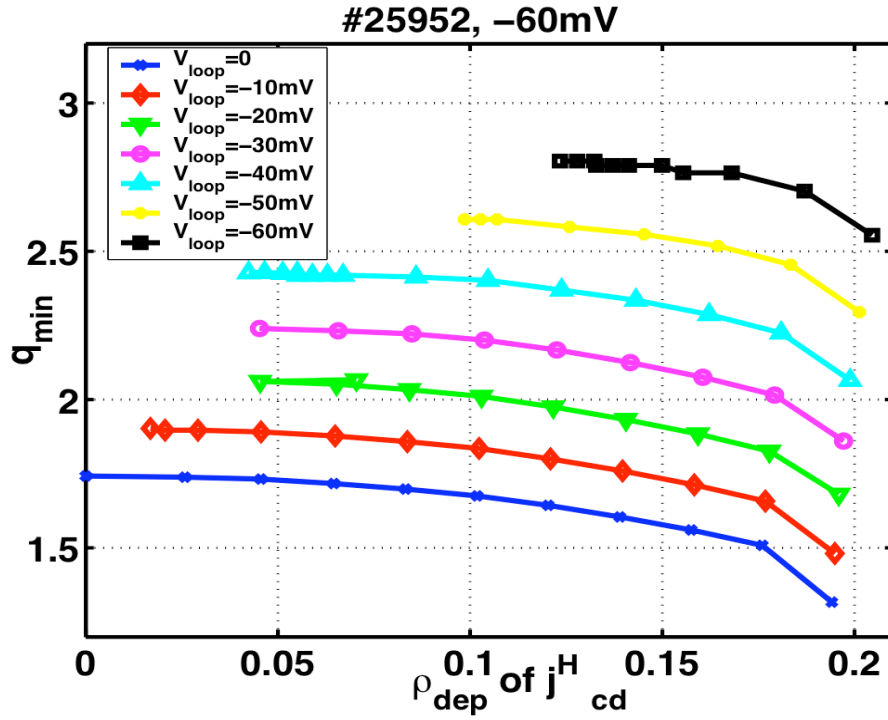


Figure 3.19: Minimum values of the safety factor profile as a function of the square root of the normalized volume at which the Heaviside  $j_{cd}^H$  has been deposited.

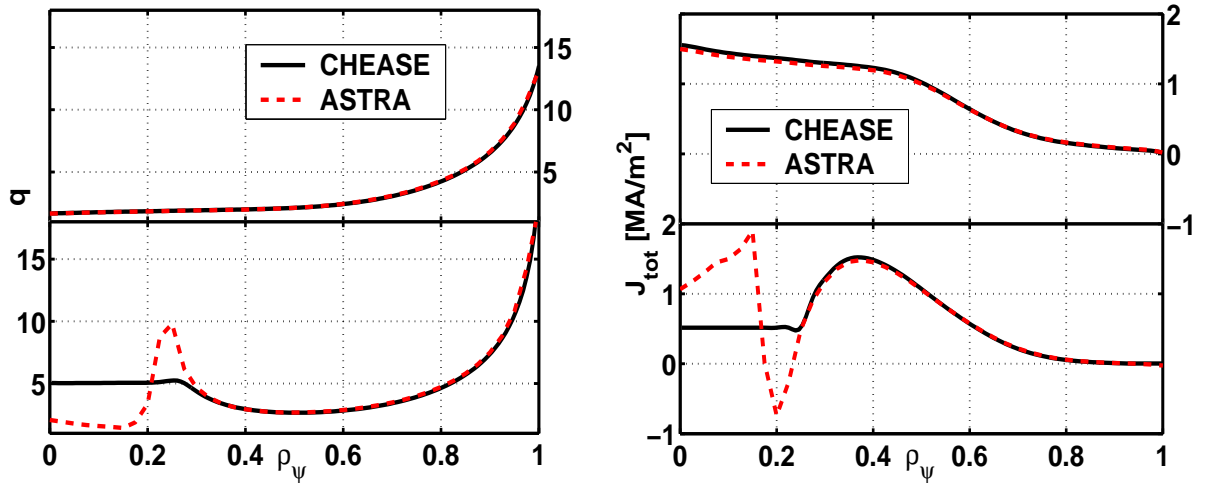


Figure 3.20:  $q$  and  $j_p$  profiles from ASTRA and CHEASE simulations, for two different TCV discharges (#25957 on top and #25952 on bottom).

usage of the ASTRA code for interpretative, steady state equilibrium reconstructions is still greatly advantageous, since it is user friendly, fast, modular and allows interactive

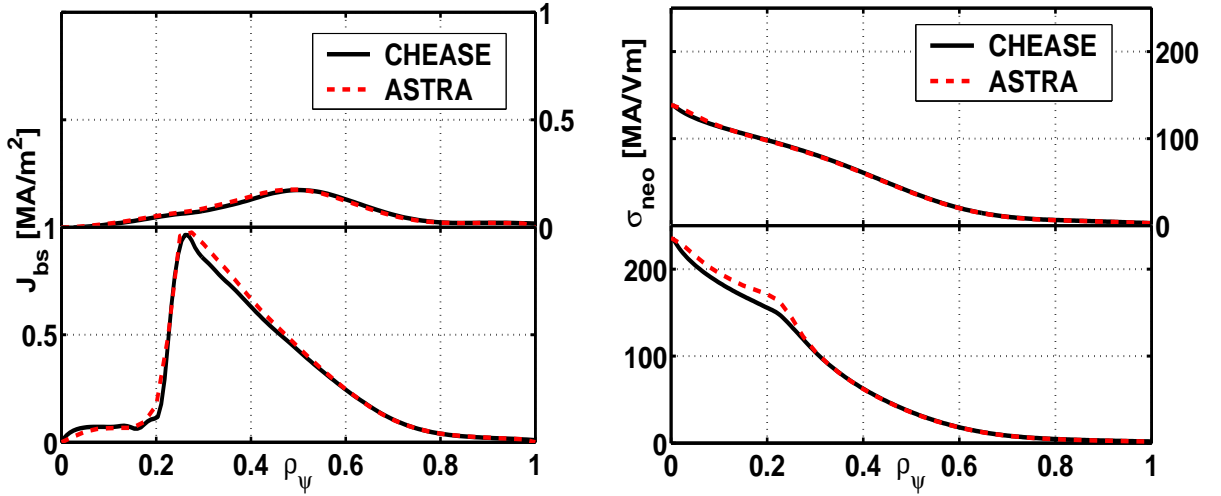


Figure 3.21:  $j_{bs}$  and  $\sigma_{neo}$  profiles from ASTRA and CHEASE simulations, for two different TCV discharges (#25957 on top and #25952 on bottom).

modifications during a run. Note that the good agreement is also due to the relative simple plasma boundary shapes which have been used in these TCV experiments.

### 3.5 Summary and conclusions

Simulations of the plasma current density evolution in electron Internal Transport Barrier discharges on the Tokamak à Configuration Variable have been performed, in order to determine the relationship between the safety factor profile and the electron transport improvement. The results show that the formation of the transport barrier is correlated with the shear reversal in all cases studied, regardless of the different heating and current drive schemes. No indications were found of an effect peculiar to low order rational  $q$  surfaces. On the contrary, the increase of confinement along with the negative shear is gradual, but constant, indicating that the transition is smooth, although it can be very fast. They correspond therefore to a second order transition for ITB formation discussed in Ref. [80].

Results arising from the ASTRA modeling of the plasma current density profile in TCV advanced scenarios have been presented. The range of relevant normalized plasma parameters at mid-radius spanned during this analysis is the following:  $\beta_N \sim 0.6 - 1.2$ ,  $T_e/T_i \sim 3 - 5$ ,  $\nu_e^* \sim 0.018 - 0.1$ ,  $R/L_{Te} \sim 5 - 20$  ( $\beta_N$  being the normalized toroidal

plasma pressure,  $T_e/T_i$  the temperature ratio,  $\nu_e^*$  the effective collisionality,  $R/L_{T_e}$  the normalized electron temperature gradient). First, simulations of ohmic perturbations on already formed eITBs have been discussed. In these scenarios, the final steady state is characterized by the presence or absence of a well defined negative shear region, starting from an initially slightly non-monotonic  $q$  profile. The simulated profiles are consistent with the hypothesis that the presence of an eITB is related to the existence of an  $s \leq 0$  region in the plasma. They have shown agreement with the experimental observation that the more reversed the shear, the better the confinement.

The work has also addressed the study of discharges with comparable initial and final steady states, but different intermediate phases due to different heating conditions. The difference in the current penetration during the time evolution has been correctly reproduced by ASTRA. In addition, it was shown that the identification of MHD activity can be used to remove one degree of freedom to the modeling and thus allow to restrict the uncertainty of the central value of the radial particle diffusion when this is ill-determined due to the absence of power deposited in the plasma center.

The dynamics regulating transport barriers and confinement improvement are rather complex mechanisms, but the previous discussions confirm the important role played by the local value of the magnetic shear for the confinement improvement. No evidence was found that any specific value of  $q_{\min}$  favors the eITB triggering; rather, the confinement improvement occurs during a smooth and rapid transition while the magnetic shear becomes more and more reversed. Although the  $q$  profile is not measured on TCV, the present detailed simulations suggest that the local confinement improvement is consistent with a linear and continuous increase with decreasing local magnetic shear.

# Chapter 4

## Swing ECCD discharges on TCV

### 4.1 Introduction

In the course of this thesis, it has already been mentioned that understanding the physical connection behind the electron confinement and the plasma current density profile has become of primary importance for the most successful exploitation of a future fusion reactor. A precise understanding of transport, based on the experimental study of plasmas and on their modeling, allows one to identify the key parameters controlling the transport level and to predict the energy confinement time of future tokamaks, like ITER. The electron confinement and the plasma current density profile were found to be strongly related by a variety of dedicated experiments in many tokamaks. For instance, in the previous Chapter, it has been shown that TCV electron confinement was found to improve by modifying the steady state current density from peaked to hollow [81]. Such behavior is believed to be due to the suppression of plasma turbulence in the presence of a negative magnetic shear and a finite Shafranov shift [69].

The electron temperature behavior and the transport modeling of plasma discharges have been widely investigated in TCV. The current density profile being a key element which can strongly affect plasma turbulence, it is useful to design dedicated experiments specifically suitable for transport studies, solely based on the current profile modification. In the following Sections, we present the analysis of Swing ECCD discharges which have been designed with the purpose of providing a better insight on the magnetic shear profile modification, as realized in said experiments.

## 4.2 Swing ECCD experiments on TCV

### 4.2.1 Experimental set-up

L-mode experiments with modulation of ECCD at constant total input power have been performed at TCV [19], with the purpose of decoupling the contributions of heating oscillations from those of the current tailoring. The ECRH-ECCD system at TCV is equipped with two independently supplied clusters each composed of 3 X2 gyrotrons, providing up to 3 MW of total EC power. This allows generation of a Swing ECCD in L-mode plasmas, i.e. driving alternatively positive or negative local ECCD at constant total input EC power during a single discharge. Indeed, in these Swing ECCD discharges,

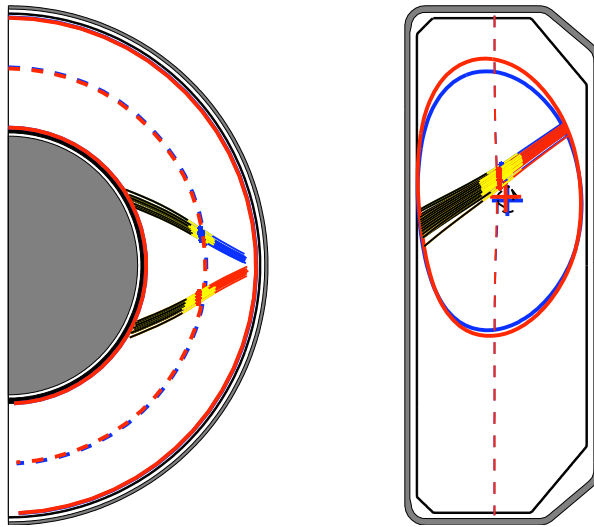


Figure 4.1: *Top and side views of the EC beams injected in a typical Swing ECCD discharge. The blue and red color coded beams correspond, respectively, to the co- and cnt-ECCD. The light gray section corresponds to 99% absorption. The ray paths are calculated with the TORAY-GA ray-tracing code [47].*

co- and counter-ECCD, peaked slightly off-axis, are alternatively injected at a constant frequency inside the plasma, while maintaining a symmetric aiming of the EC beams, the same absolute value of total driven current and the same EC power deposition profile,  $P_{\text{EC}}(\rho)$ ; the configuration is shown in Fig. 4.1. The underlying motivation behind these experiments is to decouple the contributions of heating oscillations from those of the current density tailoring, so that any modification in the transport properties of the

plasma can be ascribed to the magnetic shear profile modulation.

The target L-mode plasmas are characterized by the following range of parameters:  $I_p = 120\text{-}150\text{kA}$ ,  $\kappa \sim 1.2\text{-}1.4$ ,  $P_{\text{EC}} = 0.5\text{-}1\text{MW}$ ,  $n_{\text{el}} = 1\text{-}1.5 \cdot 10^{19}\text{m}^{-3}$ ,  $B_0 = 1.42\text{T}$ ,  $f_{\text{ec}} = 50\text{Hz}$ . In order to account for possible EC power misbalance, all Swing ECCD discharges presented were realized in pairs, with the toroidal injection angle,  $\phi$ , of the two EC clusters inverted. The purpose of this procedure is to create pairs of Swing ECCD measurements in which the EC clusters driving co-/counter-ECCD are simply flipped, while keeping all other actuators constant. If the modulation effect is observed in both discharges constituting the pair, even registering differences in signal intensities due to EC power misbalance, then the  $T_e$  modulation can really be ascribed to a true transport phenomenon and not, for instance, to small misbalances in heating. Preliminary pure ECH discharges have also been performed, with alternated on/off phases of the two EC beam clusters, to check that the total plasma energy stays constant and, if not, to adjust  $P_{\text{EC}}$  as necessary. It should be pointed out that the balance of the EC power from the two clusters turned out to be a very important and delicate problem in Swing ECCD discharges; it has not been completely overcome. For this reason, the experimental analysis is of rather difficult interpretation and further Swing ECCD discharges should be realized in order to clearly validate the observed phenomena. The results of the simulations presented in the following Sections also help in designing the future experiments.

## 4.2.2 Electron transport properties

The main goal of Swing ECCD experiments is to realize a modulation of the magnetic shear in order to study the consequent effects on the central electron temperature (and thus of confinement properties). Fig. 4.2 shows the time traces of some measured and reconstructed quantities during two Swing ECCD discharges realized at two different deposition locations of the EC modulation, respectively  $\rho_V \sim 0.3$  and  $\rho_V \sim 0.55$ . The first time trace reports the constant plasma current and, in arbitrary units, the modulated total EC power for the cluster of gyrotrons driving co-ECCD, the other trace having a  $180^\circ$  phase-shift. The total injected EC input power is constant, as shown by the constant diamagnetic loop (DML) time trace. The other time traces reported are the central electron temperature,  $T_{e0}$ , the line integrated electron density,  $n_{\text{el}}$ , the internal inductance,  $l_i$ , and the plasma elongation,  $\kappa$ . Following the ECCD swing,  $T_{e0}$ ,  $n_{\text{el}}$ ,  $l_i$

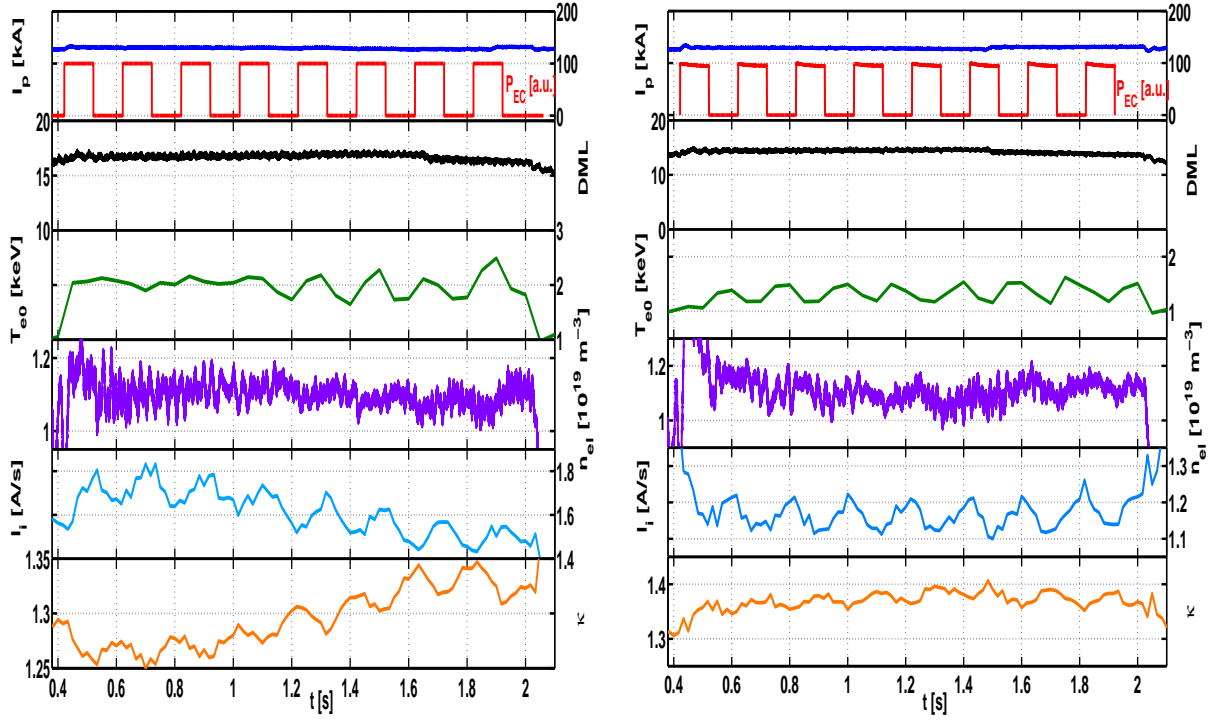


Figure 4.2: Time traces of two TCV Swing ECCD discharges (#34064 and #34044), in which the ECCD modulation is respectively realized at  $\rho_V \sim 0.3$  and  $\rho_V \sim 0.55$ . a) Constant plasma current and modulated total input EC power for the cluster of gyrotrons driving co-ECCD. The EC power traces are in arbitrary units, and the values of the total injected  $P_{EC}$  are 450kW for the on-axis discharge and 900kW for the off-axis discharge. b) DML energy content, constant over the entire discharge. c) Modulated central electron temperature. d) Line integrated electron density. e) Internal inductance from the LIUQE reconstruction. f) Reconstructed plasma elongation. The  $P_{EC}$  trace (in arbitrary units) corresponds to the co-ECCD phase.

and  $\kappa$  are also modulated at the same modulation frequency. Fig. 4.3 shows the Thomson Scattering  $T_e$  and  $n_e$  profiles of, respectively, the on-axis and the off-axis case. The profiles are obtained from the coherent time average over the final states of the two phases, the co- and counter- phases, for each discharge. For both discharges, the average over the co-ECCD phase includes  $t_{co} = [0.5 \ 0.7 \ 0.9 \ 1.1 \ 1.3 \ 1.5 \ 1.7 \ 1.9]$ s, whereas the counter-ECCD phase  $t_{counter} = [0.6 \ 0.8 \ 1.0 \ 1.2 \ 1.4 \ 1.6 \ 1.8 \ 2.0]$ s. While the electron density profile stays approximately constant throughout the whole discharge, the electron temperature profile inside  $\rho_{dep}$  appears modulated at the same frequency of the EC alternate injection. For

the on-axis case, the injection of co-ECCD results in a central  $T_e$  of about 2.05keV, while injecting counter-ECCD decreases the value of central  $T_e$  to 1.75keV. For the off-axis case, the injection of co-ECCD results in a central  $T_e$  of about 1.2keV, while injecting counter-ECCD increases the value of central  $T_e$  to 1.55keV. Therefore, in the on-axis Swing ECCD discharge ( $\rho_{\text{dep}} = 0.3$ ), the experimental data show that  $T_e^{\text{co}} > T_e^{\text{counter}}$ . For the off-axis Swing ECCD discharge ( $\rho_{\text{dep}} = 0.5$ ) one finds, instead,  $T_e^{\text{counter}} > T_e^{\text{co}}$ .

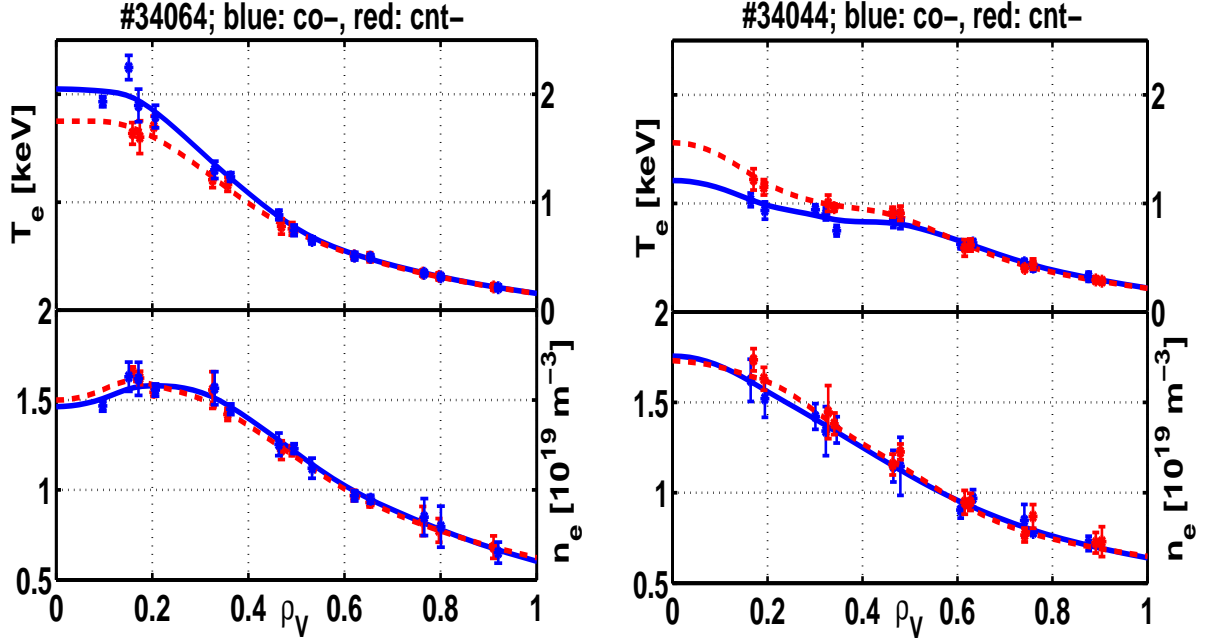


Figure 4.3: *Radial profiles of the experimental Thomson Scattering  $T_e$  data, which are averaged over each phase, showing the modification of transport properties during the two Swing ECCD phases. For both discharges, the average over the co-ECCD phase includes  $t_{\text{co}} = [0.5 \ 0.7 \ 0.9 \ 1.1 \ 1.3 \ 1.5 \ 1.7 \ 1.9]s$ , whereas the counter-ECCD phase  $t_{\text{counter}} = [0.6 \ 0.8 \ 1.0 \ 1.2 \ 1.4 \ 1.6 \ 1.8 \ 2.0]s$ .*

The  $T_e$  modulation maintains the same behavior in the corresponding paired discharges as well (obtained inverting the toroidal injection angle). In Fig. 4.4, the time traces of three central X-ray measurements are shown for the two Swing ECCD discharges described above and the corresponding paired discharges. The pair of discharges reported in the first plot was obtained with EC poloidal and toroidal injection angles  $(\theta, \phi) = (120^\circ, \pm 163^\circ)$ , corresponding to on-axis deposition (around  $\rho_{\text{dep}} = 0.3$ ), while the pair of discharges reported in the second plot was obtained for  $(\theta, \phi) = (106^\circ, \pm 156^\circ)$ , corresponding to off-



axis deposition ( $\rho_{\text{dep}} = 0.55$ ). As evident from the two plots, while for the first of them the co-ECCD phase is consistently higher than the counter-ECCD phase, for the second plot the situation is inverted so that the counter-ECCD phase is consistently higher than the co-ECCD phase. The difference in signal intensities for each pair of discharges can be ascribed to small differences in heating between the two EC cluster gyrotrons and small differences in density.

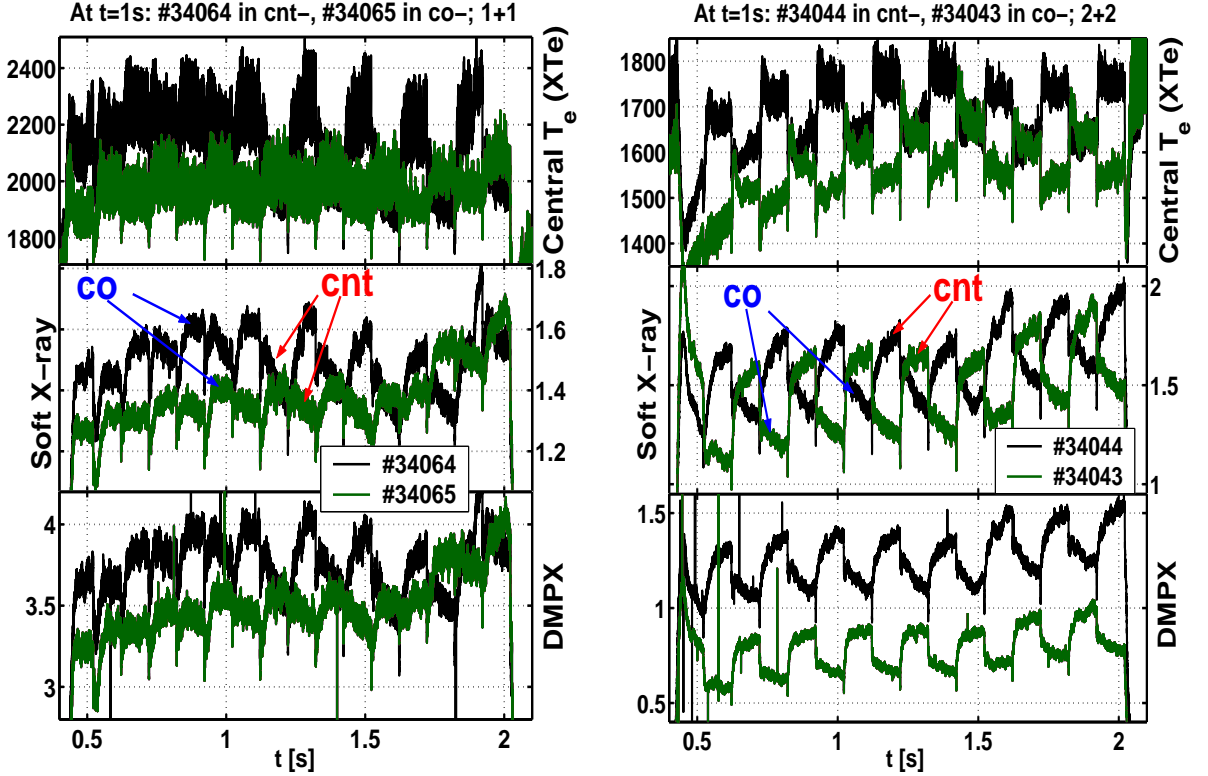


Figure 4.4: Time traces of three central X-ray measurements for two pairs of Swing ECCD shots. The deposition location of the ECCD Swing was done on-axis for case a), and off-axis for case b).

Gyrokinetic linear simulations by Kinsey *et al.* [82], performed using the GYRO gyrokinetic code [83], with kinetic electrons, have found analogous results: the confinement properties increase if the magnetic shear decreases, in the radial region where  $s < 1$ . At larger values of the magnetic shear (typically  $s > 1 - 1.5$ ), the opposite behavior is, instead, predicted (see Fig. 19 of Ref. [82], which shows the time-averaged ion and electron energy, and ion particle diffusivities as a function of  $s$ ).

The discharges presented are consistent with the inversion of the confinement properties,

depending on the value of the magnetic shear, which is predicted by gyrokinetic simulations. This is experimentally observed even when inverting the EC clusters toroidal angles, in order to systematically flip the heating effects. However, in order to clearly link these experimental observations, i.e. the modulation of the electron temperature profile and the difference in the electron energy transport properties at different radii, to the value of the modulated magnetic shear, modeling of the current density profile is required. The results of the modeling will be presented in Sec. 4.4-4.5.

### 4.2.3 Scan in the deposition location

A shot-to-shot scan in the deposition location has been performed in order to sweep across the radial region where the transport inversion occurs, and to attempt identifying the plateau region predicted by micro-instability theory. However, this behavior has not been systematically and clearly observed in all plasmas. Fig. 4.6 shows two plots containing the average, over the two separate phases, of central soft X-ray measurements for the various Swing ECCD pairs realized. The color code of Fig. 4.6a groups all the discharges with their corresponding pair, whereas Fig.4.6b uses the color code to identify three radial regions of EC deposition:  $\rho_V < 0.25$  (orange),  $0.25 \leq \rho_V \leq 0.35$  (violet) and  $\rho_V \geq 0.35$  (green).

It should be noted that these discharges were found to be not very easy to control, especially with respect to the setting of the EC heating balance and the control of the modulations in  $n_e$ ,  $l_i$ ,  $\kappa$ . This may, in part, be due to the (likely) presence of small asymmetries in the EC heating system, and makes the Swing ECCD results of somewhat difficult interpretation. Indeed, despite the good balance observed during the pure ECH heating discharges, which are used to test the correct balance of the current drive, different absorptions have instead been observed, once the EC launchers are directed with a large toroidal angle, so as to drive enough ECCD current. The origin of this misbalance is not easy to identify and could be due to different reasons, such as small tilts from the programmed launchers angles, or to a different coupling between the pure heating phase and the current driving phase, or again to differences in the nominal gyrotron powers. Therefore, the analysis should nevertheless be complemented by a finer shot-to-shot scan over the EC deposition location, in order to identify the radial location at which the inversion in transport properties occur, once the heating misbalance origins have been

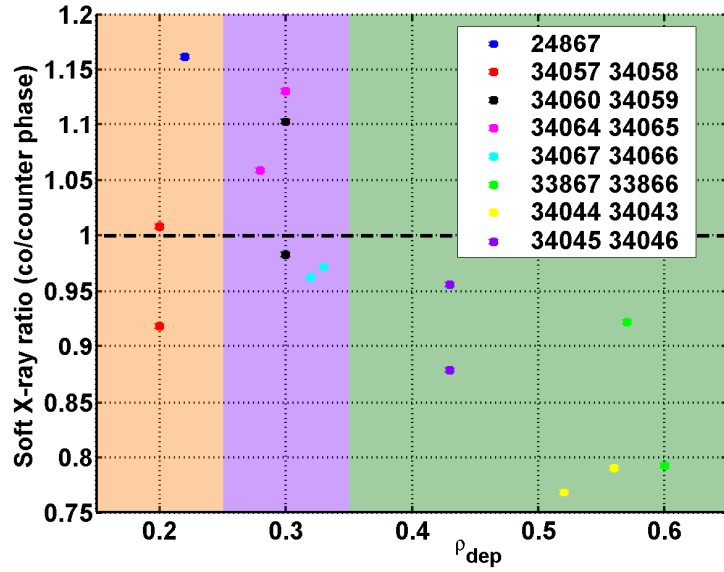


Figure 4.5: Ratio of the average Soft X-ray signal during the co-ECCD phase and the counter-ECCD phase for each Swing ECCD discharge as a function of the deposition location (in  $\rho_V$ ).

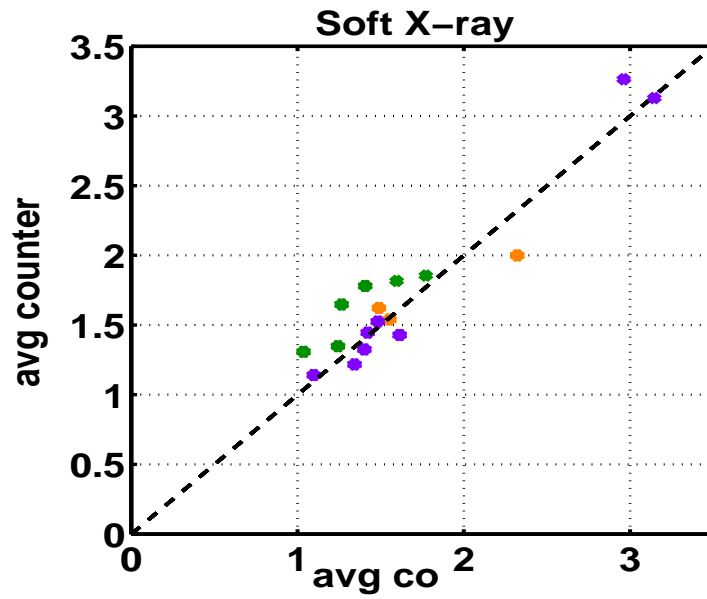


Figure 4.6: Average of central soft X-ray measurements over the two separate phases for the various Swing ECCD pairs realized, grouped by radial regions of EC deposition:  $\rho_V < 0.25$  (orange),  $0.25 \leq \rho_V < 0.35$  (violet) and  $\rho_V \geq 0.35$  (green).

assessed. However, before carrying out more Swing ECCD experiments, further deposition location tests using modulation are to be performed in order to know where exactly the beams are deposited.

### 4.3 Modeling of Swing ECCD

Theoretical investigations of the Swing ECCD regime are motivated by the need of a detailed reconstruction of the magnetic shear profile during the modulation phase. The plasma response in the presence of Swing ECCD has thus been studied in order to understand the differences in time scales and transient behaviours between the various models employed and with different experimental conditions, such as changes in deposition location and modulation period. This numerical analysis does not aim to correctly calculate the plasma current diffusion while reproducing the exact experimental set-up, because of the complexity of the dynamics associated with the Swing ECCD discharges. In the presented modeling, only a few actuators, such as  $T_e(\rho, t)$ ,  $I_{\text{eccd}}(t)$ ,  $\chi_e(\rho, t)$ , have been varied during a simulation. The other parameters ( $\kappa_a(t)$ ,  $\delta_a(t)$ ,  $P_{\text{EC}}(\rho, t)$ ,  $n_e(\rho, t)$ ,  $T_i(\rho, t)$ ,  $I_p(t)$ ) have been kept fixed, which is often difficult to realize experimentally. In this numerical context, the modulation of ECCD (and in certain cases of  $T_e$ ) is, indeed, the main actuator for the transport properties modifications.

For the analysis of Swing ECCD, the ASTRA transport code has been employed in both predictive and interpretative modes, using a magnetic shear-dependent model (the Rebut-Lallia-Watkins model, RLW, [70]) for the calculation of the electron energy diffusion coefficient. Modified versions of the RLW model have also been used to account for different dependencies on the magnetic shear. As already specified in Chap. 2, the modeling is based on the coupling of the predictive or interpretative ASTRA simulations with the experimental data and the quasi-linear CQL3D Fokker-Planck code for the computation of the ECRH and ECCD sources. The radial particle diffusion is taken into account (required due to the effect of fast particle transport, see [49]) as proportional to the electron heat diffusion. The methodology to determine  $I_{\text{eccd}}$  requires a steady state, whereas Swing ECCD discharges are intrinsically in a transient state. An accurate determination of the value of the total EC current driven can only be obtained by increasing the period of the EC modulation, so as to reach a steady state during each of the co- and counter

phases, however this has not been done experimentally. Nevertheless, in order to have an estimate of the  $j_{\text{eccd}}$  profile, the proportionality coefficient  $D_0$  between the electron energy and particle coefficients has been fixed to a typical value used in various previous calculations of other plasma discharges: therefore,  $D_0 = 0.2$  has been used for the two analyzed discharges. The  $j_{\text{eccd}}$  profiles and corresponding values of  $I_{\text{eccd}}$  calculated by CQL3D with  $D_0 = 0.2$  are shown in Fig. 4.7

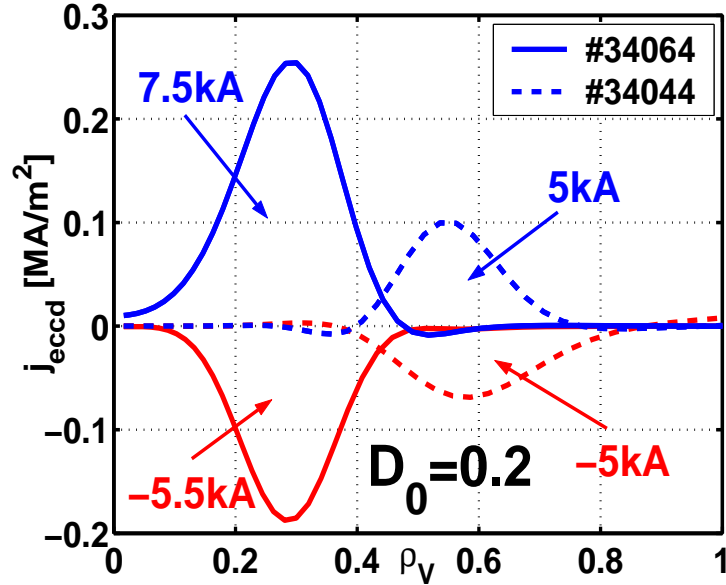


Figure 4.7:  $j_{\text{eccd}}$  profiles (and corresponding values of  $I_{\text{eccd}}$ ) calculated by CQL3D with  $D_0 = 0.2$ . These profiles have been used in all the following ASTRA simulations of Swing ECCD discharges.

The different simulating models considered in the present analysis are the following:

1. An interpretative analysis, in which the measured electron temperature profile,  $T_e(\rho, t)$ , has been provided as a time-varying input (see Sec. 2.4.1).
2. A predictive model, the so-called Rebut-Lallia-Watkins (RLW) semi-empirical local transport model [70], in which the electron heat diffusion coefficient,  $\chi_e$ , is proportional to  $q/s$  (see Sec. 2.4.2).
3. Other predictive models with different dependences on the magnetic shear (linear, quadratic and inversely quadratic). These models are essentially a variation of the RLW model, respectively multiplied by the square, the cube, or divided by

the magnetic shear. In the following analysis, they will be indicated respectively as  $RLW \cdot s$ ,  $RWL \cdot s^2$  and  $RLW/s$ . These modified models were used in order to compare the effect on  $T_e$  with a model having a different dependence of the electron heat diffusion coefficient on the magnetic shear (see Sec. 2.4.2).

### 4.3.1 Rebut-Lallia-Watkins model

Semi-empirical models can involve physical ideas like simplified theoretical models, dimensional analysis, critical gradients, etc., but they mainly determine the parametric dependence and magnitude of particle and heat diffusivities by experimental comparisons, and are therefore very different in origin than respect to theory-based models. The semi-empirical Rebut-Lallia-Watkins (RLW) local transport model has been validated to well reproduce TCV discharges [55]. It involves a critical electron temperature gradient: when the electron temperature gradient exceeds the critical value, a turbulent behavior in the magnetic topology is triggered. The electron heat transport coefficient consists of two contributions, the neoclassical and anomalous ones, therefore one can write:  $\chi_e = \chi_{e,neo} + \chi_{e,an}$ , where the anomalous coefficient is given by:

$$\chi_{e,an} = \frac{C_{e,an}}{B_\phi} \sqrt{\frac{\epsilon(1 + Z_{eff}) T_e}{R_0} \frac{T_e}{T_i}} \left| \left( \frac{\nabla T_e}{T_e} + 2 \frac{\nabla n_e}{n_e} \right) \frac{q\rho}{s} \right| \left( 1 - \frac{\nabla T_{RLW}}{\nabla T_e} \right) H(\nabla T_e - \nabla T_{RLW}), \quad (4.1)$$

where  $H(x)$  is the Heaviside step function, and the critical electron temperature gradient is given by the expression:

$$\nabla T_{RLW} = \frac{C_{gcrt}}{q} \sqrt{\frac{\eta j B_\phi^3}{n_e \sqrt{T_e}}}, \quad (4.2)$$

$\eta$  being the neoclassical resistivity. Note that the critical value of  $T_e$  is essentially negligible outside the deposition region in case of ECH heated plasmas. In the RLW model, an increase on the local magnetic shear, with the safety factor relatively constant, induces a reduction of transport,  $\chi_e \sim |q/s|$ , which is adequate for TCV discharges in case of negative or large positive magnetic shear. To test a different dependence, a modified version of the RLW local transport model has also been taken into account, with a linear magnetic shear dependence.

The two free parameters  $C_{e,\text{an}}$  and  $C_{\text{gcrt}}$  of the transport models have been adjusted until they adequately reproduce the measured  $T_e$  for a pure ECH discharge, then subsequently held at those values. The resulting simulated profiles are shown in Fig. 4.8a, for the RLW, and Fig. 4.8b, for one of the modified RLW model. At this on-axis deposition, for instance, the values obtained in this way are  $C_{e,\text{an}} = 0.6$  and  $C_{\text{gcrt}} = 1$  for the RLW model (4.8a), and  $C_{e,\text{an}} = 0.7$  and  $C_{\text{gcrt}} = 0.5$  for the RLW $\cdot s^2$  model (4.8b). The determined values have been kept unvaried during the simulations of the Swing ECCD discharges.

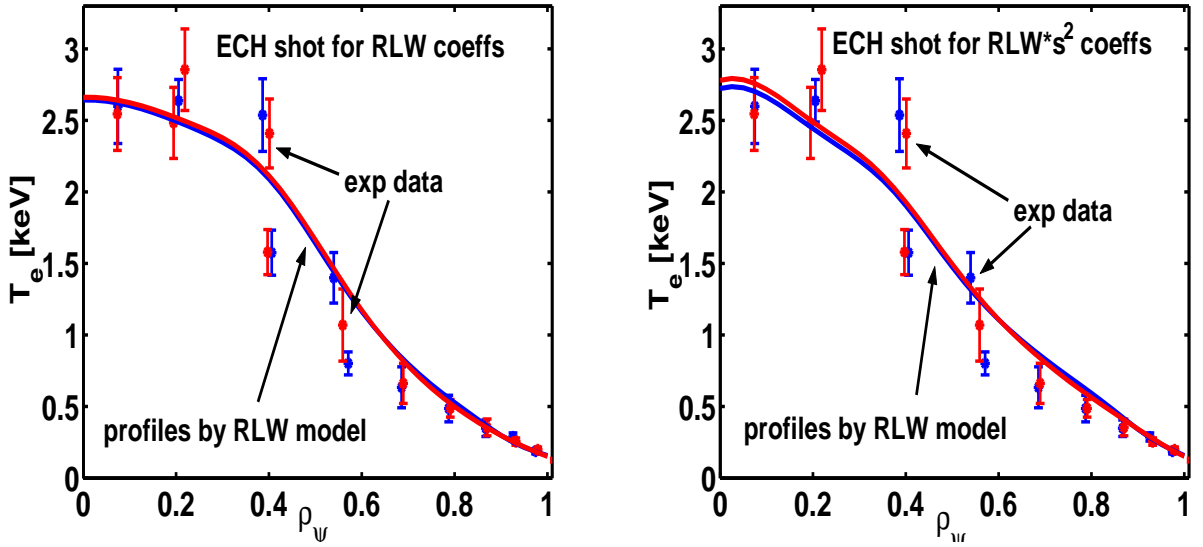


Figure 4.8: *Simulated electron temperature profiles of an ECH discharge used to determine the free coefficients of the RLW and the modified RLW $\cdot s^2$  model so as to accurately reproduce the experimental profiles. The values obtained are  $C_{e,\text{an}} = 0.6$  and  $C_{\text{gcrt}} = 1$  for the RLW model and  $C_{e,\text{an}} = 0.7$  and  $C_{\text{gcrt}} = 0.5$  for the RLW $\cdot s^2$  model.*

## 4.4 Numerical results

The following numerical analysis was carried out for the TCV discharges #34064 ( $\rho_{\text{dep}} = 0.3$ ) and #34044 ( $\rho_{\text{dep}} = 0.55$ ), described in Sec. 4.2.2. The modulation period of these discharges is 200ms. Therefore, in the following simulations the full co-ECCD and full counter-ECCD phases have been fixed to 95ms each. The imposed time switch from one phase to the other is 5ms, of the order of the electron energy confinement time. The transition from one Swing ECCD phase to the other is imposed in such a way that the

profiles of  $j_{\text{eccd}}$  and  $T_e$  (when prescribed) are varied in time following a linear interpolation between the two co- and counter-ECCD profiles during 5ms; then, the profiles are held constant for 95ms. During this modulation period of 200ms, the plasma does not reach a full steady state, as the simulated parallel electric field is not yet relaxed. Simulations with much longer modulation times have also been done, identifying the modulation period for steady state to be around 600ms, in order to have 300ms with constant conditions.

#### 4.4.1 Interpretative simulations results

For the interpretative simulations, two cases have been taken into account: a fixed  $T_e$  simulation, in which the electron temperature has been maintained constant throughout the simulation, and a time-varying  $T_e$  simulation, in which the prescribed electron temperature is varied between the two profiles measured by the Thomson Scattering system. In the first case, the modulation of the magnetic shear is only due to the change between co- and counter-ECCD, whereas in the second case the electron temperature profile variation acts as a second actuator (along with  $j_{\text{eccd}}$ ). The analysis is divided into two subsections dedicated respectively to on-axis and off-axis interpretative simulations of Swing ECCD.

##### On-axis magnetic shear modulation

Fig. 4.9 shows the calculated time traces of the various plasma current components and the prescribed central  $T_e$ , at fixed or time-varying  $T_e$  for the TCV discharge #34064 ( $\rho_{\text{dep}} = 0.3$ ). As a consequence of the imposed modulation on  $I_{\text{eccd}}$  (and  $T_e$  for Fig. 4.9b),  $I_{\text{ohm}}$  is also modulated, whereas the modulation effect on  $I_{\text{bs}}$  is essentially negligible, even in the case of time-varying  $T_e$ . The value of  $I_{\text{eccd}}$ , calculated by CQL3D with  $D_0 = 0.2$ , oscillates between 7.5kA and -5.5kA.

Fig. 4.10 compares the simulated magnetic shear profiles of both interpretative cases. The modulation of  $s$  reaches its maximum variation at the radial location of the EC deposition,  $\rho_{\text{dep}} = 0.3$ , and is essentially independent of the temperature profile. With co-ECCD the value of  $s$  at  $\rho_V = 0.3$  is about 0.5, whereas it increases to about 0.75 when the counter-ECCD is injected. Therefore for both cases, the reconstructed magnetic shear profile increases by 50% around the deposition location, when passing from the higher confinement co-ECCD to the lower confinement counter-ECCD phase; simultaneously, the central electron temperature is experimentally observed to drop by 15%. The radial extent



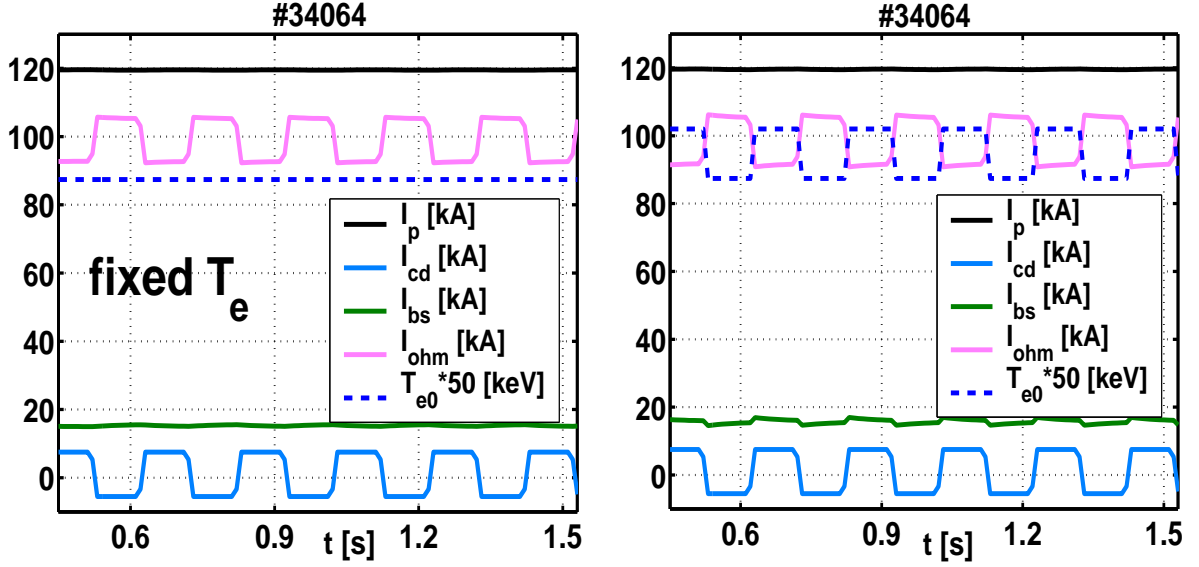


Figure 4.9: Simulated or imposed time traces of the various plasma current components and the imposed central  $T_e$ , respectively at fixed (a) or time-varying (b)  $T_e$ . In the ASTRA modeling,  $I_p$ ,  $I_{cd}$  and  $T_e$  are imposed, whereas  $I_{bs}$  and  $I_{ohm}$  are calculated.

of the region in which  $\Delta s = s^{\text{counter}} - s^{\text{co}} > 0$  coincides with the deposition width of  $P_{EC}$ . The magnetic shear profiles are nevertheless modulated to the outside of the deposition region ( $\rho_V > 0.4$ ), with a smaller and negative  $\Delta s$ , whereas they are not modified to the inside of it ( $\rho_V < 0.1$ ). The minimum and maximum values of the magnetic shear, within the radial region where the modulation is observed, are 0.1 and 0.9 (at  $\rho_V = 0.1$  and  $\rho_V = 0.4$  respectively).

For the time-varying  $T_e$  case, the  $q$  profiles are also shown in Fig. 4.11a, along with the EC deposition power, which is constant throughout all simulations. These simulations do not take into account a model for the sawtooth crash, as sawteeth are not experimentally observed in the analyzed discharges. As shown in Fig. 4.11a, the simulated  $q = 1$  surface is inside  $\rho_V = 0.1$ , therefore if a sawtooth crash did occur, the mixing radius would be very small and should not affect the other reconstructed profiles in the region around  $\rho_V = 0.3$ .

Fig. 4.11b shows the time evolution of the parallel electric field profile,  $E_{\parallel}$ , simulated during the switch from co- to counter-ECCD phase. The profiles are plotted every 10ms, with the blue and red profiles being the first and last respectively. A large and rapid variation of the local  $E_{\parallel}$  is observed at the location of the deposition radius: the main

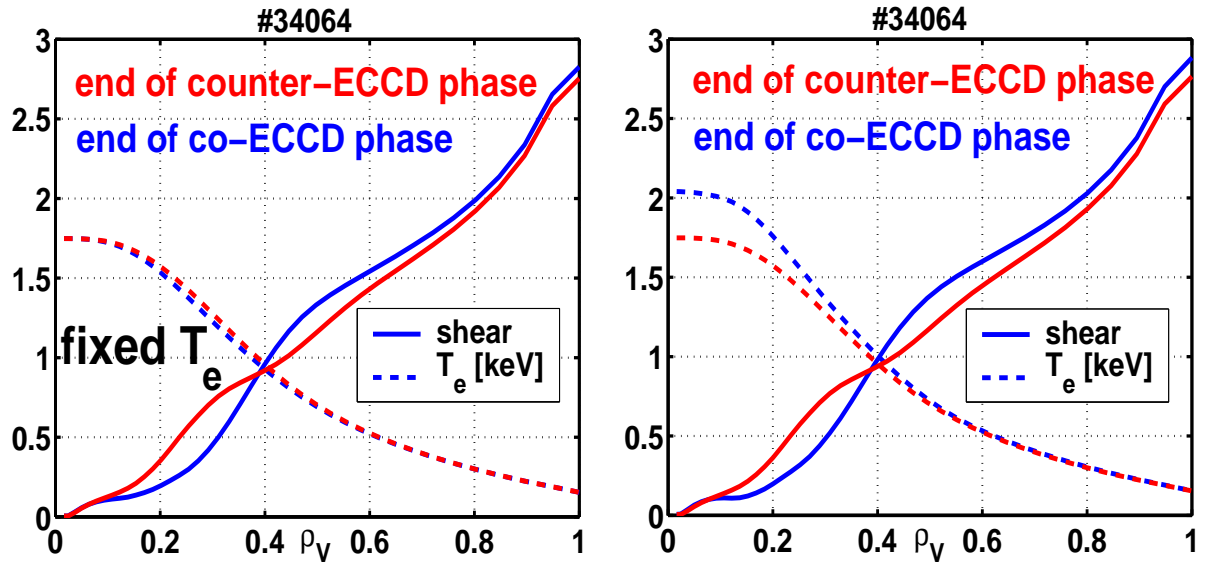


Figure 4.10: *Simulated magnetic shear and imposed electron temperature profiles for the fixed (a) and time-varying (b)  $T_e$  cases.*

change occurs during the first 20ms following the imposed flip in ECCD sign. The initial and final profiles are not completely relaxed (flat) yet, therefore a steady state is not reached within 100ms.

Finally, the simulated edge loop voltage is shown to be in agreement with the measured time trace in Fig. 4.12 (for the time-varying  $T_e$  case). The experimental value of  $Z_{\text{eff}} = 3$  has been used in the modeling, and the agreement of the measured and reconstructed  $V_{\text{loop}}$  is still maintained if the value of  $Z_{\text{eff}}$  is increased to 3.5. It should be noted that all simulations described in this Chapter have been performed by fixing the value of the plasma current  $I_p$ , and leaving  $V_{\text{loop}}$  free to evolve according to the other calculated and measured quantities.

### Off-axis magnetic shear modulation

Fig. 4.13 shows the calculated time traces of the various plasma current components and the prescribed central  $T_e$ , at fixed or time-varying  $T_e$  for the TCV discharge #34044 ( $\rho_{\text{dep}} = 0.55$ ). As observed in the more on-axis interpretative simulations,  $I_{\text{ohm}}$  is modulated, because of the imposed modulation on  $I_{\text{eccd}}$  and  $T_e$ , whereas the modulation effect on  $I_{\text{bs}}$  is negligible. The value of  $I_{\text{eccd}}$ , calculated by CQL3D with  $D_0 = 0.2$ , oscillates between 5kA and -5kA, as shown in Fig. 4.7.

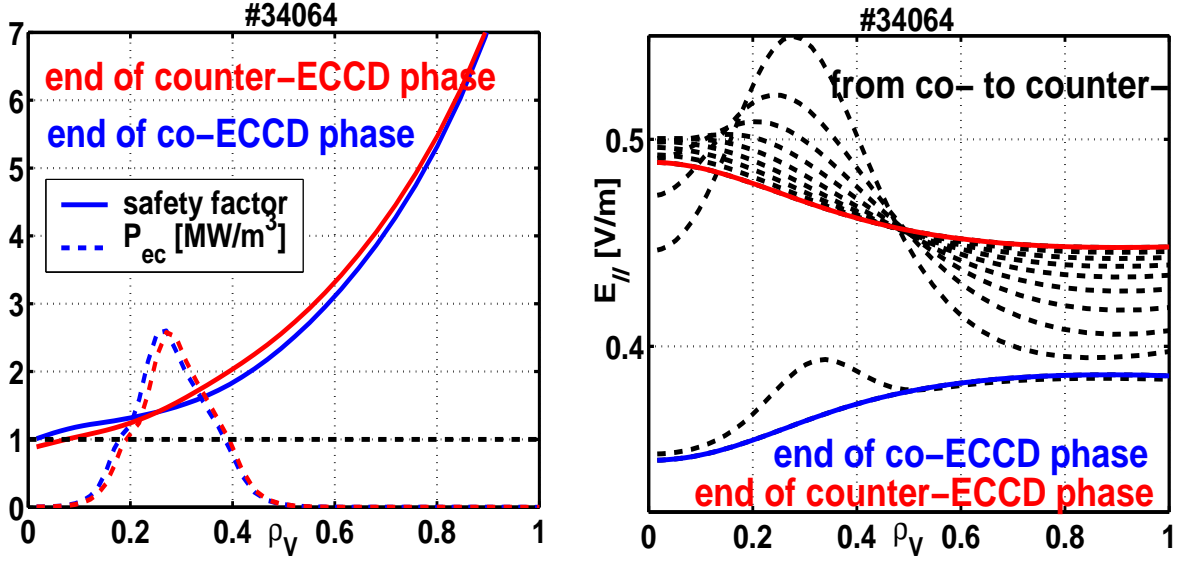


Figure 4.11: Simulated safety factor and EC power density deposition profiles (a) and parallel electric field,  $E_{||}$ , simulated during the switch from co- to counter-ECCD phase (b) for the time-varying  $T_e$  case. Starting from the end of the co-ECCD phase,  $E_{||}$  is then plotted every 10ms until the end of the counter-ECCD phase is reached.

Fig. 4.14 compares the simulated magnetic shear profiles of both interpretative cases. The modulation of  $s$  reaches its maximum variation at the radial location of the EC deposition, at  $\rho_{dep} = 0.55$ , and is independent of the temperature profile, as found in the on-axis case. With co-ECCD the value of  $s$  at  $\rho_V = 0.55$  is 0.7, whereas it increases to about 1.1 when the counter-ECCD is injected. Therefore an increment of 50% in  $s$  around the deposition location is again obtained for both interpretative cases, when passing from the lower confinement co-ECCD to the higher confinement counter-ECCD phase. Contrary to the on-axis case, the central electron temperature is experimentally observed to increase by 25%. The radial extent of the region in which  $\Delta s > 0$  again coincides with the deposition width of  $P_{EC}$  ( $0.4 < \rho_V < 0.8$ ). The magnetic shear profiles are essentially not modulated, neither to the inside nor to the outside of the deposition width. The minimum and maximum values of the magnetic shear in the radial region where the modulation is observed are 0.7 and 1.7 (at  $\rho_V = 0.4$  and  $\rho_V = 0.8$  respectively).

For the time-varying  $T_e$  case, the  $q$  profiles are also shown in Fig. 4.15a, along with the EC deposition power, which is constant throughout all simulations. The modeled  $q$  profile

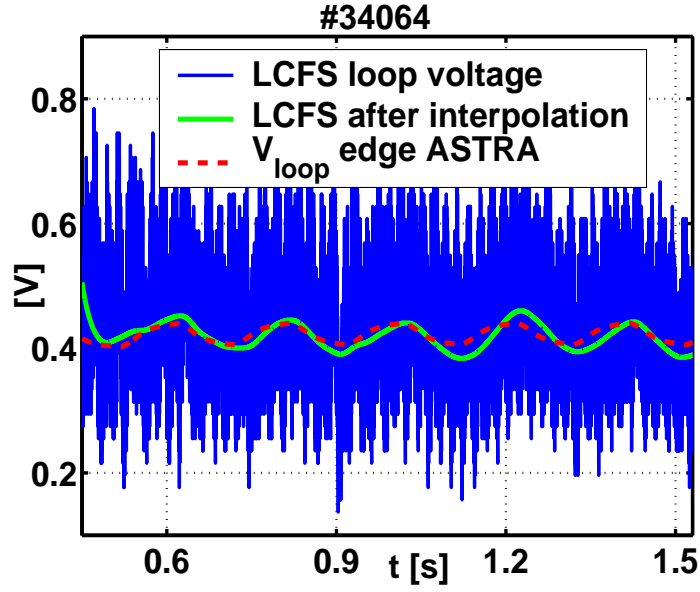


Figure 4.12: Time trace of the measured loop voltage (noisy blue line), corresponding filtered signal by interpolation, and ASTRA simulated loop voltage (at constant  $I_p$ ) for the time-varying  $T_e$  case and with  $Z_{\text{eff}} = 3$ . The simulated  $V_{\text{loop}}$  is still in agreement with the experimental one if  $Z_{\text{eff}}$  varied between 3 and 3.5.

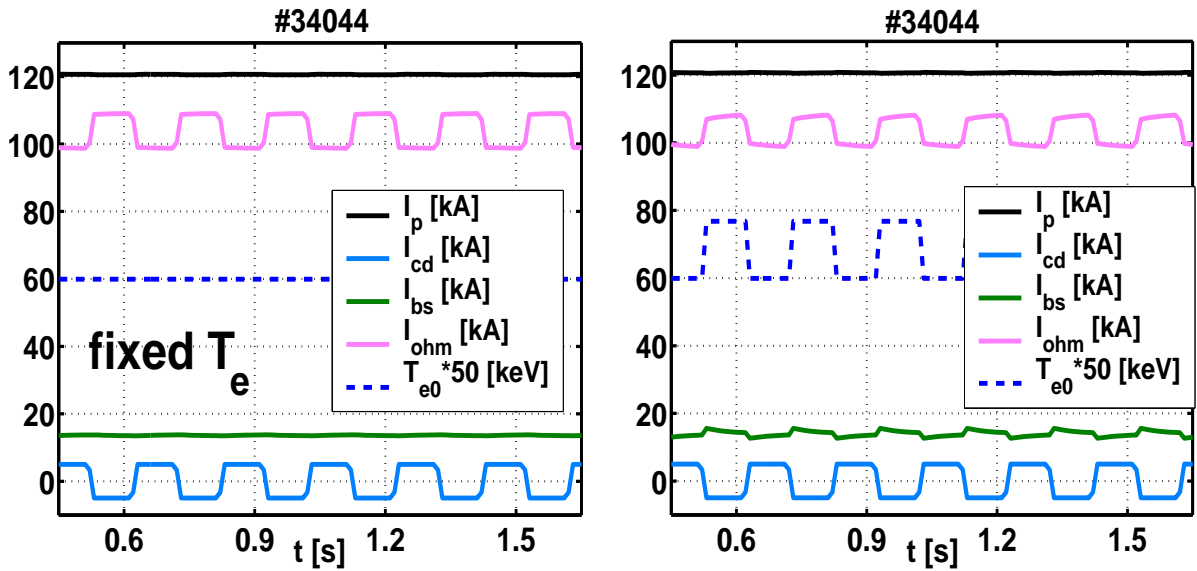


Figure 4.13: Simulated or imposed time traces of the various plasma current components and the imposed central  $T_e$ , respectively at fixed (a) or time-varying (b)  $T_e$ . In the ASTRA modeling,  $I_p$ ,  $I_{\text{cd}}$  and  $T_e$  are imposed, whereas  $I_{\text{bs}}$  and  $I_{\text{ohm}}$  are calculated.

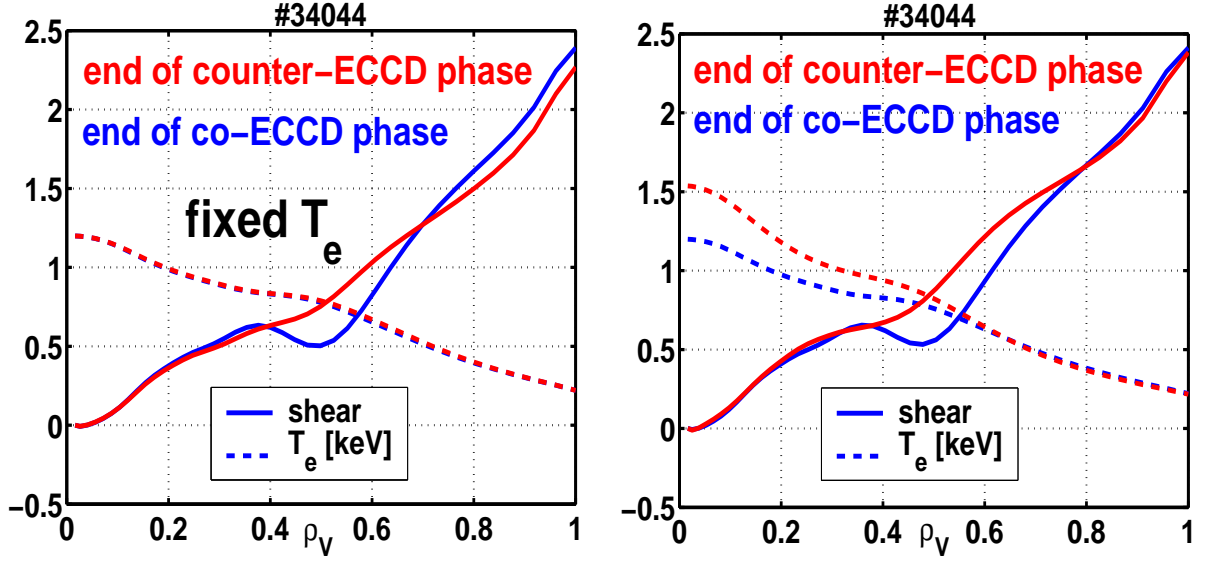


Figure 4.14: Simulated magnetic shear and imposed electron temperature profiles for the fixed (a) and time-varying (b)  $T_e$  cases.

appears modulated as well, with the maximum  $\Delta q$  at  $\rho_V = 0.55$  of 0.5.

Fig. 4.15b shows the time evolution of the parallel electric field profile,  $E_{\parallel}$ , simulated during the switch from co- to counter-ECCD phase, for the time-varying  $T_e$  case. The profiles are plotted every 10ms, with the blue and red profiles being the first and last, respectively. A large and rapid variation of the local  $E_{\parallel}$  is observed just outside the location of the deposition radius: the main change occurs during the first 20ms following the imposed flip in ECCD sign.

Finally, the simulated edge loop voltage is shown to be in agreement with the measured time trace in Fig. 4.16 (for the time-varying  $T_e$  case). The experimental value of  $Z_{\text{eff}} = 3$  has been used in the modeling presented, and the agreement of the measure and reconstructed  $V_{\text{loop}}$  is still maintained if the value of  $Z_{\text{eff}}$  is increased to 3.5.

#### 4.4.2 Predictive simulations results

In the case of predictive simulations, the electron energy diffusion coefficient,  $\chi_e$ , is calculated based on the RLW (or a modified RLW) model, which has an explicit dependence in  $s$ . The principal difference with respect to the interpretative cases is that now an imposed change in the current density profile (due to the Swing ECCD) will also affect the  $s$ -dependent  $\chi_e$  profile. This, in turn, will change the conductivity and bootstrap

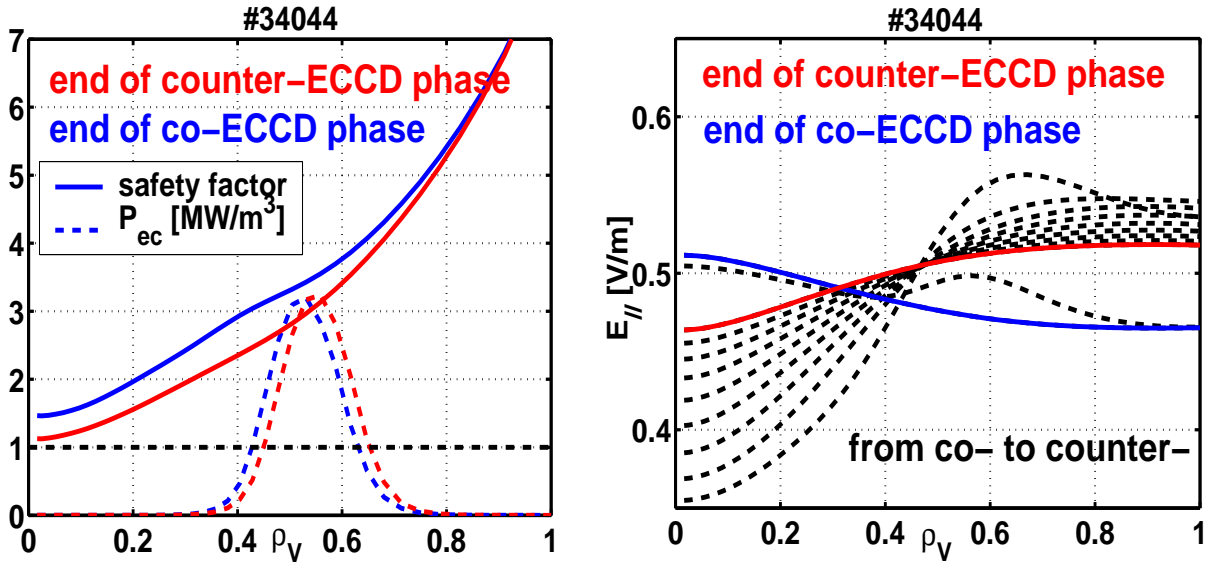


Figure 4.15: Simulated safety factor and EC power density deposition profiles (a) and parallel electric field,  $E_{||}$ , simulated during the switch from co- to counter-ECCD phase (b) for the time-varying  $T_e$  case. Starting from the end of the co-ECCD phase,  $E_{||}$  is then plotted every 10ms until the end of the counter-ECCD phase is reached.

coefficients, therefore influencing  $j$  again. With the difference in confinement properties observed for the two depositions taken into account, the usual RLW fails to reproduce the observed electron temperature trend (i.e.  $T_e^{\text{co}} > T_e^{\text{counter}}$  for on-axis deposition and  $T_e^{\text{counter}} > T_e^{\text{co}}$  for off-axis deposition). For this reason, differing corrections to the RLW model have been used for the separate discharges analyzed. Like previously, the analysis is divided into two subsections dedicated respectively to on-axis and off-axis predictive simulations of Swing ECCD.

### On-axis magnetic shear modulation

Fig. 4.17 shows the calculated time traces of the various plasma current components and the calculated central  $T_e$  with the RLW and the RLW $\cdot s^2$  for the TCV discharge #34064 ( $\rho_{\text{dep}} = 0.3$ ). As a consequence of the imposed modulation on  $I_{\text{eccd}}$  and the  $s$ -dependent  $\chi_e$ ,  $I_{\text{ohm}}$ ,  $T_{e0}$  and, to a minor extent,  $I_{\text{bs}}$  are also modulated. The central  $T_e$  modulations are shifted by 180° depending on the model employed: the correct behavior is obtained with the RLW $\cdot s^2$  model, which depends linearly on  $s$ . Indeed, the simulated  $s$  profile is such that  $s^{\text{counter}} > s^{\text{co}}$ , as shown in Fig. 4.18. Therefore an inversely proportional dependence

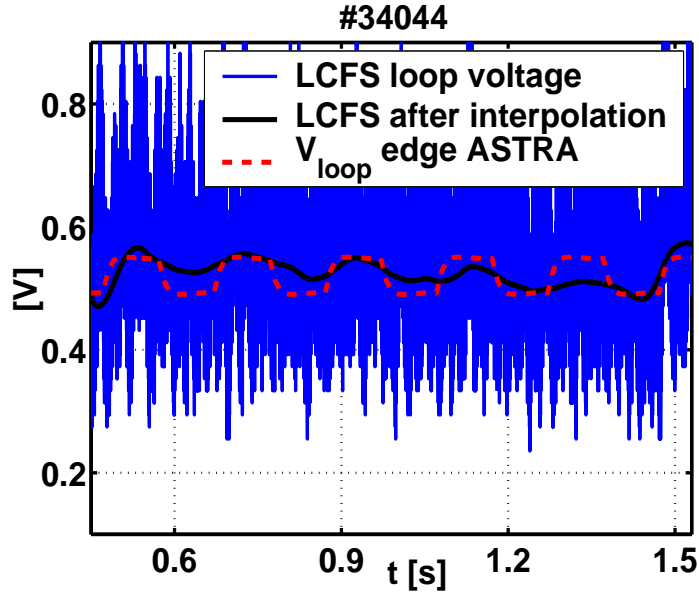


Figure 4.16: Time trace of the measured loop voltage (black noisy line), corresponding filtered signal by interpolation, and ASTRA simulated loop voltage (at constant  $I_p$ ) for the time-varying  $T_e$  case and with  $Z_{\text{eff}} = 3$ . The simulated  $V_{\text{loop}}$  is still in agreement with the experimental one if  $Z_{\text{eff}}$  varied between 3 and 3.5.

on  $s$ , as that of the RLW model, is expected to fail in reproducing the observed electron temperature profiles. On the other hand, the  $T_e$  profiles simulated with the RLW· $s^2$  model are very close to the experimental ones of Fig. 4.10b.

For both models, the maximum  $\Delta s$  is found to be  $\Delta s = 0.3$  at the radial location of the EC deposition,  $\rho_{\text{dep}} = 0.3$ . The absolute values of  $s(\rho_V = 0.3)$  are slightly different, with the RLW case yielding lower values. It is again found that the radial extent of the region in which  $\Delta s = s^{\text{counter}} - s^{\text{co}} > 0$  coincides with the deposition width of  $P_{\text{EC}}$ . The minimum and maximum values of the magnetic shear in the radial region where the power is deposited are 0.1 and 0.9 (at  $\rho_V = 0.1$  and  $\rho_V = 0.4$  respectively). Therefore, the location and extent of the shear modulation for both models are in good agreement with the interpretative results described above.

For the RLW· $s^2$  case, the  $q$  profiles are also shown in Fig. 4.19, along with the EC deposition power, which is constant throughout all simulations.

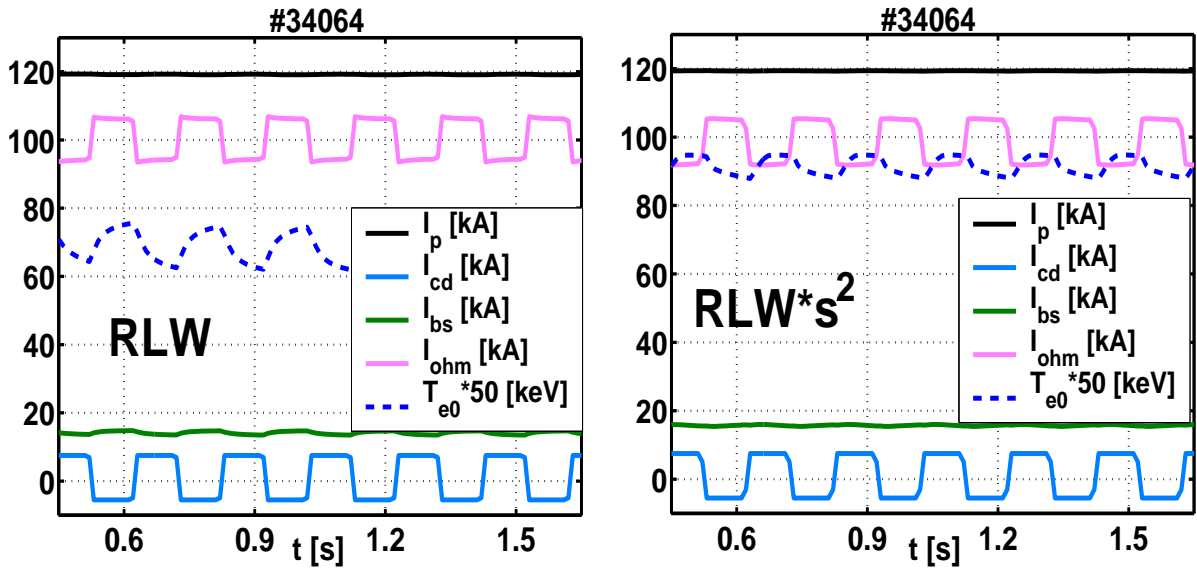


Figure 4.17: Simulated or imposed time traces of the various plasma current components and the calculated central  $T_e$ , respectively obtained with the RLW (a) or the modified RLW $\cdot s^2$  (b) models. In the ASTRA modeling,  $I_p$  and  $I_{cd}$  are imposed, whereas  $I_{bs}$ ,  $I_{ohm}$  and  $T_e$  are calculated.

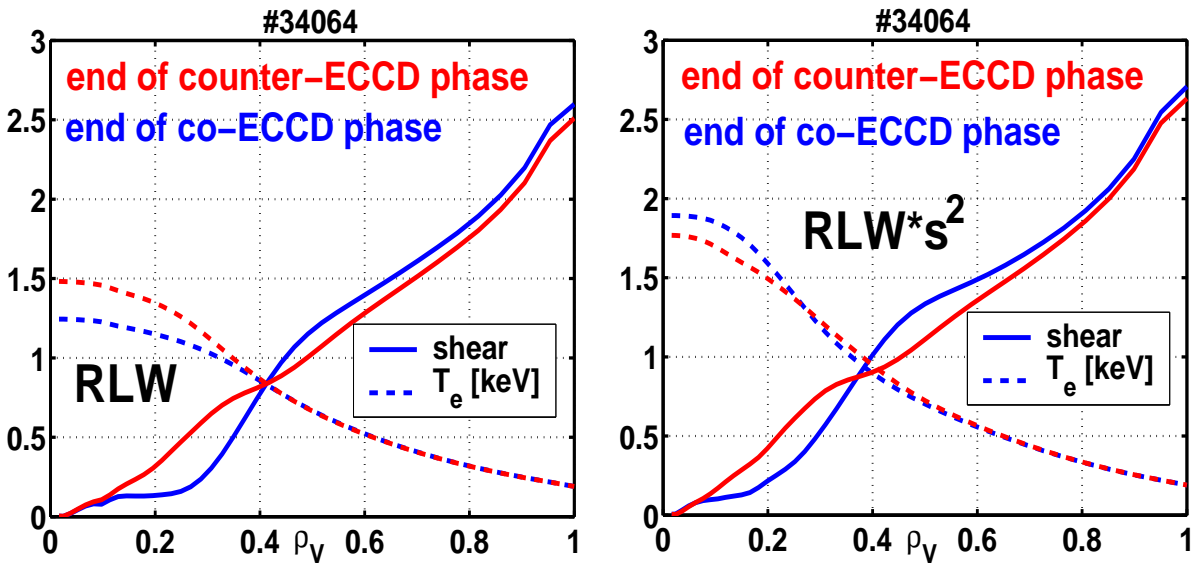


Figure 4.18: Simulated  $s$  and  $T_e$  profiles, respectively obtained with the RLW (a) or the modified RLW $\cdot s^2$  (b) models.

### Off-axis magnetic shear modulation

Fig. 4.20 shows the calculated time traces of the various plasma current components and the calculated central  $T_e$  with the RLW and the RLW/s for the TCV discharge #34044



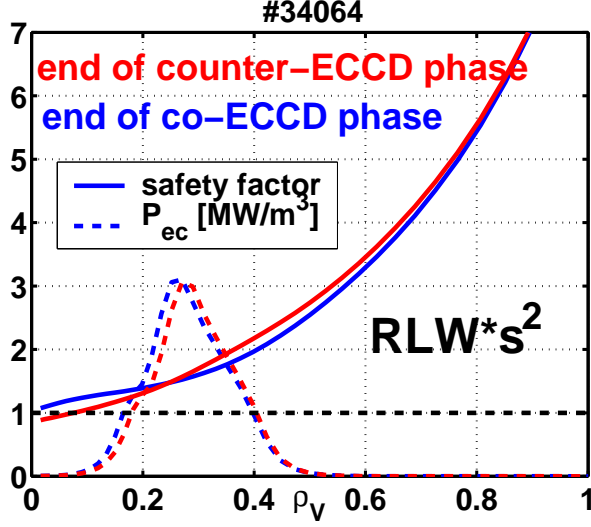


Figure 4.19: *Simulated  $q$  and  $P_{\text{EC}}$  profiles obtained with the modified  $RLW \cdot s^2$  model.*

( $\rho_{\text{dep}} = 0.55$ ).  $I_{\text{ohm}}$ ,  $T_{e0}$  and, to a minor extent,  $I_{\text{bs}}$  are also modulated due to the imposed modulation on  $I_{\text{eccd}}$  and the  $s$ -dependent  $\chi_e$ . The simulated  $s$  profile is such that  $s^{\text{co}} > s^{\text{counter}}$ , as shown in Fig. 4.21. The central  $T_e$  modulations follow the same trend, since the models employed both have an inverse dependence on  $s$ . However, a stronger dependence in the magnetic shear, such as  $\sim 1/s^2$  is required in order to obtain a difference in  $T_e$  at  $\rho_V = 0.4$  (just inside the  $P_{\text{EC}}$  deposition) of the same order as observed experimentally (Fig. 4.21b versus Fig. 4.14b).

The magnetic shear behaviour is qualitatively the same in both cases, with  $\Delta s \sim 0.3$  around the deposition location. Even though the extent of the shear modulation is found to be in good agreement with the corresponding interpretative results, the amplitude of the modulation is smaller: the minimum and maximum values of the magnetic shear in the radial region where the power is deposited are 0.4 and 1.1 (at  $\rho_V = 0.4$  and  $\rho_V = 0.8$  respectively). For the  $RLW/s$  case, the  $q$  profiles are also shown in Fig. 4.22, along with the EC deposition power.

#### 4.4.3 Discussion on the numerical results

The results arising from these simulations have linked the observed modification of local electron transport to the modulation of the magnetic shear profile at the deposition of the EC injection. In all cases studied,  $s^{\text{cnt}}$  is larger than  $s^{\text{co}}$  within the radial width of

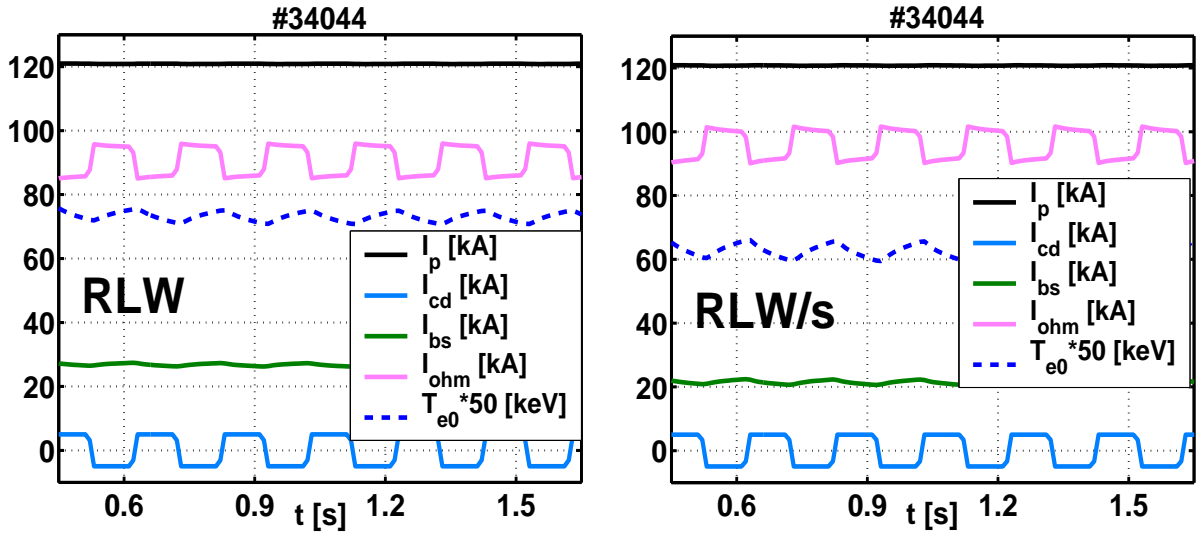


Figure 4.20: Simulated or imposed time traces of the various plasma current components and the calculated central  $T_e$ , respectively obtained with the RLW (a) or the modified RLW/s (b) models. In the ASTRA modeling,  $I_p$  and  $I_{cd}$  are imposed, whereas  $I_{bs}$ ,  $I_{ohm}$  and  $T_e$  are calculated.

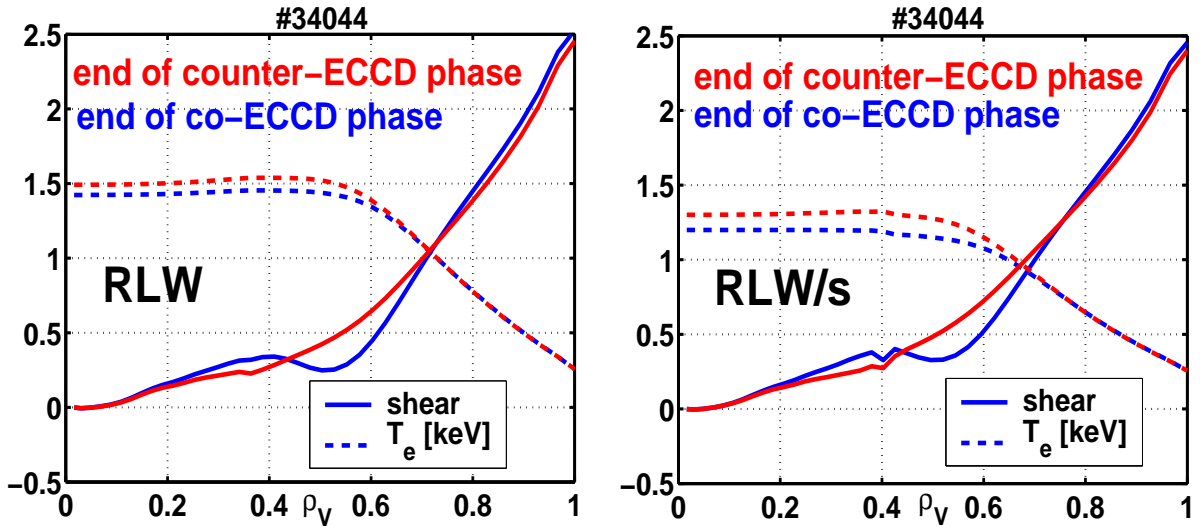


Figure 4.21: Simulated  $s$  and  $T_e$  profiles, respectively obtained with the RLW (a) or the modified RLW/s (b) models.

the EC deposition, regardless of the experimental or calculated  $T_e$ .

In the interpretative cases for the on-axis deposition location, the values of the magnetic shear affected by the modulation range from 0.1 to 0.9. For the off-axis deposition location, the values of the magnetic shear affected by the modulation range from 0.7 to 1.7. Since at

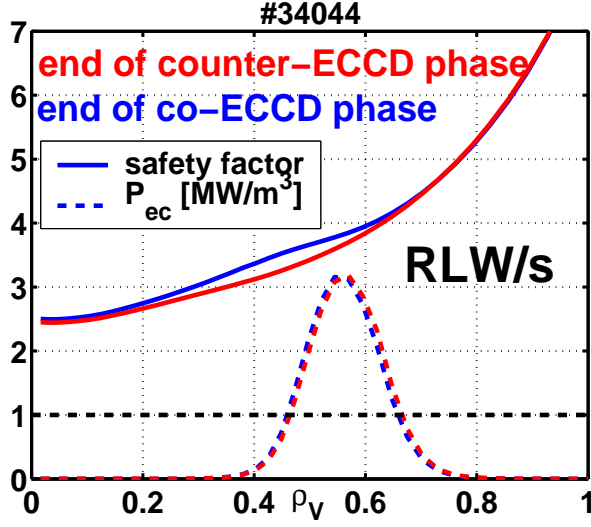


Figure 4.22: *Simulated  $q$  and  $P_{EC}$  profiles obtained with the modified RLW/d models*

these two locations the electron confinement exhibits inverse properties, these simulations confirm the inversion of electron transport between low and high values of the magnetic shear, as predicted by gyrokinetic linear simulations [82], [69].

In the predictive cases, for the on-axis deposition location, the values of the magnetic shear affected by the modulation also range from 0.1 to 0.9. For the off-axis deposition location, the values of the magnetic shear affected by the modulation range from 0.4 to 1.1. These latter are still high enough to be in agreement with the predictions from micro turbulence.

Additionally, the results confirm the robustness of the magnetic shear modeling, indicating that the main contribution comes from the  $j_{eccd}$  modulation.

The interpretative, on-axis, time-varying  $T_e$  case has moreover confirmed a previous modeling based on electrodynamics calculations, discussed in Ref. [19]. The main results arising from such modeling were that, in the deposition region,  $s$  passes from 0.2 to 0.7 while switching from the co- to counter-phase, and  $q(\rho_{dep})$  oscillates between respectively 1.2 and 1.4. The  $j_{eccd}$  profiles used in the previous modeling had been determined by the linear Toray-GA code, while for the present calculations the co- and counter-ECCD profiles have been calculated by solving the Fokker-Planck equation, including radial particle diffusion, resulting in ECCD profiles slightly broader than the ones predicted by linear theory. Nevertheless, the two models have shown similar relative changes in the magnetic

shear modulation.

## 4.5 MHD activity in Swing ECCD discharges

Previous to the experiments analyzed in this Chapter, a number of other Swing ECCD discharges had been realized with larger EC power (i.e. 2+2 or even 3+3 gyrotrons) and feedback control on the plasma elongation. These were initially carried out with the purpose of creating a large database featuring different values of the plasma current, radial deposition location, and width of the deposited power. Unfortunately these discharges have been found to systematically exhibit MHD activity, so that, when the modulation of  $T_e$  is observed, it is not easy to attribute it uniquely to the magnetic shear oscillation. This obviously complicates the correct interpretation of the measured electron temperature modulation. Nevertheless, one can clearly observe that the mode activity is very intense during all co-ECCD phases and fades out when switching to counter-ECCD, as seen in the spectrogram of Fig. 4.23.

This confirms experimentally that the  $q$  profile is, indeed, being modified locally, but may also explain the fact that no significant effect on  $T_e$  has been observed in these discharges. However, the identification of the toroidal and poloidal mode numbers for these modes allows a possible validation of the ASTRA modeling by comparison with the simulated rational  $q$  surfaces. For the discharge shown in Fig. 4.23 (#30675), the mode has been identified as a  $m/n = 3/1$  one, located approximately in the region  $0.4 < \rho_\psi < 0.5$ . Therefore an interpretative ASTRA simulation has been carried out, in order to model the safety factor profile and identify the  $q = 3$  surface location. The model has employed Gaussian ECCD profiles, centered at the EC deposition and scaled to provide the  $I_{\text{eccd}}$  calculated by Toray-GA. Results from this simulation are shown in Fig. 4.24. The  $q$  profile during the co-ECCD phase crosses  $q = 3$  at  $\rho_\psi \sim 0.5$ , consistent with the mode location, whereas the surface is pushed outwards at  $\rho_\psi \sim 0.65$  during the counter-ECCD phase. Further analysis of the modes in these experiments is beyond the scope of this thesis, but these modeled  $q$  and  $s$  profiles form an excellent basis for tearing mode studies and the effect of local current density profile perturbations.

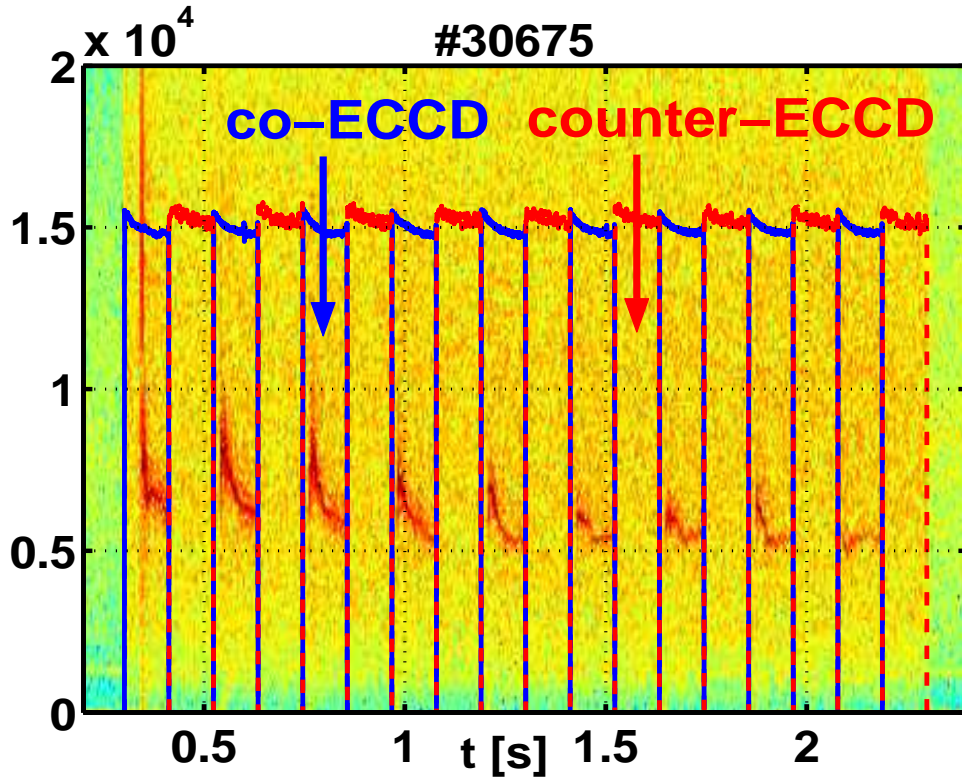


Figure 4.23: Spectrogram revealing the presence of MHD activity, with alternated phases of appearance and absence, for TCV discharge #30675. The modulation frequency is that of the Swing ECCD injection (45Hz). The EC total power is in arbitrary units.

## 4.6 Summary and conclusions

The study on Swing ECCD has confirmed the link between the electron transport and the magnetic shear, both of which are modulated around the EC deposition region. The numerical modeling has allowed us to completely decouple the effects of the current profile modification from those of slight plasma heating misbalance or non-constant plasma elongation - a rather delicate experimental issue. The location and extent of the shear modulation has been shown to be essentially independent of the transport model employed, confirming the robustness of the magnetic shear modeling and indicating that the main contribution is due to  $j_{eccd}$ . The numerical results have moreover validated a previous rough model based on electrodynamics calculations, which found comparable magnetic shear variations.

The experimental electron temperature shows that, at on-axis deposition locations, during

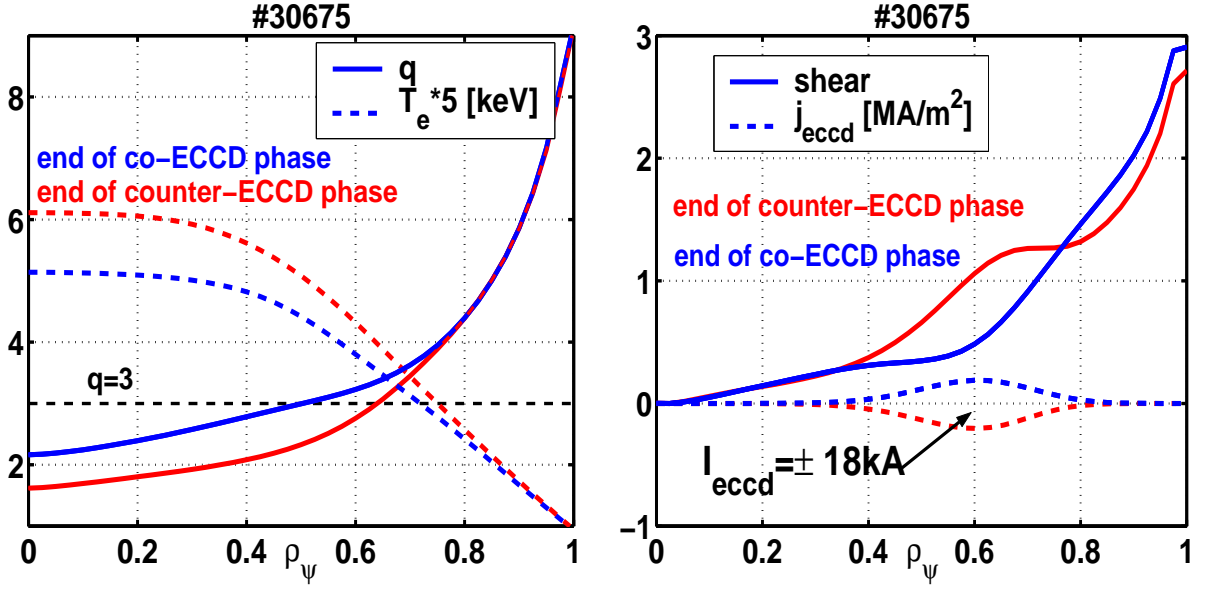


Figure 4.24: Simulated  $q$  and  $s$  profiles, and imposed  $T_e$  and  $j_{\text{eccd}}$  profiles of the interpretative modeling of #30675.

the co-ECCD phase  $T_e$  is higher than that in the counter-ECCD phase. Conversely, for off-axis deposition locations, during the co-ECCD phase  $T_e$  is lower than that in the counter-ECCD phase. The modeled local magnetic shear modulation ranges from 0.1 to 0.9 in the on-axis discharge, whereas it ranges approximately from 0.7 to 1.7 in the off-axis discharge (from the interpretative modeling). This is consistent with results from gyrokinetic simulations, which predict an increase of the confinement properties if the magnetic shear decreases in the radial region where  $|s| < 1$  and a decrease of the confinement properties if the magnetic shear decreases in the radial region where  $s > 1 - 1.5$ .

In order to attempt identifying the region where the transport properties undergo the inversion, a shot-to-shot scan in the deposition location has been performed. The results arising from this experimental campaign have turned out to be of somewhat difficult interpretation, in all likelihood due to asymmetries in the EC heating system; though the general trend is confirmed. The origin of this misbalance was not easy to identify and could be due to various reasons, such as small tilts from the programmed launchers angles, or a different coupling between the pure heating phase and the current driving phase, or again to differences in the nominal gyrotron powers. The presented Swing ECCD discharges were, however, realized in pairs, differing only for a flip in the sign of

the toroidal injection angle of the two EC clusters: this scheme has allowed to disregard the systematic error due to the EC system misbalance, and therefore to obtain a limited database of Swing ECCD discharges in fairly good agreement with the predicted transport inversion.

# Chapter 5

## Modeling of ITER discharges with local EC Heating & Current Drive

### 5.1 Introduction

ITER is a joint international research and development project tokamak that aims “to demonstrate the scientific and technical feasibility of fusion power for peaceful purposes” [84]. This general aim can be broken down into a number of specific technical goals, all regarding performance, testing, design and operation requirements. Among its many goals, ITER should:

1. Achieve inductive plasma burn with a power amplification,  $Q$ , of at least 10, with  $Q = \frac{\text{fusion power}}{\text{auxiliary power}}$ , under stationary conditions on the time scales of plasma processes;
2. Aim at demonstrating steady state operation with  $Q \geq 5$ ;
3. Implement and test the key technologies and processes needed for future fusion power plants (including superconducting magnets, components able to withstand high heat loads, and remote handling);
4. Test and develop concepts for breeding tritium from lithium-containing materials inside thermally efficient high temperature blankets surrounding the plasma.

Compared with current conceptual designs for future fusion power plants, ITER will include most of the necessary technology, but will be of slightly smaller dimensions and will operate at about one-sixth of the power output level [85].



## 5.2 ITER external heating systems and main design parameters

External heating systems heat the plasma to a burning state and also control the safety factor profile. On ITER, several auxiliary heating and current drive systems are planned: negative ion-based neutral beams, with neutral beam energies of 1MeV, electron cyclotron heating at 170GHz with 1MW gyrotrons, ion cyclotron heating at 40-55MHz, and lower hybrid wave injection at 5GHz [86]. Each of these heating sources has technological and physics-based strengths and weaknesses. For instance, 1MeV sources of neutral beam are challenging to construct, but the coupling to the plasma is straightforward. Similar advantages and disadvantages are found for electron cyclotron heating, with an added benefit of a highly localized and controllable deposition profile. The role of ion cyclotron heating is primarily to heat the plasma to a burning condition, but it may also be used for current profile control in certain situations. However, the coupling in the presence large Edge Localized Modes is not guaranteed [87]. Lower hybrid current drive offers highly efficient current drive in the periphery of the plasma (where it is likely to be needed) with a more complicated coupling structure and less precise deposition control than, for instance, ECCD. The degree to which current profile control will be possible is ultimately limited by the constraints imposed by the physical processes of the particular auxiliary system.

The principal design parameters of the machine are reported in Table 5.1. In the following section, we provide a detailed description of the ITER Electron Cyclotron Heating and Current Drive system: the analysis of the capabilities of the EC system in controlling the sawtooth period and the current density profile constitutes the object of this work's final chapter.

## 5.3 Present ITER EC system

### 5.3.1 Description

The present ITER Electron Cyclotron Heating and Current Drive (ECH&CD) system consists of up to 24 gyrotrons operating at 170GHz and delivering from 1 to 2 MW each, for

Parameters	Symbol	Value
Major radius	$R_0$	6.2m
Minor radius	$a$	2.0m
Nominal aspect ratio	$A = R_0/a$	3.2
Volume	$V$	837m <sup>3</sup>
Cross sectional area	$S$	21.9m <sup>2</sup>
Nominal maximum plasma current	$I_p$	15MA
Maximum central magnetic field	$B_0$	5.3T
Edge plasma elongation	$\kappa_a$	1.86
Edge plasma triangularity	$\delta_a$	0.5
Nominal NBI power	$Q_{\text{NB}}$	33MW
Nominal EC power	$Q_{\text{EC}}$	20MW
Nominal IC power	$Q_{\text{IC}}$	20MW
Nominal LH power	$Q_{\text{LH}}$	34MW

Table 5.1: *Main ITER technical parameters from [84].*

a nominal injected power into the plasma of 20 MW. The system has two types of antennas to inject the power into the plasma: one Equatorial Launcher (Eq. Launch., or EL) which occupies one port in the equatorial plane, and four Upper Launchers (Up. Launch., or UL) occupying four ports in the upper plane.

At present, the Up. Launch. is designed uniquely for Neoclassical Tearing Mode (NTM) stabilization, achieved by off-axis co-ECCD [89]. NTMs have a very strong impact on the plasma confinement and are predicted to cause energy losses ranging from 30% to 50% of the total fusion power [90]. They are predicted to be triggered at the crash of long period stabilized sawteeth [91]. It is clear that for a performant operation, NTMs will have to be avoided in ITER, therefore the Up. Launch. must guarantee access to those (off-axis) surfaces susceptible to the onset of NTMs. The Eq. Launch. is designed to access the inner half (in  $\rho$ ) of the plasma, envisioning all physics applications other than NTM stabilization, including:

1. Current density profile tailoring for steady state operation;
2. Central heating to assist the transition from L- to H-mode and reach  $Q \geq 10$ ;

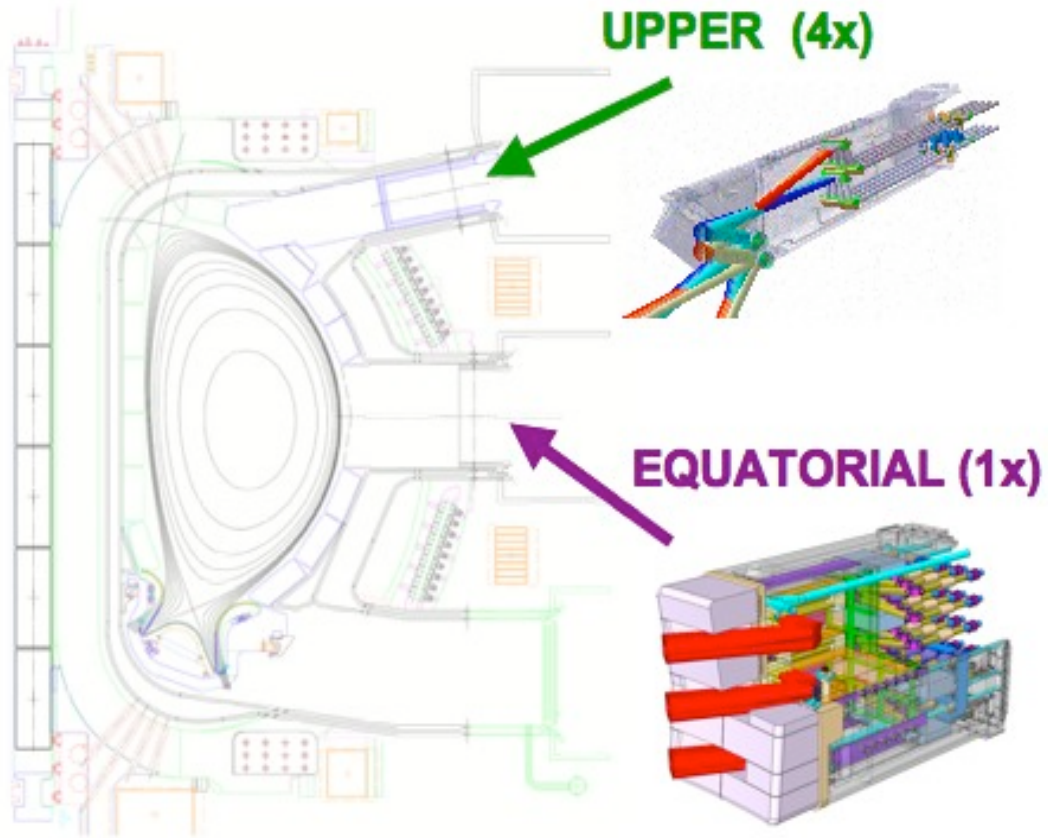


Figure 5.1: *The ITER EC H&CD system consists of up to 24 gyrotrons at 170GHz, delivering from 1 to 2 MW each and connected to one launcher situated in one equatorial port (Eq. Launch.) and to four launchers in the upper ports (Up. Launch.), for a nominal injected power into the plasma of 20 MW [88].*

### 3. Control of the sawtooth instability.

The Upper Launcher is shown in Fig. 5.1 and is capable of directing up to 8 beams (each up to 2MW) using two front steering mirrors per launcher (4 launchers) that scan the beam in a vertical plane. The two mirrors are indicated as Upper and Lower Steering Mirrors (USM and LSM) and each of them can sweep up to 4 beams nearly in a vertical plane during a discharge. In the original partitioning of the ITER EC system, the radial coverage permitted by the Up. Launch. poloidal steering range allowed access only to the radial region where NTMs are predicted to occur, namely around  $0.51 \leq \rho_T \leq 0.87$  (or  $0.64 \leq \rho_\Psi \leq 0.93$ ) for either the USM and the LSM (case of Scenario 2), where  $\rho_T$  and  $\rho_\Psi$  are, respectively, the square roots of the normalized toroidal and poloidal fluxes.

This range in the plasma includes the  $q = 3/2$  and  $q = 2$  surfaces for the main inductive and hybrid ITER scenarios (2 and 3) and also takes into account variations in  $\beta_N$  and  $l_i$ , to determine a realistic range in which the NTMs are expected to be found [92]. The Up. Launch. steering plane has a fixed toroidal injection angle,  $\beta \sim 20^\circ$ , optimized for a narrow and peaked current density profile needed for controlling NTM activity. The narrow deposition width of the beam allows enough margin to exceed the requirements for NTM stabilization. The figure of merit for NTM stabilization requires a ratio between  $j_{cd}$  and  $j_{bs}$  larger than 1.5, and the present Up. Launch. provides ratios ranging from 1.8 to 3.6, depending on the deposition location. The corresponding beam steering range to achieve this access is  $38^\circ \leq \alpha \leq 62^\circ$  for the LSM and  $44^\circ \leq \alpha \leq 64^\circ$  for the USM, where  $\alpha$  is the poloidal injection angle.

The Equatorial Launcher is also shown in Fig. 5.1 and is capable of directing 24 beams (1MW each) using three front steering mirrors that scan the beam in a toroidal plane (with the poloidal injection angle,  $\alpha$ , fixed). The three steering mirrors are indicated as top, mid and low, and each of them can sweep up to 8 beams each in a horizontal plane. The original ITER baseline requirements for the Eq. Launch. have more central deposition, approximately from  $0 \leq \rho_T \leq 0.49$  (or  $0 \leq \rho_\Psi \leq 0.65$ ), again for the case of Scenario 2. More specifically, the radii reached by the Eq. Launch. differ for each of the steering rows:  $0.23 \leq \rho_T \leq 0.44$  for the top row,  $0.03 \leq \rho_T \leq 0.49$  for the mid row and  $0.17 \leq \rho_T \leq 0.46$  for the low row. The toroidal scanning optimizes the amplitude of the driven current over the radial range described above and the corresponding beam steering range needed to achieve this access is  $20^\circ \leq \beta \leq 45^\circ$ , where  $\beta$  is the toroidal injection angle. The resulting access range of the EC launchers is shown in fig. 5.2 based on the initial design specifications.

Both launchers are presently specified for only co-ECCD, so that neither counter-ECCD nor pure EC heating are possible. It should be noted that the EC system will be ITER's main localized and steerable heating and current drive source, therefore it can be regarded more as a "surgical" tool rather than a bulk heating/current drive source, especially given its small total current driven (20MW  $I_{eccd}$  is always smaller than 7% of  $I_p$ ).

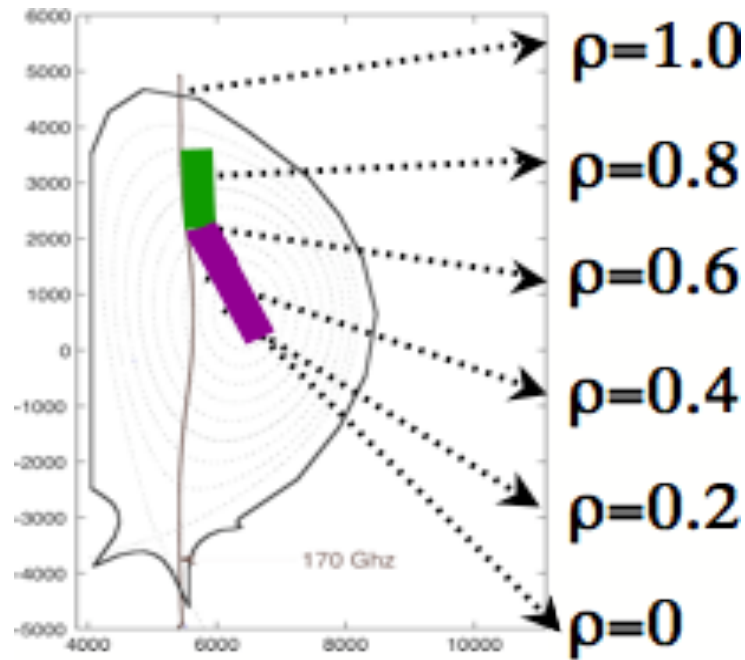


Figure 5.2: *Radial access range of the present partitioning of the ITER EC system: the Up. Launch. accesses the region  $\rho_\psi = 0.64 - 0.93$ , where NTMs are predicted to occur, while the Eq. Launch. has more central deposition from  $\rho_\psi = 0$  to  $0.61$ ,  $\rho_\psi$  indicating the square root of the normalized poloidal flux.*

### 5.3.2 Limitations

The present requirements for EC H&CD have been established in 1998-2000 by ITER: that period coincided with the early phase of multi-MW, multi-beam, steerable EC systems on tokamaks, therefore some of the more recent benefits of this heating source were less commonly known. There are several aspects that should be pointed out concerning the original scanning range and EC H&CD capabilities:

- A) The Up. Launch. (with 4 ports) is dedicated to the unique physics application of NTM control, while the Eq. Launch. (with a single port) is required to address all other physics applications. The partitioning between the physics programs covered by the two launchers is imbalanced.
- B) There is no possibility to provide pure heating or counter-current drive. This limits the potential usage of the Eq. Launch. when central heating is, for example, desired.

The present EC design will heat, but also drive central current, therefore peaking the current density profile, which is not desired in advanced and hybrid scenarios.

- C) The Eq. Launch. begins to have significant beam shine-through in the region of  $\rho_T > 0.45$ , which could damage other ITER systems and limit access to the  $q = 1$  surface.
- D) The geometrical scanning of the Eq. Launch. prevents access of the top and low rows inside approximately  $\rho_T < 0.2$ .

### 5.3.3 Revised variant

The limitations presented in the previous Section imply that redefining the present status of the launcher access might improve the EC potential for the control of MHD modes and the plasma current profile. A recently proposed variant [93], [88] to the above design redistributes the radial ranges covered by the two launchers, and therefore their physics programs, in a more balanced manner. Using the Up. Launch. for applications other than NTM control relaxes the constraints on the Eq. Launch. and opens the way to increase its functionality, for example allowing heating and counter-ECCD. This thesis covers a critical physics analysis of the gains/losses, with respect to the original design, that one could obtain if the EC system was modified as suggested in Ref. [93]. The main revisions proposed to improve the limitations listed in the four items enumerated above are the following.

#### A) Imbalanced partitioning

Given the high efficiency of the Up. Launch. for NTM stabilization [88], a broader physics scope can be delivered by the Up. Launch., for instance by assisting the Eq. Launch. in the control of the sawtooth instability. The Up. Launch. radial range is increased to access the  $q = 1$  flux surface (located, for instance, around  $\rho_T = 0.42$  for Scenario 2) and contribute to sawtooth control. In order to access the region from  $0.4 \leq \rho_T \leq 0.5$  with the EC power, the access range of the USM and LSM is spread out. This forms essentially three access zones from the Up. Launch.: an inner zone accessible with the USM (13MW, 16 beams), an overlap zone accessible with the USM and the LSM (therefore up to 20MW, 24 beams) and an outer zone accessible with just the LSM (13MW, 16 beams). Using this method,

the overall access region from the Up. Launch. is increased from about  $0.51 \leq \rho_T \leq 0.87$  to about  $0.3 \leq \rho_T \leq 0.86$ . The engineering advantages of this Up. Launch. configuration include a reduction of the overall opening in the front wall panel and of the rotation of each steering mirror, increasing their expected longevity by a factor of 2.

Note that, following a similar technique as above, the LSM mirrors of the four launchers can be spread out to access further toward the plasma edge, reaching up to 0.96. To ensure that there is some overlap with the USM, the suggested solution is to rotate two of the four LSM such that the deposition is further outward accessing the region about  $0.8 \leq \rho_T \leq 0.95$ , while the other two steering mirrors are kept with the access of  $0.6 \leq \rho_T \leq 0.86$ . This would then provide access of up to 6.7MW (assuming 1MW beams) out to  $\rho_T \leq 0.96$ . This would be useful in the event that the  $q = 2$  surface occurs further outward than expected or if higher rational surfaces such as the  $q = 5/2$  become susceptible to NTMs (this will not be treated in the present analysis). Note that this is only possible with the usage of four upper ports and eight additional switches to direct 8 beams to either the USM or LSM.

There are several advantages of this Up. Launch. configuration with respect to the original design configuration, which include:

- i) Access to the  $q = 1$  surface for control of the sawtooth oscillation.
- ii) Access further out in the event that the  $q = 2$  occurs beyond  $\rho_T = 0.86$ , or NTMs occur on other rational surfaces such as the  $q = 5/2$ .
- iii) The overlap region between the USM and LSM covers a majority of the reference scenario  $q = 2$  and  $q = 3/2$  locations, providing a large safety margin (between 1.8 and 3.6) for the NTM stabilization.
- iv) Local ECCD can be driven near the  $4/3$  surface and therefore a control of the  $4/3$  mode can be reached, either in order to obtain the Frequency Interrupted Regime (FIR) of NTMs [94] or in order to control the  $q$  profile evolution in hybrid scenarios, as with the  $3/2$  mode in DIII-D [95].
- v) Reduction of the overall opening in the front wall panel.
- vi) Reduction of the rotation of each steering mirror (from  $\pm 6.5^\circ$  to  $\pm 5.5^\circ$ ) increasing the expected longevity by a factor of 2.

## B) Pure ECH/counter-ECCD

Some key issues arise since with the present design it is not possible to do pure heating, nor counter-ECCD. Injecting only a co-ECCD component can have detrimental effects on the final profiles; for example it can remove the reverse shear in advanced scenarios or anticipate the first sawtooth crash to occur earlier in hybrid scenarios. Therefore, if central heating by EC waves is needed to assist L-H transition during the ramp-up phase, the present launcher design might prohibit the final target  $q$  profile from being reached. The Eq. Launch. would thus have limited usage for reverse shear and hybrid scenarios. In addition, in most high performance discharges in present tokamaks, central electron heating is used to control impurity accumulation in the center and density peaking, either with ICRH at JET [96], or with ECH at AUG [97]. Therefore central heating might be needed for impurity control and density peaking control, either before  $\alpha$ -heating takes over, or if the latter is not sufficient.

Performing sawtooth control by the Up. Launch. would allow the requirements for the Eq. Launch. to be relaxed. For instance, counter-ECCD could be considered, in order to allow current density profile tailoring and reverse shear scenarios. In order to provide counter-ECCD with the Eq. Launch., one of the three steering mirror assemblies can be entirely flipped (as indicated in Fig. 5.3, for the case of the top row), which would result in driving negative current with 6.7MW of EC power. This would be useful for either balancing the co-ECCD (providing pure ECH, with no net driven current and without peaking the plasma current density profile) or for current profile tailoring (increasing the current hole in the centre and controlling  $q_0$  and  $q_{\min}$  in reverse shear profiles). In general, counter-ECCD offers greater flexibility and control of the plasma current density profile. In addition, it provides the possibility to decouple the heating and current driven effects which might be very useful in the optimization towards DEMO (DEMONstration Power Plant, a proposed nuclear fusion power plant [98]).

## C) Beam shine-through

The present toroidal steering range of the Eq. Launch. is  $20^\circ \leq \beta \leq 45^\circ$ , however such a steering range is not only unnecessary and increases the engineering constraints, but also risks damaging other systems due to beam shine-through. The minimum values in  $\rho_T$  accessed by the top, mid and low steering rows are achieved when  $\beta = 23^\circ$ . Thus the



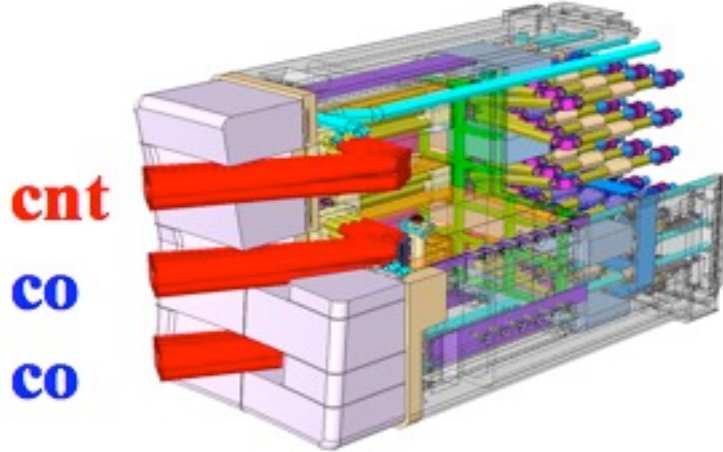


Figure 5.3: *The top steering mirror assembly of the Eq. Launch. can be flipped in order to provide counter-ECCD (6.7MW).*

steering range between  $20^\circ \leq \beta < 23^\circ$  does not provide any increased access. Moreover, full absorption of the Eq. Launch. beams occurs for toroidal steering angles of  $\beta \leq 40^\circ$ . At larger angles, part of the beam passing through the plasma is not fully absorbed. In such a case, the beam could significantly damage either another heating system, diagnostic or a Blanket Shielding Module (BSM). The percentage of the absorbed power decreases significantly with a larger toroidal steering angle. Therefore, a hard limit should be imposed to ensure that the beam is fully absorbed for all plasma scenarios and a reasonable range of temperature and density profiles. Thus, in the course of this work, a toroidal steering range of  $23^\circ \leq \beta \leq 38^\circ$  has been used for each Eq. Launch. beam set. This reduces the access radius from  $\rho_T \lesssim 0.49$  to  $\rho_T \lesssim 0.41$ .

Note that this would reduce the required opening in the BSM. A smaller opening would in turn reduce the thermal and neutron flux seen by the steering mechanism, mirrors and other RF components, which are critical issues for the Eq. Launch. since its position in the equatorial plane is in full view of the plasma core.

#### D) Central access

The present orientation of the three Eq. Launch. steering rows in the horizontal plane results in a geometrical limit that prevents the top and low steering rows to access the plasma centre. The minimum  $\rho_T$  location with the mid row is  $\rho_T = 0$ , whereas for the

other rows, the minimum  $\rho_T$  locations accessed are approximately  $\rho_T = 0.23$  for the top row and  $\rho_T = 0.17$  for the low row, for Scenario 2. Introducing a small poloidal tilt angle, such that the top row aims slightly downward and the bottom row aims slightly upward, would provide access closer to the plasma centre from the two external rows and utilize more efficiently the full steering range from  $23^\circ \leq \beta \leq 38^\circ$  of each row. Note that it would not be necessary for all the three steering rows to access the plasma centre. Depositing all 20MW on axis could render the plasma unstable due to a strong peaking of the plasma current density profile, because the resulting EC power and EC current density would be very high. Also, some spread is desired so that, should the plasma axis move up or down, the centre would still be accessed by at least one of the steering rows. A tilt of  $\pm 5^\circ$  would be achievable in the present Eq. Launch. design without requiring modification to the BSM design. In addition, there would still be adequate spread of the three deposition locations to ensure access to the plasma centre of about  $\pm 25\text{cm}$ . A tilt greater than  $\pm 5^\circ$  would require modifications of the BSM design without much further gain for the EC system. This is why a tilt of  $\pm 5^\circ$  is proposed.

This global revision would allow the EC system to have access from the plasma axis out to  $\rho_T \leq 0.96$ , covering essentially the entire plasma cross section without impacting an increase of costs and actually increasing the mechanical reliability and overall machine safety. Comparison of the discussed access ranges and of the various physics applications are shown in Table 5.2 and in Table 5.3. Figs. 5.4–5.8 show the various  $j_{\text{eccd}}$  and  $P_{\text{EC}}$  profiles obtained at different deposition locations with the revised EC system. These are obtained using formulas, described in Appx. B, obtained by fitting the GRAY results [88], [99].

## 5.4 ITER operation scenarios

The ITER base-line design foresees a number of operation scenarios obtained with various combinations of heating schemes and plasma parameters, consequently leading to different plasma burn regimes. In the course of this work, the physics analysis has been based on three selected full magnetic field, H-mode, scenarios at the end of burn, referred to as the base-line inductive, hybrid and steady state scenarios. These are briefly reviewed in the

		Upper Launcher		Equatorial Launcher		
		USM	LSM	TOP	MID	LOW
PRESENT SYSTEM	$\alpha$	44° – 64°	38° – 62°	0	0	0
	$\beta$	23°	23°	20° – 45°	20° – 45°	20° – 45°
	$\rho_T$	0.51 – 0.87	0.51 – 0.87	0.23 – 0.44	0.03 – 0.49	0.17 – 0.46
	$\rho_\psi$	0.64 – 0.93	0.64 – 0.93	0.29 – 0.55	0.04 – 0.61	0.22 – 0.58
REVISED SYSTEM	$\alpha$	44° – 68°	34° – 58°	+5°	0	–5°
	$\beta$	20°	18°	23° – 38°	23° – 38°	23° – 38°
	$\rho_T$	0.3 – 0.8	0.55 – 0.96	0.12 – 0.4	0.001 – 0.41	0.08 – 0.4
	$\rho_\psi$	0.38 – 0.9	0.68 – 0.98	0.15 – 0.5	0.001 – 0.52	0.01 – 0.5

Table 5.2: Comparison of the present and revised access radii of the ITER EC systems (case of Scenario 2). All steering ranges are subject to change in the future.

		Foreseen applications	Co-ECCD	Pure ECH	Counter-ECCD
PRESENT SYSTEM	<b>Upper Launcher</b>	NTM control	yes	no	no
	<b>Equatorial Launcher</b>	ST control, core heating for L-H transition	limited	no	no
REVISED SYSTEM	<b>Upper Launcher</b>	NTM and ST control	yes	no	no
	<b>Equatorial Launcher</b>	$j_p$ tailoring, $q_0/q_{\min}$ control, RS and hybrid scenarios	yes	yes	yes

Table 5.3: Comparison of the present and revised physics applications of the ITER EC systems.

following subsections. For a more detailed description on the ITER operation scenarios, see [84]. The analyzed plasmas have considerably different  $q$ ,  $T$ ,  $n$ ,  $j_{bs}$ ,  $P_{add}$  and  $Q$ . These scenarios were correctly reproduced by the transport model described in Appx. A, and table 5.4 contains a list of the relevant physical quantities simulated by ASTRA.

The reference confinement regime for inductive  $Q = 10$  operation is the thermal energy

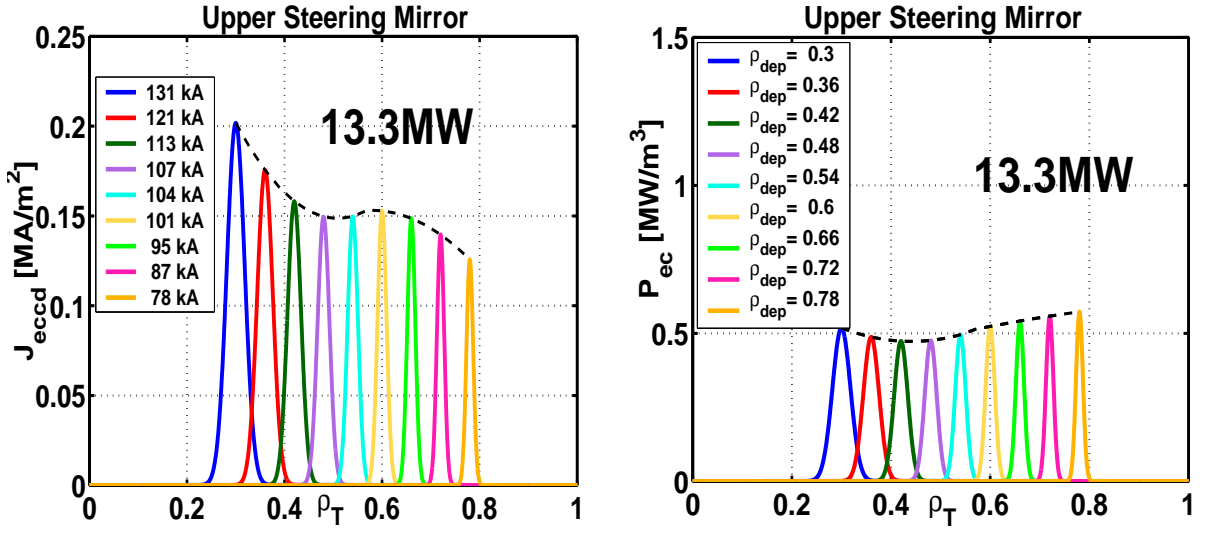


Figure 5.4: a) GRAY-calculated EC current density and b) power profiles as a function of the deposition location for the upper steering mirror of the Up. Launch. Case of Scenario 2.

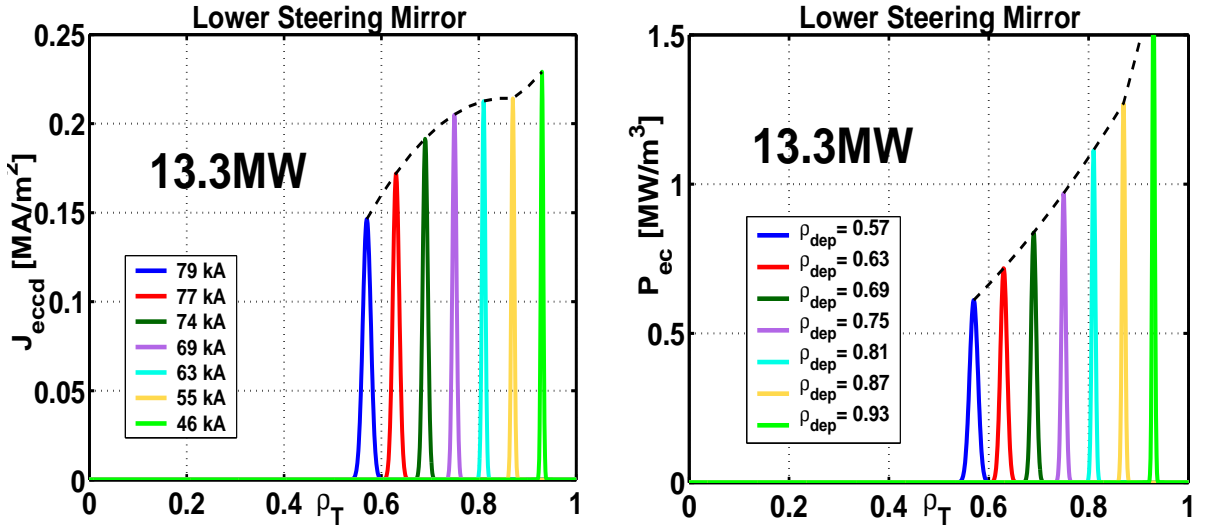


Figure 5.5: a) GRAY-calculated EC current density and b) power profiles as a function of the deposition location for the lower steering mirror of the Up. Launch. Case of Scenario 2.

confinement time, described by the ITER-H98(y,2) [100] empirical scaling as:

$$\tau_{\text{E,th}}^{\text{H98}(y,2)} = 0.0562 HH_{(y2,98)} I_p^{0.93} B^{0.15} R^{1.39} n_{19}^{0.41} a^{0.58} \kappa_a^{0.78} M^{0.19} P_{\text{input}}^{-0.69}, \quad (5.1)$$

where  $M = 2.5$  is the average atomic mass number of the main plasma ion species and

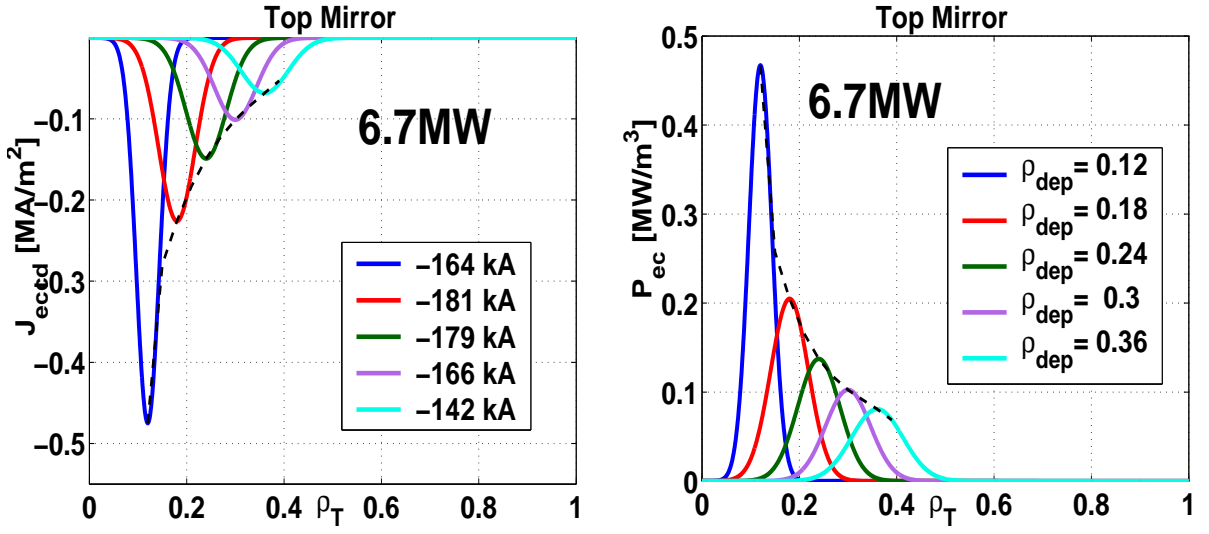


Figure 5.6: a) *GRAY*-calculated EC current density and b) power profiles as a function of the deposition location for the top mirror of the Eq. Launch. Case of Scenario 2.

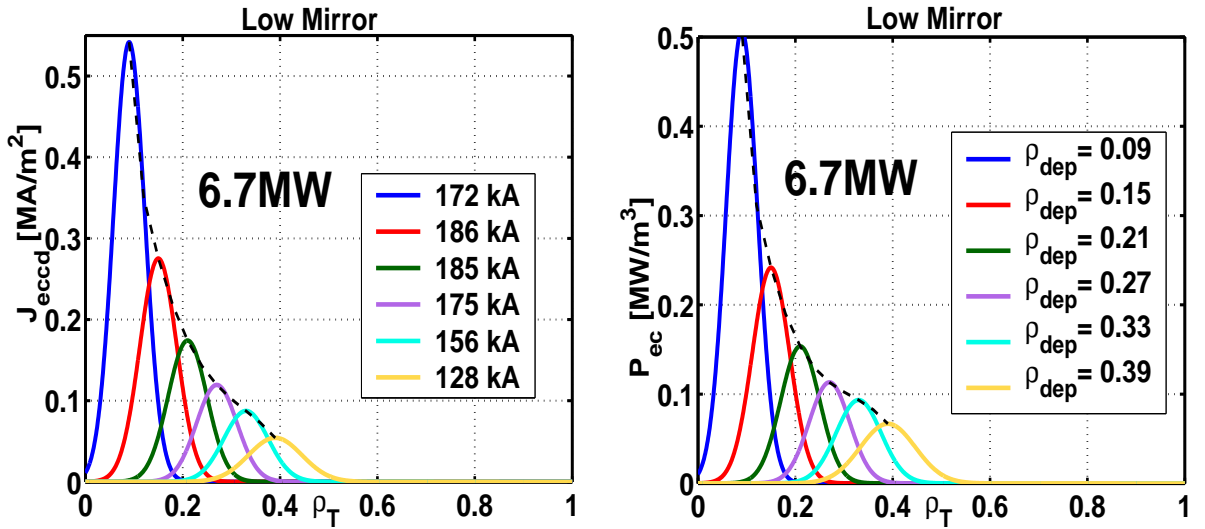


Figure 5.7: a) *GRAY*-calculated EC current density and b) power profiles as a function of the deposition location for the low mirror of the Eq. Launch. Case of Scenario 2.

the relevant quantities are expressed in the following units:  $\tau_E$  [s],  $I$  [MA],  $B$  [T],  $R$  [m],  $n$  [ $10^{19}\text{m}^{-3}$ ],  $a$  [m],  $P_{\text{input}}$  [MW]. The  $HH_{(y2,98)}$  factor is the thermal confinement improvement, which is close to unity, and depends on the scenario considered. In the course of this work, the scaling presented above has been used to normalize the electron heat diffusion coefficient, with  $HH_{(y2,98)} = 1$  for the standard Scenario 2, and  $HH_{(y2,98)} \sim 1.3$  for the advanced fully non-inductive Scenario 4 [101]. It should be noted that new scalings

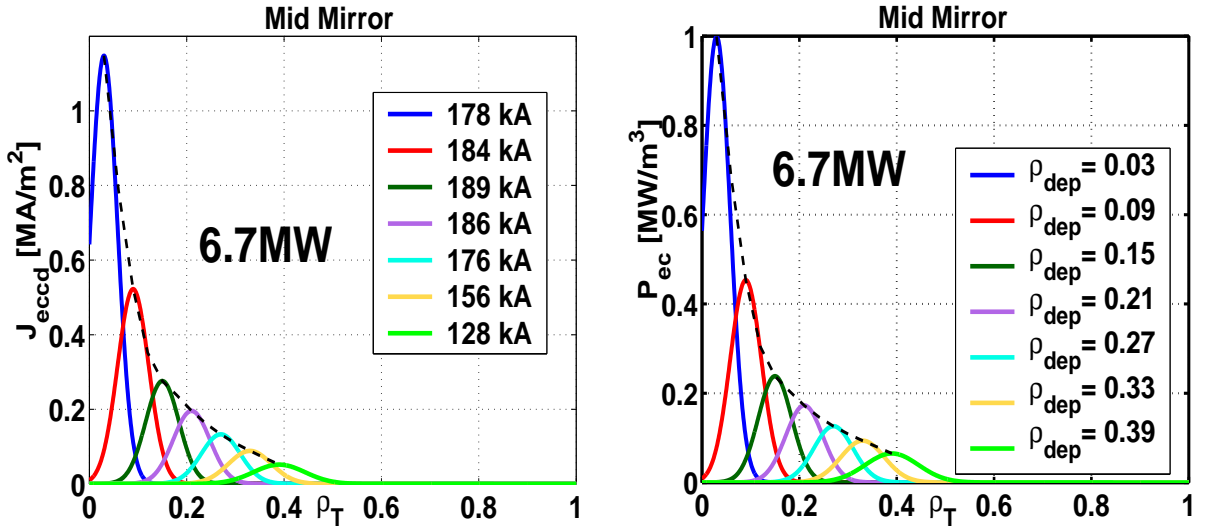


Figure 5.8: a) *GRAY*-calculated EC current density and b) power profiles as a function of the deposition location for the mid mirror of the Eq. Launch. Case of Scenario 2.

based on an extended database and advanced analysis techniques [102] have predicted operational spaces for the ITER reference scenario with improved performance relative to scaling ITER-H98(y,2), therefore the analysis presented here is more conservative. A brief overview of the ITER model used is presented in Sec. 5.5, whereas a more exhaustive description can be found in Appx. A.

#### 5.4.1 Inductive operation (Scenario 2)

The inductive ITER operation, Scenario 2 in the ITER nomenclature, is a standard H-mode discharge, with a peaked current density profile and a monotonic safety factor profile. The  $q = 1$  surface is found around  $\rho_T = 0.4$  ( $\rho_\psi \sim 0.5$ ), therefore the sawtooth instability is expected to occur in this scenario. In ITER, the sawtooth period,  $\tau_{\text{ST}}$ , is predicted to be very long, due to fusion-originated  $\alpha$ -particles, which should provide a significant stabilizing effect on the sawteeth [103]. This scenario will operate at  $I_p = 15\text{MA}$  ( $q_{95} \sim 3, q_0 \sim 0.9$ ). The inductive current component will be a large fraction of the total current, namely more than 70%. The additional heating will start at the beginning of the current flat-top and will consist of 33MW of auxiliary power (NBI), resulting in a fusion multiplication factor of  $Q=10$  for about 400s. Fig. 5.9 shows the simulated current density components and safety factor profiles (a) as well as the pressure profiles (b) for

an intermediate time during the sawtooth period.

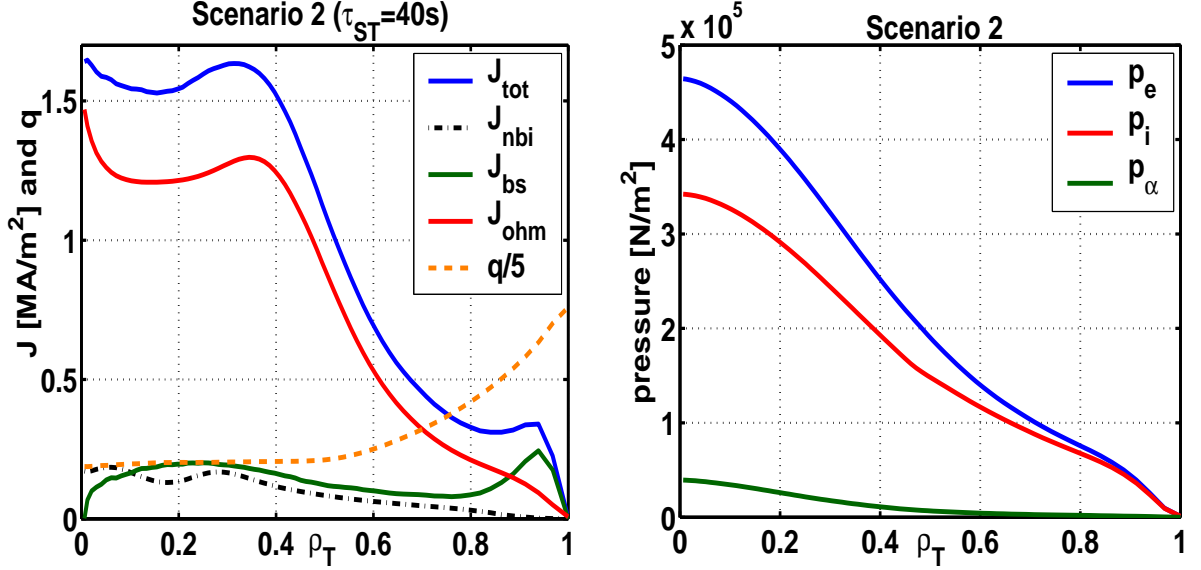


Figure 5.9: a) ASTRA-simulated current density components and safety factor profiles and b) pressure profiles for an intermediate time during the sawtooth period for Scenario 2.

This standard ITER scenario with an edge transport barrier has an extensive experimental database [104] and is attractive for reaching high fusion power. However, it does not allow to reach conditions where the plasma current is completely non-inductively driven, while still achieving a significant  $Q$ .

### 5.4.2 Hybrid operation (Scenario 3)

ITER's hybrid scenario, also referred to as Scenario 3, is a long-pulse, inductively driven plasma burn that has been extended by current drive systems, but which is not fully steady state. The aim is to obtain a large neutron fluence, in particular to test the blanket modules [105]. In this case, about 50% of the total  $I_p$  is sustained by the ohmic current component, therefore a substantial fraction of the plasma current is obtained by non-inductive means, including the bootstrap current.

Similarly to the inductive case, the hybrid scenario has a  $q = 1$  surface, located at around  $\rho_T = 0.3$ , with a rather flat  $q$  profile ( $q_0 \sim 1$  and  $q_{95} \sim 4$ ). Scenario 3 is planned to operate at  $I_p = 13\text{MA}$ , with 33MW of NBI power resulting in  $Q = 10$ . Note that this scenario has not been taken into account in the following ASTRA calculations regarding the effect of

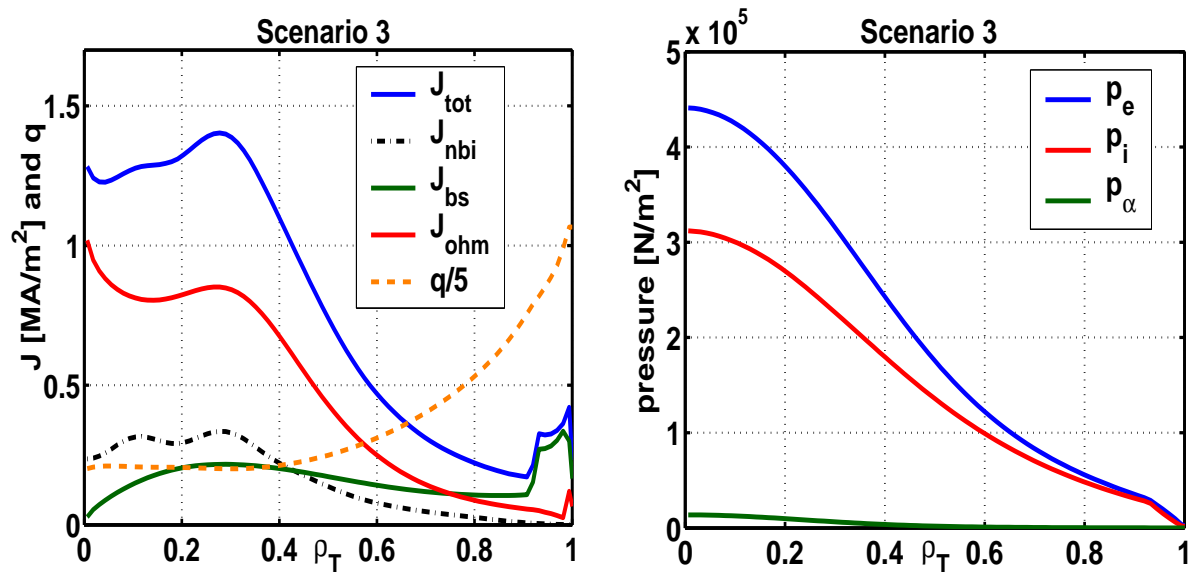


Figure 5.10: a) Current density components and safety factor profiles and b) pressure profiles for Scenario 3 as from Ref.[106].

ECCD on the sawtooth period and current density tailoring, but it has been mentioned in this context for the sake of completeness. Moreover, equilibrium calculations of this Scenario have been carried out with the CHEASE code and will be briefly commented upon in Sec. 5.7.3. In Fig. 5.10 we report the current density components, safety factor and pressure profiles of Scenario 3 as given in [106].

### 5.4.3 Steady-state operation (Scenario 4-type I and II)

The ITER target steady state scenario is a plasma burn with weakly negative magnetic shear in which all the plasma current is sustained by fully non-inductive means. The fraction of bootstrap current is around 50% of the total plasma current. This steady state scenario will produce about 300MW of fusion power with  $Q \gtrsim 5$  for about 3000s. The fully non-inductively sustained plasma current will be about  $I_p = 9\text{MA}$  ( $q_{95} \sim 5.5$ ). To form a weak reverse magnetic shear, the plasma current will be ramped up faster than in the other Scenarios, and the additional heating will start during the current ramp-up phase. The goal of this scenario is ultimately to reach pure steady state, and in other tokamaks much effort is being made in order to extrapolate the presently developed non-inductive current drive regimes to ITER [107].

In Ref. [86], two steady state scenarios have been taken into account, referred to as



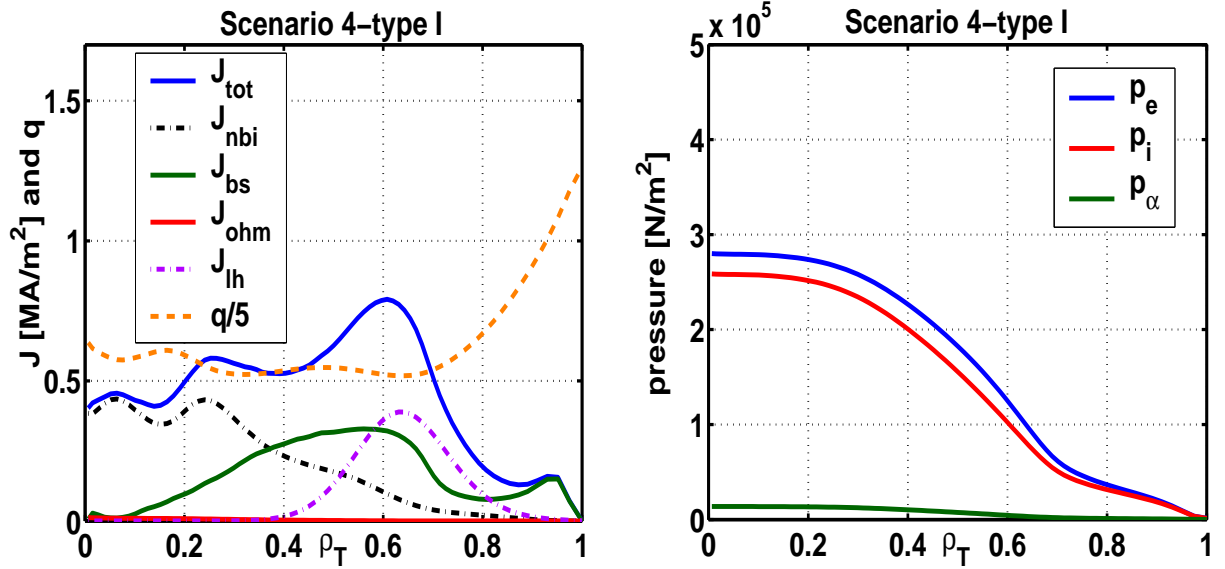


Figure 5.11: *a) Simulated current density components and safety factor profiles and b) pressure profiles for Scenario 4-type I.*

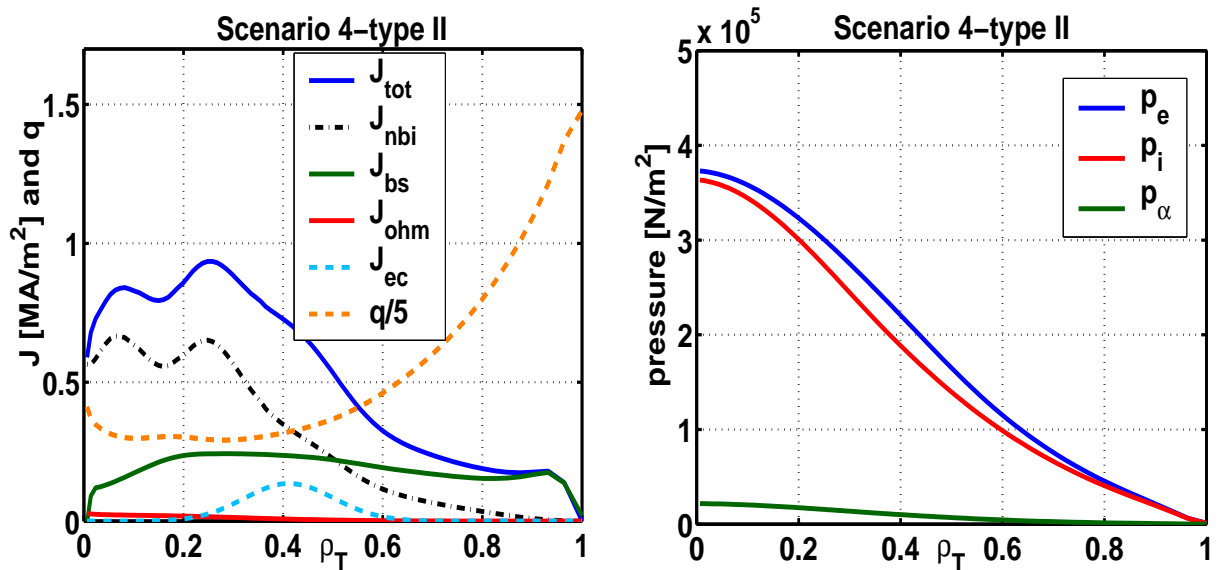


Figure 5.12: *a) Simulated current density components and safety factor profiles and b) pressure profiles for Scenario 4-type II.*

Scenario 4-type I and type II. Scenario 4-type I is sustained by 33MW of NBI power on-axis and by 34MW off-axis LH power, whereas for Scenario 4-type II it is assumed that a third NBI beam is available on ITER, resulting in about 50MW of on-axis NBI power, the remaining 20MW being provided by the EC system. The differences in current density,

safety factor and pressure profiles for the steady state scenarios are shown in Figs. 5.11 and 5.12.

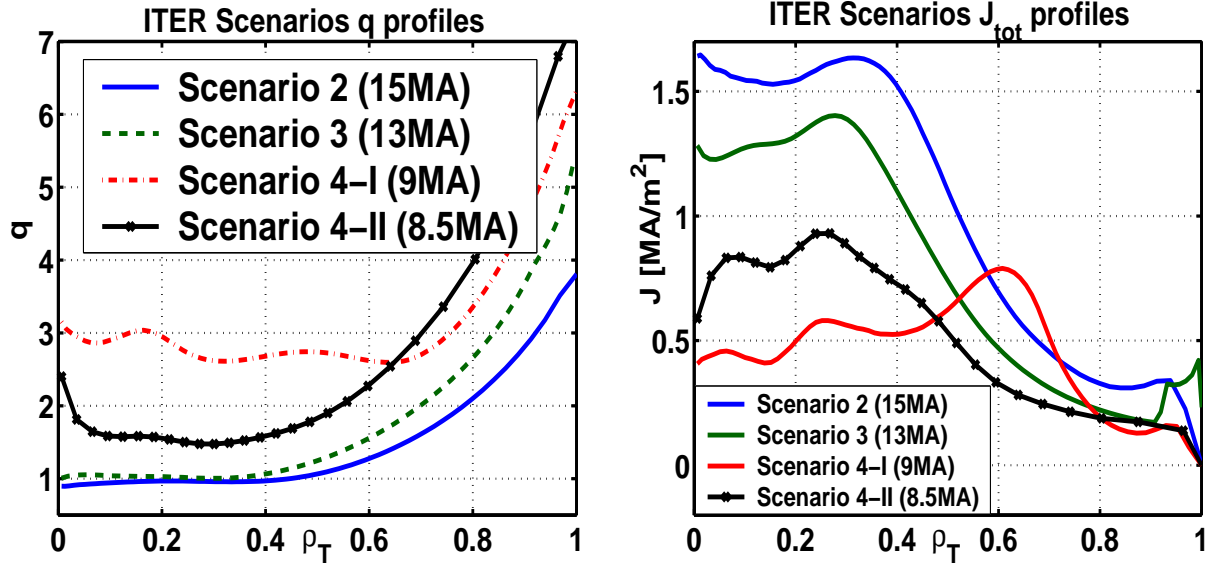


Figure 5.13: Comparison of a) the safety factor and b) total current density profiles for the three ITER Scenarios used in the analysis.

Finally, a comparison of the  $q$  and  $j$  profiles of the various ITER Scenarios is shown in Fig. 5.13, whereas a table comparing the main physical quantities used in the following analysis, either simulated or fixed, is presented in Table 5.4.

## 5.5 Model for ITER discharges

The modeling concerning the effects of local ECH&CD on the safety factor profile was carried out both with the CHEASE equilibrium code [43] and with the ASTRA transport code [18], to compare the different steady state and transient effects on the magnetic shear in the inductive scenario and on the profile control in the reverse magnetic shear scenario. In either case, the EC profiles have been calculated by the beam tracing code GRAY [108], which provides the total ECCD current,  $I_{eccd}$ , the peak value,  $j_{eccd}^{peak}$ , the location,  $\rho_{eccd}$ , and the width,  $w_{eccd}$ , of the gaussian EC current density profile, as well as the peak value,  $P_{ech}^{peak}$ , the location,  $\rho_{ech}$ , and the width,  $w_{ech}$ , of the gaussian EC power density profile [88], see Appx. B.

Being an equilibrium code, CHEASE does not take into account the transport effects

Parameters	Symbol	Sc2	Sc3	Sc4-I	Sc4-II
Plasma current [MA]	<b><math>I_p</math></b>	15	<i>13</i>	9	8.5
Loop voltage [mV]	$V_{loop}$	86.7	<i>40</i>	0	0
Discharge duration [s]		400	<i>~2000</i>	3000	3000
Energy confinement time	$\tau_E$	3.7s	<i>3.4</i>	2.2	2.2
Volume-averaged electron density [ $10^{19}m^{-3}$ ]	$\langle n_{e19} \rangle$	10	<i>7.9</i>	6.6	7
Central electron temperature [keV]	<b><math>T_{e0}</math></b>	24.8	<i>31.8</i>	24.0	29.1
Central ion temperature [keV]	<b><math>T_{i0}</math></b>	21.2	<i>27.5</i>	25.3	32.7
Central electron density [ $10^{19}m^{-3}$ ]	$n_{e0}^{19}$	11.4	<i>10.2</i>	7.3	8.0
Inductive current fraction [%]	<b><math>I_{ohm}\%</math></b>	73	<i>53</i>	0	0
Bootstrap current fraction [%]	<b><math>I_{bs}\%</math></b>	18	<i>29</i>	43	48
Driven current fraction [%]	<b><math>I_{cd}\%</math></b>	9	<i>18</i>	57	52
Safety-factor on magnetic axis	<b><math>q_0</math></b>	0.9	<i>1</i>	3.2	2.1
Minimum safety-factor	<b><math>q_{min}</math></b>			2.6	1.5
Safety-factor at the flux surface enclosing 95% of the poloidal flux	<b><math>q_{95}</math></b>	3.1	<i>4.0</i>	5.5	6.1
Effective charge	$Z_{eff}$	1.67	<i>1.67</i>	1.67	1.67
$\alpha$ -particle power [MW]	<b><math>Q_\alpha</math></b>	80	<i>78</i>	67	71
Fusion power [MW]	<b><math>Q_{DT}</math></b>	400	<i>390</i>	334	357
Auxiliary (external) power [MW]	$Q_{aux}$	33	<i>33</i>	67	50
Power amplification	<b><math>Q</math></b>	12	<i>12</i>	5	7
Thermal confinement improvement	<i>HH</i>	1	<i>1.2</i>	1.37	1.37

Table 5.4: Comparison of some relevant quantities employed or self-consistently calculated in the following ASTRA simulations, for the different ITER Scenarios. Note that the quantities reported in the column in *Italic* (Scenario 3) are the values from Ref. [106], since transport modeling has only been performed for Scenarios 2, 4-type I and 4-type II. The symbols of the physical quantities calculated by ASTRA are indicated in **Bold**.

due to the additional heating power, but only the effects due to the modification of  $j$ , which in this case is due to the ECCD (with frozen temperature and density profiles). As previously mentioned in Chap. 2, the input to CHEASE is constituted by the plasma boundary and by the equilibrium profiles: the pressure profile is kept fixed, whereas the

current density profile is given by the contribution of the equilibrium current density without ECCD and by the modeled  $j_{\text{eccd}}$ .

Concerning the ASTRA transport modeling of ITER discharges, a DT plasma with Be and Ar impurities has been taken, with a transport model that reproduces the main ITER Reference Scenarios without ECCD/ECH.

Specifically, a reduced set of 1D equations for the time evolution of the electron and ion temperatures, the  $\alpha$ -particles density and the poloidal magnetic flux is solved. The equilibrium is self-consistently calculated with the ASTRA 2D fixed-boundary solver. The electron density is kept fixed and the impurity densities are assumed to be known fractions of it:  $n_{\text{Be}} = 2\% n_e$  and  $n_{\text{Ar}} = 0.12\% n_e$ . The deuterium and tritium densities are determined from quasi-neutrality assuming they are equal, and the effective charge profile is assumed uniform ( $Z_{\text{eff}} = 1.67$ ).

The electron and ion heat diffusion coefficients are normalized to achieve a thermal confinement improvement  $HH_{(y2,98)} \sim 1$ , for the standard Scenario 2, and  $HH_{(y2,98)} \sim 1.37$  for the advanced fully non-inductive Scenario 4 [101]. The  $\alpha$ -particles diffusion coefficient is equal to the electron diffusion coefficient which one would need in order to obtain the  $n_e$  profile, consistently calculated from the various sources and sinks.

Various thermal sources and losses are taken into account: firstly, some terms common to both the ion and electron species, such as auxiliary heating sources (NBI injection and DT reactions) and electron-ion heat exchange due to Coulomb collisions; secondly, for ions only, a cold neutrals ionization source and charge exchange losses; thirdly, for electrons further auxiliary (LH and ECRH) and Ohmic heating sources, and radiation losses (including the electron Bremsstrahlung and synchrotron radiation, and the impurities line radiation losses).

The neoclassical conductivity and the bootstrap coefficients are evaluated by the formulas obtained by solving the Fokker-Planck equation with the full collision operator [44], [45]. Concerning the auxiliary H&CD sources, the Neutral Beam (NB) components are self-consistently evaluated with a simplified Fokker-Planck subroutine which calculates the separate NB contributions to the electrons and ions. The Lower Hybrid components are fixed gaussian profiles. EC power density and current driven profiles are evaluated by the beam tracing GRAY code [108], assuming the steering ranges proposed by the variant design, and allowing for counter-ECCD driven by the top row of the Eq. Launch.

A sawtooth module based on the Porcelli model [103], [109] is used, which accounts for the  $\alpha$ -particles stabilization. The free parameter of the model,  $c_\rho$ , is chosen to provide a reference sawtooth period,  $\tau_{\text{ST}}=40\text{s}$ , when no EC heating is applied ( $c_\rho = 4.3$ ).

A more detailed description of the transport model, including the equations solved and the various sources and sinks, can be found in Appx. A.

## 5.6 Control of the sawtooth instability

Sawteeth are periodic relaxations of the central pressure profile, playing an important role in the determination of both plasma performance and plasma profiles [23]. Their name is due to the temporal evolution of the central plasma pressure, resembling a sawtooth, as observed by soft X-rays. Sawteeth cause an expulsion of particles and energy out of the  $q = 1$  surface, attributed to a reconnection of the magnetic field lines in this region. During a sawtooth crash, the particles, energy and current in the centre are redistributed resulting in almost completely flat profiles, mainly in the region inside the  $q = 1$  surface. Because of this uniform flattening of the profiles and the associated fast radial transport, sawteeth decrease the average energy confinement time. The larger the  $q = 1$  radius and the frequency of sawtooth crashes, the higher the impact of sawteeth on the energy confinement time.

On one hand, sawtooth stabilization produces centrally peaked temperature profiles and therefore is favorable for increasing the fusion yield. On the other hand, it has been shown that long sawtooth periods can have undesirable consequences, such as the creation of seed magnetic islands capable of triggering pressure limiting neoclassical tearing modes [91]. While long-period sawteeth can induce other instabilities like NTMs or, in the worst case, plasma disruption, modest sawtooth oscillations are helpful in a burning plasma to expel the helium ash created by the burn process in the centre of the plasma.

Sawtooth period ( $\tau_{\text{ST}}$ ) control can be achieved with the help of non-inductive current drive, and has been demonstrated with ECCD injection on several machines, such as TCV [110] and AUG [111]. The control is realized by modifying the magnetic shear profile near the  $q = 1$  surface,  $s_1$ . Since the stabilizing effect of the fast particles scales inversely with the values of  $s_1$  [103], a similar control can be obtained in ITER. The control can be done by depositing localized co- or counter-ECCD around the  $q = 1$  surface. Particularly, it

was shown that it is possible to destabilize sawtooth, i.e. to shorten the sawtooth period, by depositing either localised co-ECCD inside or counter-ECCD just outside the  $q = 1$  surface, to increase the value of the magnetic shear at the  $q = 1$  surface [110]. Similarly,  $\tau_{\text{ST}}$  increases if co-ECCD is driven just outside  $q = 1$  ( $s_1(t)$  slows down).

Because of the importance of this instability in future burning plasmas, methods for active control of the current density profile in the plasma are required. The optimized Up. and Eq. Launchers in ITER can drive co-ECCD at different radial locations inside the plasma and are therefore suitable for this purpose. Thus, it is important for ITER to identify the effects of localized heating and current drive by EC waves on the stabilization/destabilization of sawteeth.

### 5.6.1 Self-consistent transport results

The simulations presented in this section have been realized with the ASTRA code coupled to the Porcelli model [103], [109], as described in Appx. A. In these simulations, we show the effect of EC H&CD on the sawtooth period during various scans in the deposition location of ECCD for ITER inductive Scenario 2. The sawtooth period in ITER is predicted to be considerable, thanks to the beneficial influence of  $\alpha$ -particle stabilization:  $\tau_{\text{ST}} \sim 10 - 200\text{s}$ . Since the sawtooth period is related to the free parameter of the model,  $c_\rho$ , the latter has been chosen to provide  $\tau_{\text{ST}} = 40\text{s}$  for the reference case, without any additional EC power. The corresponding value for  $c_\rho$  is 4.3. With a free parameter set to 1 (as originally in the model), the sawtooth period without ECCD becomes larger than 100s. The results obtained with 13.3MW of co-ECCD driven from the USM are shown in Fig. 5.14. The plot shows the time evolution of the  $s_1$  value in case of no EC injection (top plot), co-ECCD deposited just inside  $q = 1$  (middle plot) and just outside  $q = 1$  (bottom plot). The sawtooth period can be easily estimated from this plot as  $\tau_{\text{ST}} = 40\text{s}$  (top plot),  $\tau_{\text{ST}} = 30\text{s}$  (middle plot) and  $\tau_{\text{ST}} = 70\text{s}$  (bottom plot), showing that the USM is particularly efficient in delaying the occurrence of sawtooth crashes, and can also increase the sawtooth frequency.

In Fig. 5.15, the value of the sawtooth period is shown as a function of the scan in the radial deposition location,  $\rho_{\text{dep}}$ , of the injected co-ECCD. The different markers correspond to different mixtures of EC power from the Eq. Launch. or the USM. In general, the variation of the sawtooth period during the ECCD location scan is consistent to the results shown

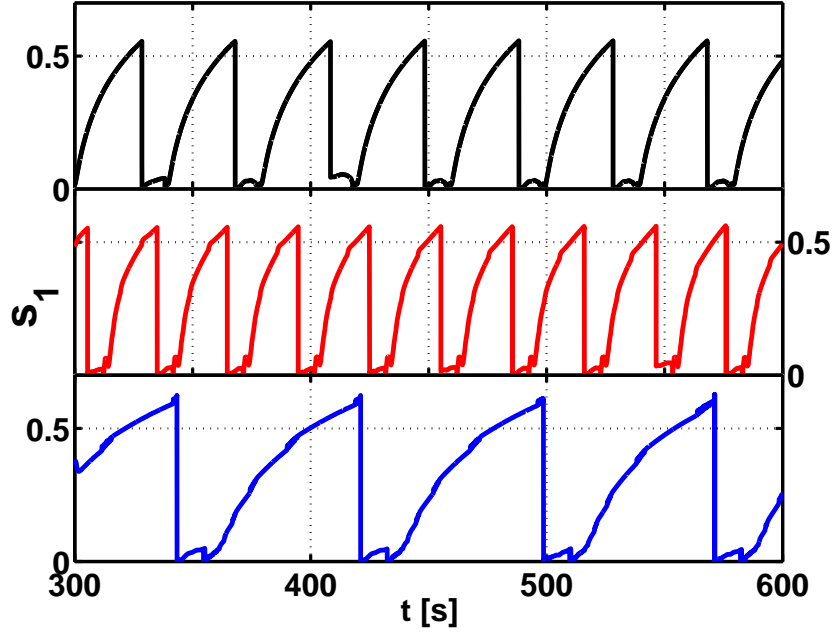


Figure 5.14: *Time evolution of the value of the magnetic shear at  $q = 1$ , for the reference case without ECCD (top plot), with ECCD driven from the USM inside  $q = 1$  (middle plot) and outside  $q = 1$  (bottom plot). The middle and bottom cases were modeled with a real time control on the value of the EC deposition radius:  $\rho_{\text{dep}} = \rho_1 + \eta w_{\text{CD}}$ , with  $\eta = -0.75$  (middle plot) and  $\eta = 0.25$  (bottom plot).*

in Ref. [110]. The dashed black line indicates the reference Scenario 2 sawtooth period of 40s, when no EC waves are applied. With the present design, i.e. with the Eq. Launch. driving 20MW of co-ECCD, it is possible to achieve the largest reduction of the sawtooth period, namely passing from 40s to 23-24s, at  $\rho_T \sim 0.3$  (blue dots in Fig. 5.15). However, a combination of co-ECCD driven by 2 rows of the Eq. Launch. (13.3MW) and the remaining power driven by the USM of the Up. Launch., at a fixed location, can also decrease the sawtooth period down to less than 30s, as indicated by the green starred markers. The fixed location for USM injection was varied between  $\rho_T = 0.3$  and  $\rho_T = 0.35$ , with no significant difference. The poor control in both destabilizing and stabilizing the sawteeth by using only the Up. Launch. (red diamonds, 13.3MW) can be ameliorated with a real-time control (RTC) algorithm (cyan empty dots), through which the deposition location is recalculated every time step by the simple formula:  $\rho_{\text{dep}} = \rho_1 + \eta w_{\text{CD}}$ , where  $\rho_1$  is the radial location of the  $q = 1$  surface,  $\eta$  is a parameter that was scanned between -1 and +1, and  $w_{\text{CD}}$  is the width of the gaussian ECCD profile.

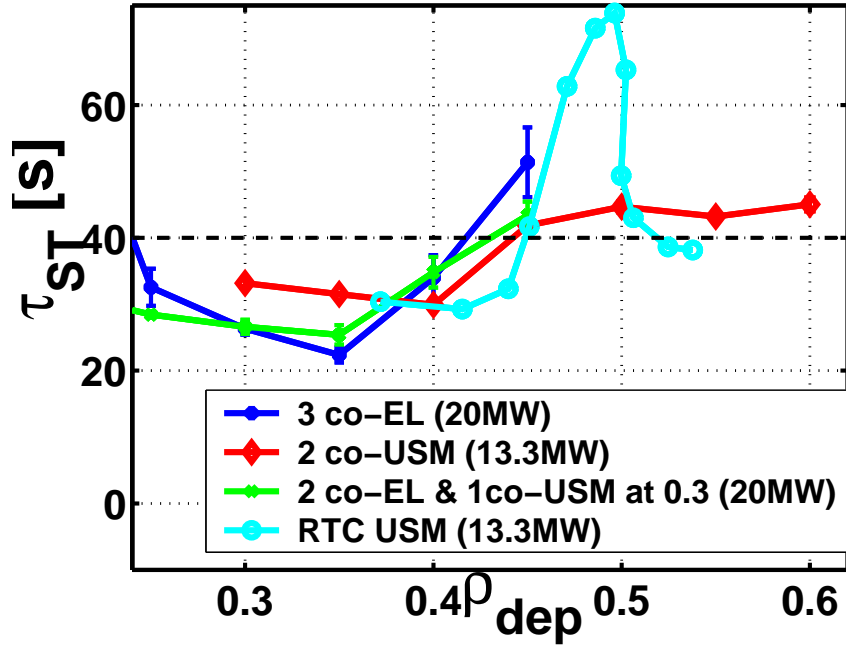


Figure 5.15: Simulated sawtooth period in the case of a full radial sweep of localized EC power, realized with either the Eq. Launch. (maximum EC power 20MW) or the USM (maximum EC power 13.3MW). The black horizontal dashed line marks the sawtooth period of the case without ECCD.

The simulated  $\tau_{\text{ST}}$  obtained with 13.3MW of co-ECCD from the USM and with  $\rho_{\text{dep}}$  controlled in real-time is plotted in Fig. 5.16 as a function of the  $\eta$  parameter. With a RTC of the  $\rho_{\text{dep}}$ , the sawtooth period can be increased up to 70s, i.e. more than 50% (Fig. 5.15). Note that the time evolutions of the value of the magnetic shear,  $s$ , at the  $q = 1$  surface, shown in Fig. 5.14b and c, result from the RTC simulations and correspond to a RTC parameter  $\eta = -0.75$  ( $\tau_{\text{ST}} = 30\text{s}$ ) and  $\eta = 0.25$  ( $\tau_{\text{ST}} = 75\text{s}$ ), respectively.

## 5.6.2 Equilibrium results

Concerning the capabilities of the two launchers for sawtooth control, it is clear that accurate predictions require transport modeling including a sawtooth period model that takes into account the stabilizing effect of alpha particles. However, in the course of this thesis, before the implementation of a full transport model for ITER accounting for a sawtooth-triggering criterion, preliminary studies have been carried out with the CHEASE code on the capability of modifying the value of  $s_1$  by ECCD injection. These



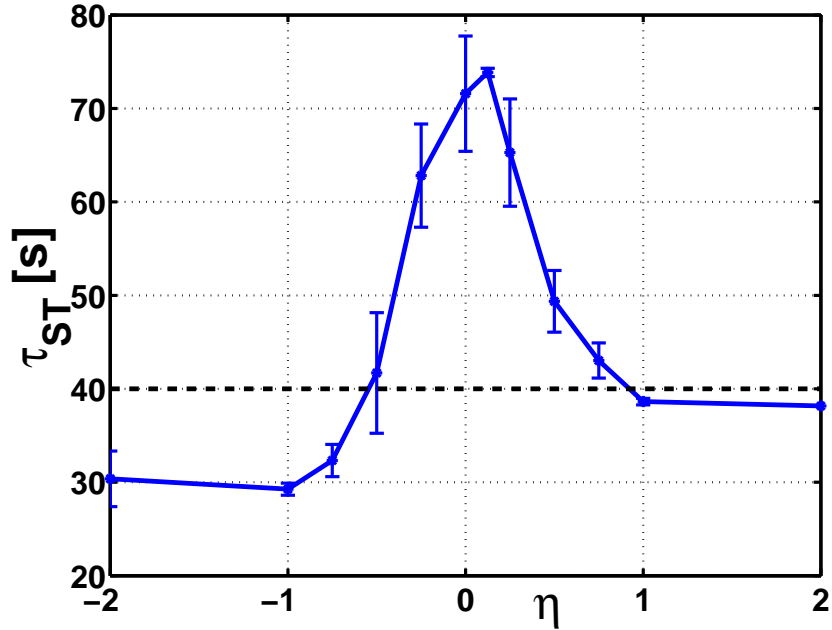


Figure 5.16: *Simulated sawtooth period obtained from the RTC modeling with injection of 13.3MW from the USM as a function of the real-time control parameter  $\eta$ .*

reconstructions were done for the ITER reference hybrid Scenario 3, characterized by a  $q = 1$  surface at  $\rho_T \sim 0.3$ . The ECCD components provided as an input to the code are Gaussian profiles with amplitude, width and total EC current derived from averaged values of early estimations by GRAY, rather than the superposed Gaussians derived from the separate launchers. Even though this model is less refined than the transport modeling presented in the previous section, the results arising from this study are still in good agreement with the former ones.

Another reason why the equilibrium calculations are instructive is that this analysis also covered the comparison in efficiencies of two possible variants of the Up. Launch., essentially differing only in the blanket shield module occupied by the launcher: that is, lowering the vertical position of the launcher makes the deposition profiles narrower, with comparable total EC current. This can be realized because greater localization occurs when the EC beam travels tangentially to the flux surface in the neighborhood of the absorption region [112], [113]. The variant occupying an upper location is the variant Up. Launch. described in the beginning of this chapter. A notation that has been common in the past to distinguish these two types of Upper Launcher indicates them as the Extended Performance Launcher (EPL, the highest and broadest of the two) and Dropped

Upper Launcher (DUL, the lowest and narrowest). Instead of changing notation, in the following analysis, we shall refer to these two variants, respectively, as the revised (or modified) Up. Launch. and the narrower Up. Launch.

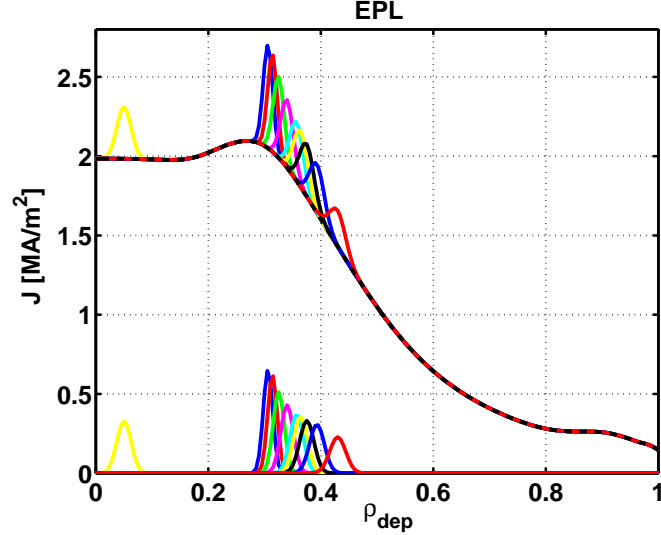


Figure 5.17: *ECCD profiles from the revised Up. Launch. and total current density profiles used as input for the CHEASE reconstructions.*

Fig. 5.17 shows the total current density and the ECCD profiles from Up. Launch. injection used in the CHEASE reconstructions; Fig. 5.18 shows the resulting  $q$  and  $s$  profiles. The original profile without ECCD is plotted in dashed-black and the circles indicate the position of the  $q = 1$  surface. Without ECCD, the value of the magnetic shear at  $q = 1$  is 0.15, which is a typical value expected at sawtooth crashes in present experiments [109] in the absence of fast particle stabilization. Gaussian profiles of co-ECCD driven by the revised Up. Launch. provided a total  $I_{cd}$  of about 100-130kA. In Fig. 5.18, by depositing co-ECCD inside or outside the  $q = 1$  radius, the shear at  $q = 1$  spans a rather large range, as it changes from just above 0 to 0.4. The increase in  $s_1$  is about a factor of 2, therefore comparable to the effect observed on the sawtooth period as the one simulated by the ASTRA code.

This modification should allow stabilization of sawteeth with  $s_1 < 0.2$  or at least a significant increase of the period with consequent delay of the first sawtooth crash. Likewise, one can increase  $s_1$  with the addition of co-ECCD inside the deposition radius and thus destabilize the sawteeth. Note that as long as the deposition location is far outside the

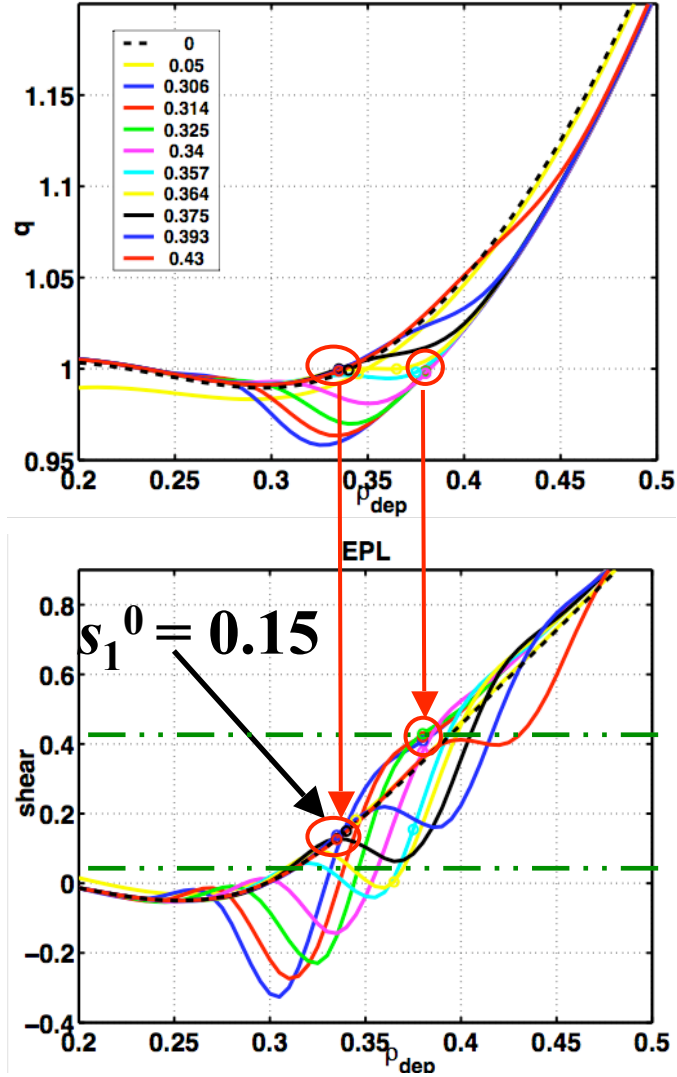


Figure 5.18: *CHEASE* reconstructed  $q$  and  $s$  profiles.

$q = 1$  surface, there is no significant effect on the shear at the  $q = 1$  location: the  $s_1$  value stays approximately constant around 0.15 (red-blue-black lines from right in the shear plot), then suddenly the  $s_1$  value drops to about 0 (yellow line in shear plot), and if one keeps on depositing more inward, the shear then rapidly starts increasing (cyan line in the shear plot) and finally stays constant at around 0.4 even if we keep on moving more on-axis (magenta-green-red-blue lines on the shear plot).

The same kind of steady state study done for the revised Up. Launch. can be compared to the other variant with even narrower deposition. Fig. 5.19 shows the difference of  $s_1$  from

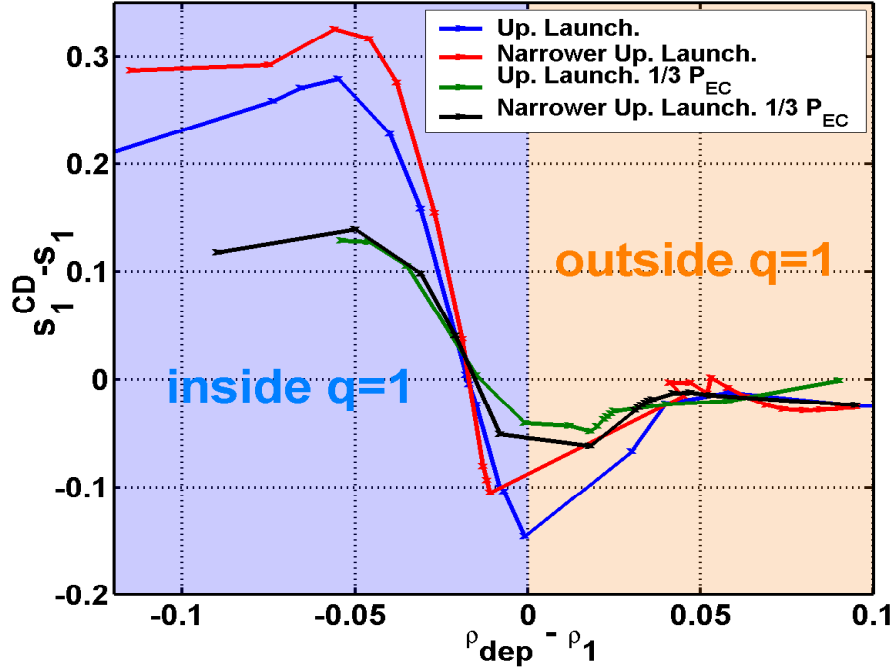


Figure 5.19: Variation of  $s_1$  from its original value without ECCD as a function of the difference between the ECCD deposition location and the  $q = 1$  radius of the case without ECCD, as from the CHEASE reconstructions.

the original value without ECCD as a function of  $\rho_{\text{dep}}$  minus the  $q = 1$  radius of the case without ECCD; the light blue shaded region corresponds to depositions inside  $q = 1$  and the yellow outside  $q = 1$ . This figure can be qualitatively compared to Fig. 5.15, keeping in mind that the two  $y$ -axes report physical quantities ( $s_1$  and  $\tau_{\text{ST}}$ ) that have inverted behaviors for the same phenomenon: with deposition inside  $q = 1$ ,  $s_1^{\text{CD}} - s_1^0$  increases, therefore a sawtooth crash is triggered more rapidly and  $\tau_{\text{ST}}$  decreases (and viceversa with deposition outside  $q = 1$ ).

The equilibrium modeling shows that the sawtooth destabilization should be somewhat easier to obtain than stabilization, because the radial extent inside  $q = 1$  at which one can deposit co-ECCD and still obtain a significant shear increase is large, whereas one has to be very well localized around a specific region outside  $q = 1$  to obtain a significant decrease in  $s_1$  and thus have a chance to stabilize sawteeth. The transport modeling has also identified a large region where the value of  $\tau_{\text{ST}}$  is decreased. From Fig. 5.18, one also

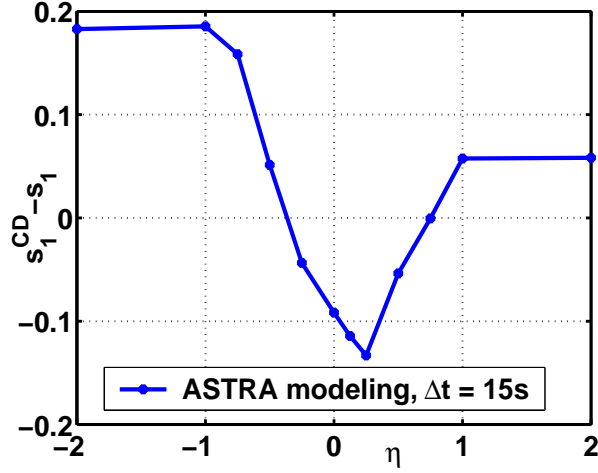


Figure 5.20: Variation of  $s_1$  from its original value without ECCD 15s after a sawtooth crash as a function of the difference between the ECCD deposition location and the  $q = 1$  radius of the case without ECCD, as from the ASTRA modeling. The value of  $s_1$  at the crash varies between 0.54 and 0.61 for the RTC case.

sees that the  $q = 1$  radius changes rapidly when the magnetic shear decreases in between the two red arrows. Therefore the optimum deposition needs to be adjusted in real time in order to follow the  $q = 1$  radius and allow optimum sawtooth stabilization, as seen in Fig. 5.16 with the ASTRA simulations.

Quite interestingly, the results of the steady state simulations show that the narrower deposition (here shown in red and black) does not significantly change the steady state variation of  $s_1$  with respect to the standard optimized Up. Launch. A criterion which has been employed for sawtooth stabilization assumes the variation of the shear at  $q = 1$  proportional to the figure of merit:  $\eta_{ST} = I_{cd} / w_{cd}^2$  [114]. This criterion has been used in the past to compare the efficiencies of these two variants of the optimized Upper Launcher [88]. According to this figure of merit, the efficiency for the narrower deposition variant should be about a factor of 4 higher than the standard optimized Upper Launcher, however this does not appear to be the case. From simple analytical considerations at steady state, the magnetic shear variation at  $q = 1$ ,  $\Delta s = s_1^{CD} - s_1^0$ , is found to be a different function of  $I_p$ ,  $I_{cd}$ ,  $j$ ,  $j_{cd}$ , etc, depending on the radial location of the EC deposition with respect to  $\rho_1$ , i. e. the position of the  $q = 1$  surface. From large aspect ratio relations, we can

express the magnetic shear as:

$$s(\rho) = 2 - \frac{2S(\rho)j(\rho)}{I_p(\rho)},$$

where  $S(\rho)$  is the area of the  $\rho$  flux surface,  $j$  is the total current density at  $\rho$  and  $I_p(\rho)$  is the total current within  $\rho$ . In this way, we see that:

$$\Delta s \sim \begin{cases} I_{cd}(\rho_1)/I_p(\rho_1) & \text{if } \rho_{dep} \ll \rho_1 \\ -j_{cd}^{peak}/j(\rho_1) & \text{if } \rho_{dep} \approx \rho_1 \\ 0 & \text{if } \rho_{dep} \gg \rho_1. \end{cases}$$

Therefore, for depositions well inside or well outside the  $q = 1$  surface, the two variants of the Up. Launch. will give comparable effects, since the total ECCD driven by them is comparable. At depositions around the  $q = 1$  surface, instead, the value of  $j_{cd}^{peak}$  becomes important and thus one would expect the narrower Up. Launch. to be significantly more efficient. Fig. 5.19 shows that the gradient of the narrower Up. Launch. curve is steeper than that of the Up. Launch., indicating that the magnetic shear variation near  $\rho_{dep} \sim \rho_1$  for the narrower Up. Launch. becomes smaller than -0.15. Further simulations should be carried on at deposition locations closer to  $\rho_1$  in order to complement the data in this region. In addition, we see that  $\Delta s$  is similar for both options for  $\rho_{dep} < \rho_1 - w_{cd}$  and it is about 1/3 when only 1/3 of the EC power is injected. Therefore it does follow the  $I_{cd}/I_p$  trend as indicated above.

## 5.7 Advantages of counter-ECCD

### 5.7.1 Pure EC Heating

The importance of a pure EC heating system for ITER resides in its capabilities to control density peaking. In a burning plasma, a peaked density profile produces a larger amount of fusion power and bootstrap current with respect to a flat profile [115], providing a boost of fusion power of more than 30% for fixed  $\beta$  and average density with respect to the usual assumption of a flat density profile [115]. On the other hand, a drawback to density peaking is an increased proneness to heavy impurity accumulation. Impurities in the plasma core enhance radiation losses and plasma dilution, with deleterious consequences in fusion reactivity. In particular, high-Z impurities, with the associated risk

of plasma disruptions, cannot be tolerated. Discharges with increased density peaking have shown a tendency for increased central concentrations of high-Z impurities in many tokamaks, such as JET [96], AUG [97], DIII-D [116]. A too peaked density profile may also have negative consequences on the MHD stability. Recent experimental results in AUG and JET H-mode plasmas indicate that the density peaking is correlated with the plasma collisionality [117], [118]. Scaling expressions suggest that the density peaking factor,  $n_{e0}/\langle n_e \rangle$ , may exceed 1.5 in ITER [119], so that, even in presence of strong  $\alpha$ -heating, the density profiles in the ITER standard scenario will not be flat, as usually assumed, but peaked. The application of radio-frequency heating has been shown to provide a flattening effect on the density profile, and the pump-out induced by these means is more pronounced when heating is delivered through the electron channel [120], [121]. It is then clear that central ECH will be extremely important for ITER, because it is useful to control density peaking.

At present, the ITER EC system does not provide the possibility of central heating by ECRH. Having an Eq. Launch. capable of both co- and counter- injection allows to achieve “pure” heating by applying a balanced mixture of both co- and counter-ECCD. Therefore, two scans in the deposition location of the EC waves have been run, in which the ECH component has been added to the standard ITER Scen 4-type I in two different ways: in the first case, by providing a mixture of both ECCD and the corresponding EC power density, while in the second case only the ECH power density has been provided. It should be noted that in this context, we wish to show the equivalence between the application of combined positive and negative EC current drive and pure heating. Since the transport model employed does not take into account the diffusive equation for the electron density ( $n_e$  is fixed), this analysis does not aim at estimating the capabilities of the EC system in controlling the density peaking, but rather at underlining the feasibility of pure heating with the suggested design.

The small positive or negative gaussian profiles in Fig. 5.21 are the  $j_{eccd}$  profiles respectively from the low and top rows of the Eq. Launch. (6.7MW each), at different deposition locations. By simultaneously driving these two current density components, opposite in sign, to the plasma of Scenario 4-type I, the resulting ECCD profile is very small. Consequently, the total current density profile is essentially unaffected: even in the most perturbed case, with very central deposition ( $\rho_{dep} = 0.13$ ), the difference between the

original  $j_{\text{tot}}$  (black curve) and the one obtained with the additional EC component is negligible.

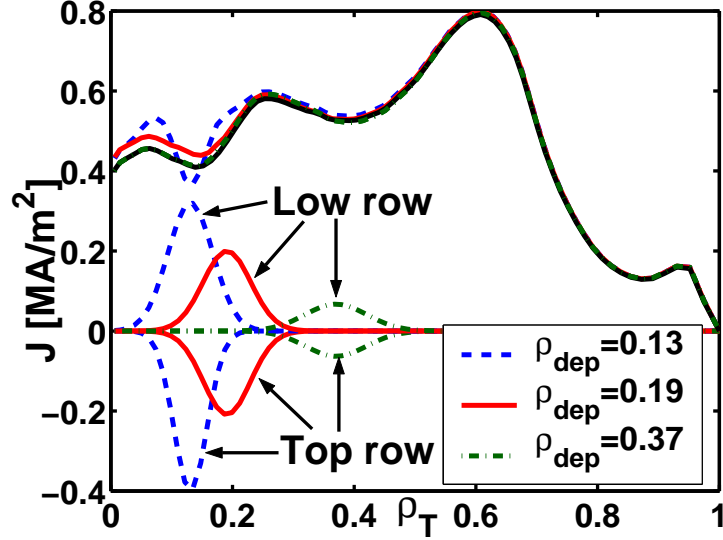


Figure 5.21: *ECCD density components with opposite sign, at different radial depositions (small gaussian profiles), with no net resulting EC current. The total current density profile is essentially unaffected.*

The corresponding  $q$  and  $s$  profiles are shown in Figs. 5.22 and 5.23, respectively. The left plots correspond to the case with a small ECCD component, whereas the right plots report profiles obtained from simulations in which the  $j_{\text{eccd}}$  component has been artificially fixed to a uniform null profile (as seen from the legend, the values of  $I_{\text{eccd}}=0$ ), nonetheless using the calculated EC power density component  $P_{\text{EC}}$ . Again the  $q$  and  $s$  profiles are essentially unaffected.

Finally, Fig. 5.24 shows the normalized values of simulated quantities such as  $I_{\text{eccd}}$ ,  $Q$ , central  $T_e$  and  $T_i$ , as a function of the EC waves deposition location,  $\rho_{\text{dep}}$ . The superscript “0” indicates the corresponding quantity for the ITER reference Scenario 4-type I, without any additional ECH or ECCD. The total net driven EC current is shown to be negligible, being  $I_{\text{eccd}} < 0.2\% I_p$ , as shown in Fig. 5.24a. The addition of 13.3MW of ECH power causes a small degradation of the fusion power amplification, making it drop to just below 5 (Fig. 5.24b). The modest electron heating effect is shown in Fig. 5.24c and the consequent ion cooling in Fig. 5.24d. These simulations underline that the EC system for ITER is not meant as a bulk heating (or current drive) source, but rather as a surgical



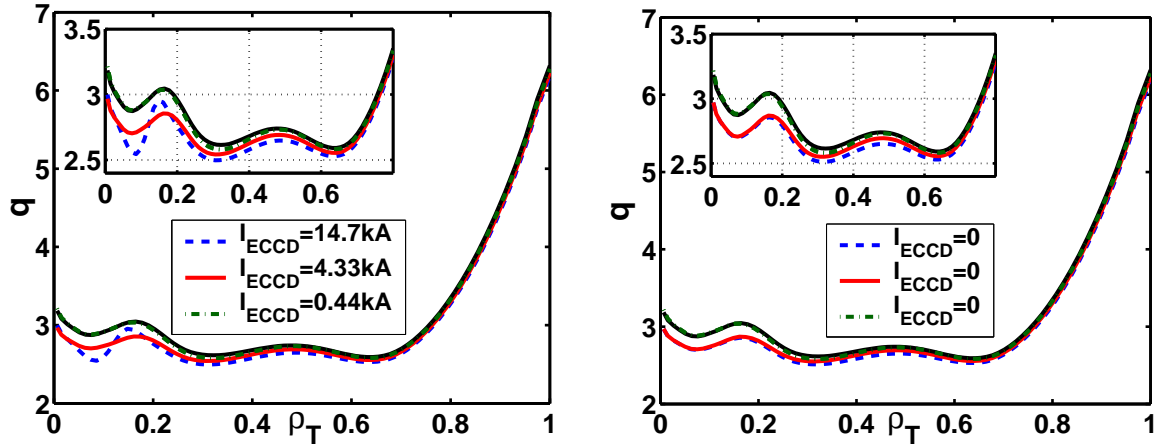


Figure 5.22: Profiles of the safety-factor for three different deposition locations of EC waves: a) case of small yet non-zero ECCD component; b) case of zero ECCD. For case a), the EC current drive density is negligible with respect to  $I_p$ .

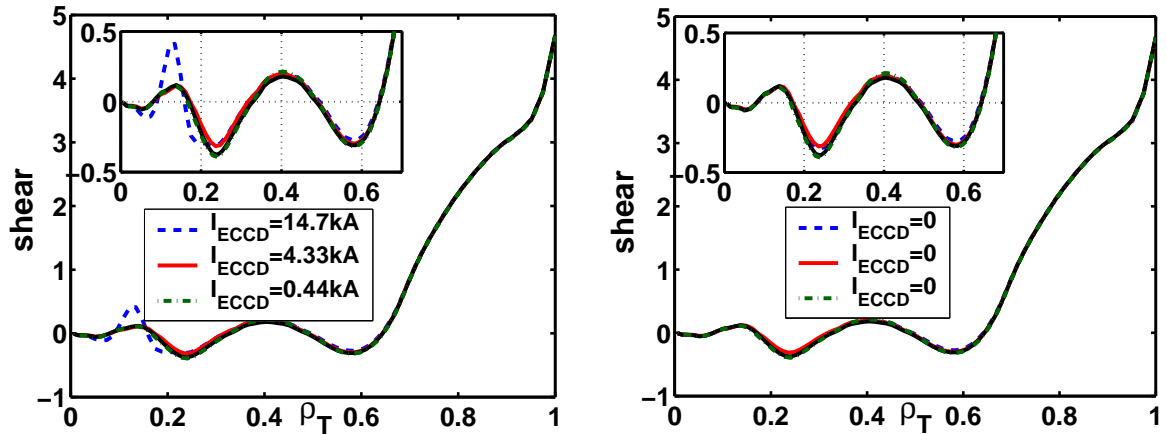


Figure 5.23: Profiles of the magnetic shear for three different deposition locations of EC waves: a) case of small yet non-zero ECCD component; b) case of zero ECCD.

tool, given its large localization and flexibility.

Pure heating with full EC power, 20MW, is also possible using a combination of power from both the Up. Launch. and Eq. Launch. Fig. 5.25a shows the values of the total EC current as a function of the deposition location: at around  $\rho_T = 0.35 - 0.4$ , the values of  $I_{eccd}$  driven by the top mirror of the Eq. Launcher (which in the revised design would be negative) is comparable to the total EC current driven by twice the power - i. e. 13.3MW of the USM of the Up. Launch. Therefore this allows injecting 20MW of EC power with no (or negligible) net driven current. This is shown in Fig. 5.25b, where such a combination

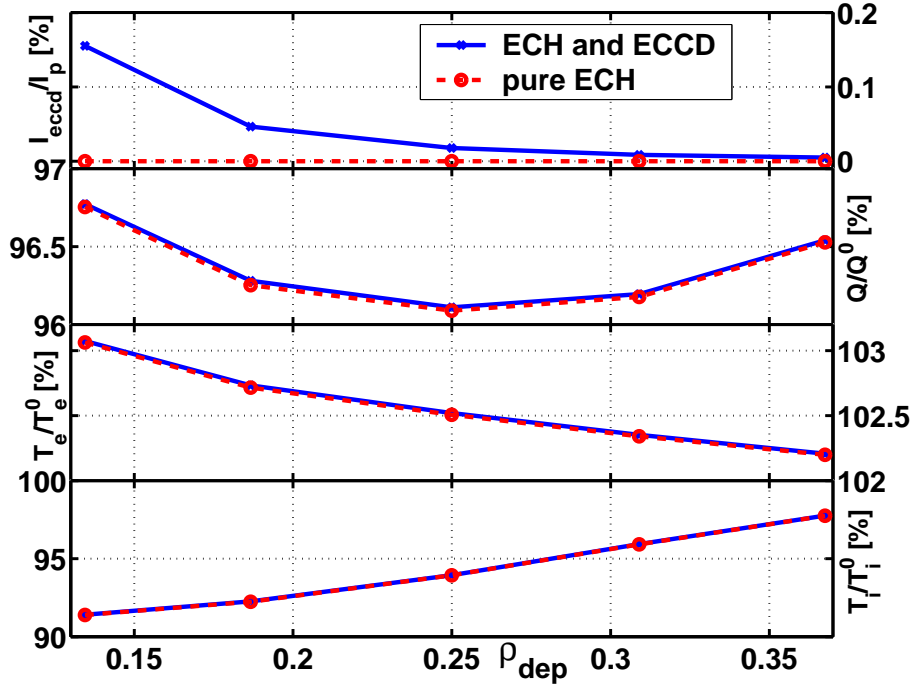


Figure 5.24: Normalized values of simulated quantities such as  $I_{\text{eccd}}$ ,  $Q$ , central  $T_e$  and  $T_i$ , as a function of the 13.3MW EC waves deposition location,  $\rho_{\text{dep}}$ . The superscript “0” indicates the corresponding quantity for the ITER reference Scenario 4-type I, without any additional ECH or ECCD.

of ECCD profiles is reported. By depositing EC power with the USM at two separate radial locations (6.7MW at each location),  $\rho_T = 0.36$  and  $\rho_T = 0.42$ , the resulting driven current balances out the counter-ECCD driven by the 6.7MW Top mirror. The net driven current is 10kA, i.e. about 0.1% of the total plasma current for the Scenario 4 (9MA).

### 5.7.2 Unvaried control capabilities of the system

It is relevant to remark that the revised variant of the EC system does not prevent driving 20MW co-ECCD. Indeed, even if one steering mirror assembly of the Eq. Launch. is flipped (to permit up to 6.7MW of counter-ECCD), co-ECCD with 20MW is still feasible using a combination of ECCD from the Up. Launch. (with  $\rho_T$  outside 0.3) and the Eq. Launch. with  $\rho_T$  inside  $\sim 0.41$ .

Using as a target the Scenario 4 type-II in [86], we have compared the plasma current density profiles sustained, first, by three Eq. Launch. rows in full-power co-ECCD and,

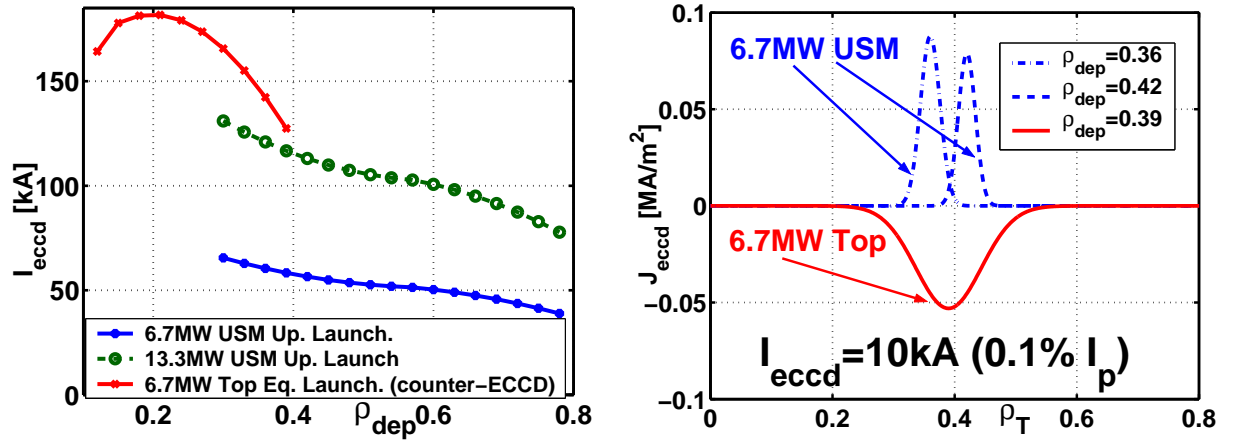


Figure 5.25: a) Values of  $I_{\text{eccd}}$  from the USM of the Up. Launch. and the top mirror of the Eq. Launch. as a function of the deposition location. b) Possible combination of ECCD profiles to provide 20MW of pure ECH.

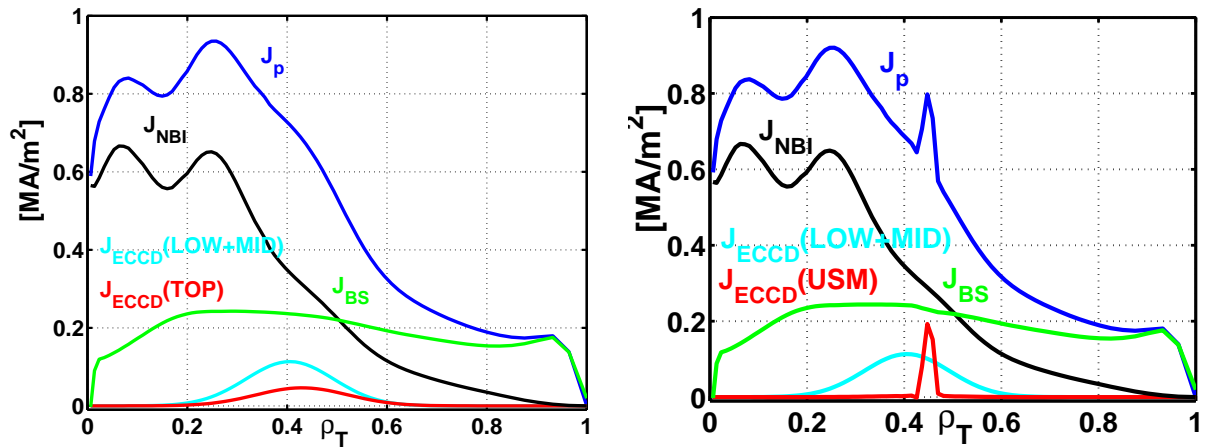


Figure 5.26: Comparison of the current density components obtained by driving co-ECCD a) with 3 rows of the Eq. Launch. or b) with 2 rows of the Eq. Launch. and 1 co-ECCD from the USM. The corresponding safety factor profiles are equivalent (Fig. 5.27).

secondly, by two Eq. Launch. rows of co-ECCD (13.3MW) and the remaining 6.7MW injected from the USM at  $\rho_T = 0.43$ . The simulated current density components for these two cases are shown in Fig. 5.26. Some of these components are common for both cases: in black the NBI component, in green the bootstrap component, and in cyan the co-ECCD driven by two rows of co-ECCD. The remaining co-ECCD component, indicated by the red curves, are instead different, since driven from different EC launchers: for the first case from the top row of the Eq.Launch. in co-ECCD (as in the present design),

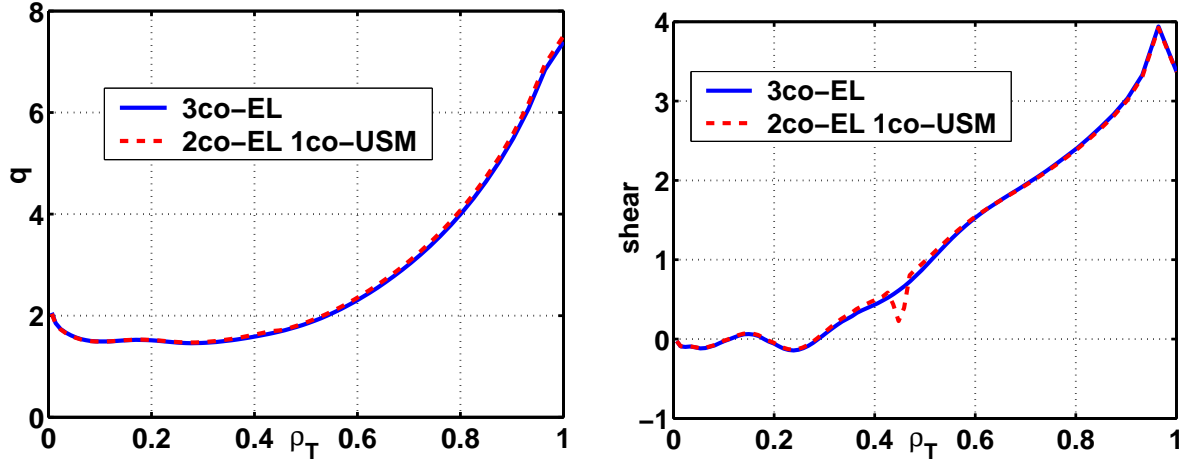


Figure 5.27: a) Safety-factor and b) magnetic shear profiles for the two analyzed cases of 20MW co-ECCD, either driven all by the Eq. Launch. or by a combination of the two launchers. Equivalence of the two cases is clear.

whereas for the second case from the USM of the Up. Launch. (as suggested by the design revision). Even though the total current density profiles (blue curves in Fig. 5.26) slightly differ at  $\rho_T \sim 0.43$ , the profiles of  $q$  are unaffected, as seen from Fig. 5.27. The local drop of the magnetic shear appearing with the USM option (dashed line) can be reduced significantly by spreading the eight beams launched from the USM. Since the total EC driven current is very similar, despite the lower current drive efficiency of the USM, the total plasma current is almost constant:  $I_p = 8.42\text{MA}$  in the first case and  $I_p = 8.34\text{MA}$  in the second case. This confirms that the two current drive schemes are equivalent, and therefore the EC system capabilities are unvaried. This would allow ITER to carry out the suggested EC design modifications without any losses in the system capabilities, but, on the contrary, providing the EC system with increased flexibility, as shown in the following Section.

### 5.7.3 Increase of the $q$ profile control

This section addresses the ability of the Eq. Launch. to control the  $q$  profile, particularly during reverse shear and hybrid scenarios. Since the  $q$  profile within  $\rho = 0.2$  is not so well resolved and is very sensitive to small changes in the current density profile, we prefer to look at the difference between  $q(\rho = 0.2) = q_{0.2}$  and the minimum  $q$  value,  $q_{\min}$ . Counter-ECCD provides a better control of the quantity  $\Delta q = q_{0.2} - q_{\min}$ . Starting with the

advanced Scenario 4-type I, Fig. 5.28a shows this difference as a function of the deposition location of ECCD for various combinations of co- or counter-ECCD. The color regions indicate the degree of shear reversal, as shown in Fig. 5.28b and previously introduced by[86]:  $\Delta q < 0$  (positive shear, bottom region),  $\Delta q \sim 0$  (zero shear), Weakly Reversed Shear (WRS,  $\Delta q \lesssim 0.5$ ) and Strong Reversed Shear (SRS,  $\Delta q \gtrsim 0.5$ ). The corresponding  $q$  profiles obtained for various deposition locations are shown in Fig. 5.29 and 5.30. As

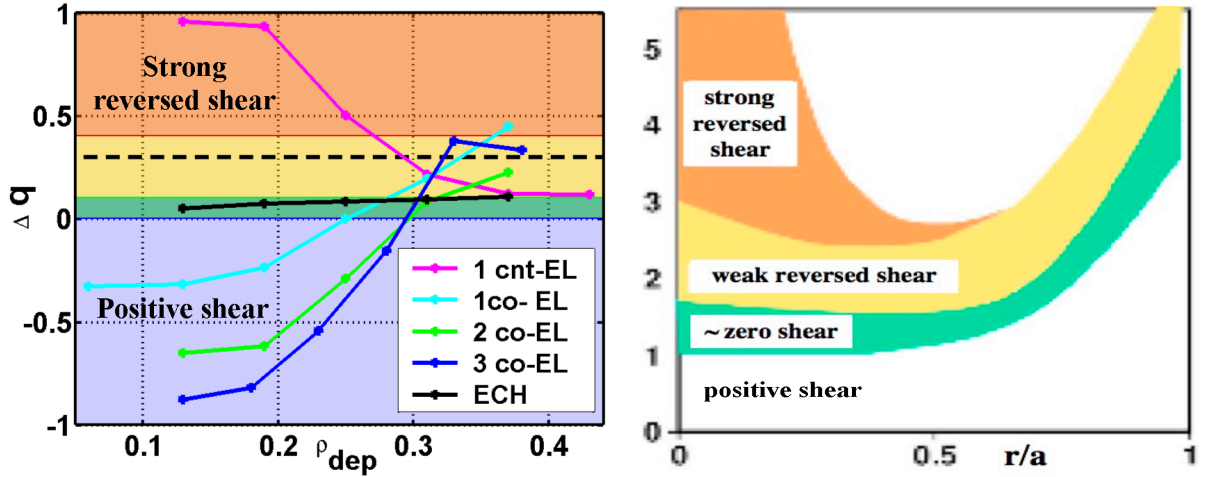


Figure 5.28: a) Control of  $\Delta q$  as a function of the ECCD deposition location, achievable with various combinations of co- and counter-ECCD. b) The corresponding definition of shear reversal according to [86].

shown in Fig. 5.28a, at present the  $\Delta q$  control is somehow limited:  $\Delta q$  varies between -0.9 to 0.4. In addition, the difference between the present off-axis co-ECCD case and pure heating is relatively small, as seen in Fig. 5.22a and Fig. 5.30b. Much improvement can be obtained with counter-ECCD, since  $\Delta q$  is then expected to vary between -0.6 to 1. Besides providing a wider range of  $\Delta q$  control, counter-ECCD opens the possibility to reach SRS, which cannot be obtained with off-axis co-ECCD. Moreover, the application of 20, 13.3 or 6.7MW of EC power in the centre from the Eq. Launch. in co-ECCD can be counter productive, essentially filling in the hollow current profile. With only 1/3 of central power in counter-ECCD, Strong Reversed Shear can be attained, without loss in control, whereas even with more off-axis deposition, co-ECCD only allows to reach Weakly Reversed Shear.

The study on the increased capabilities allowed by the revised design presented so far has

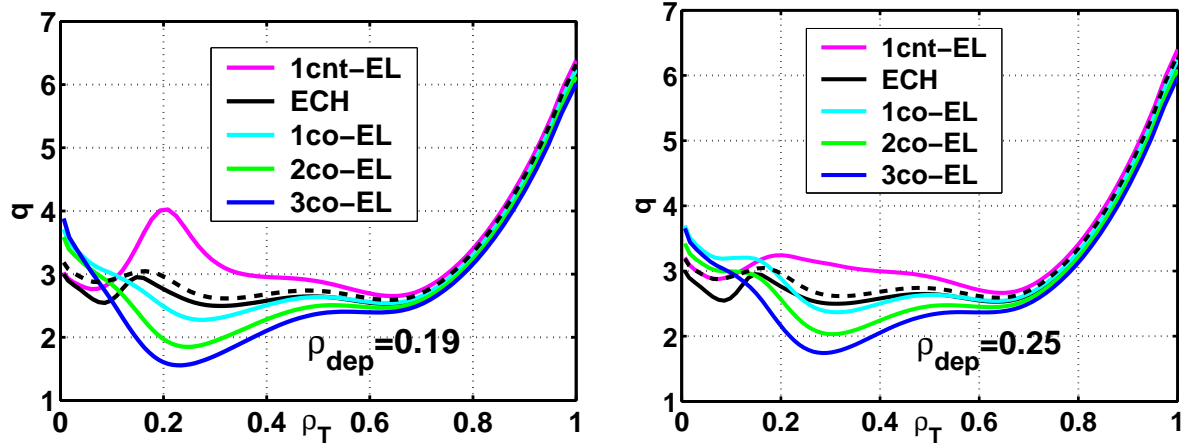


Figure 5.29: *Safety-factor profiles for a)  $\rho_{\text{dep}} = 0.19$  and b)  $\rho_{\text{dep}} = 0.25$ , Scenario 4-type I.*

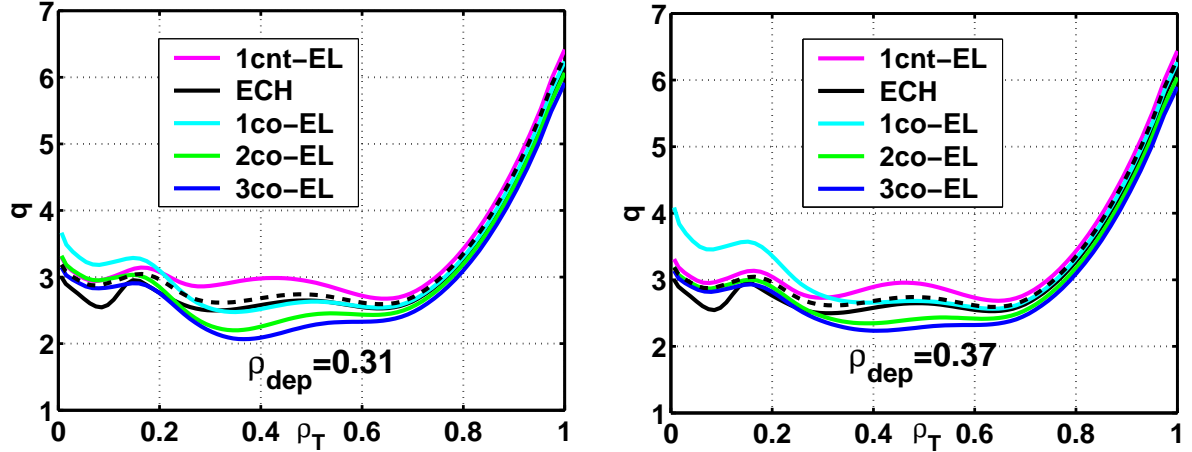


Figure 5.30: *Safety-factor profiles for a)  $\rho_{\text{dep}} = 0.31$  and b)  $\rho_{\text{dep}} = 0.37$ , Scenario 4-type I.*

been performed with the ASTRA transport code. Previously, the CHEASE equilibrium code had been used to carry out this analysis [88]. Even though the modeling does not take into account the resistive evolution of the plasma current density profile, the results from the CHEASE reconstructions are still in good agreement with the transport simulations. They are also relevant because the aim of the modeling on this Scenario 4 is to reach a steady state simulation. Fig 5.31 shows a comparison of the  $q$  profiles obtained with central Eq. Launch. injection resulting from the ASTRA and CHEASE modeling, respectively, for Scenario 4-type I. The deposition location is slightly more central for the CHEASE simulation, being  $\rho_T = 0.13$  for Fig. 5.31a and  $\rho_T = 0.08$  for Fig. 5.31b.

Concerning case b), the blue solid and dashed curves are the  $q$  profiles obtained by driving co-ECCD with respectively 20 and 10MW of EC power from the Eq. Launch., since 10MW can reasonably be considered the minimum amount of EC power used, if heating with EC waves is needed. The dark red region of Fig. 5.31b indicates the range of  $q$  profile that one can obtain by driving up to 1/3 of the total EC power, corresponding to the counter-ECCD driven by 1 row of mirrors. The light red region corresponds, instead, to having the possibility of 20MW of counter-ECCD, which is therefore shown to leave the safety factor profile essentially unvaried with respect to having only one Eq. Launch. row driving counter-ECCD.

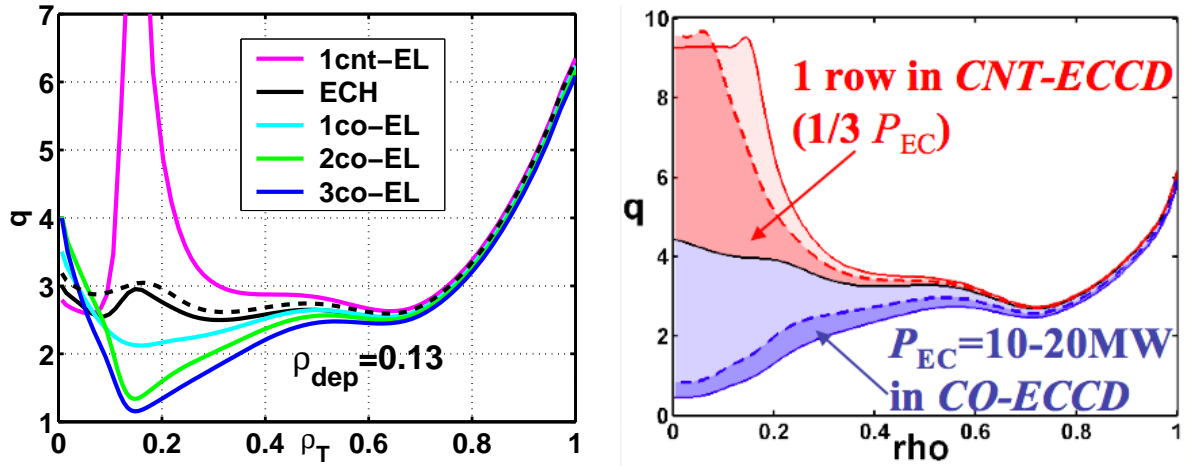


Figure 5.31: Comparison of a) ASTRA and b) CHEASE  $q$  profile control by the Eq. Launch. with various combinations of co-/counter-ECCD, for Scenario 4-type I.

As a general consideration, if central heating is needed, for example to assist during the transition between L to H mode, with the present EC design we would be limited to the profile range comprised in between the blue and green curves for case a) and the blue solid and dashed curves for case b), since pure heating is not foreseen.

The effect on the  $q$  profile of central co-/counter-ECCD injection driven by the improved Eq. Launch. (based on the equilibrium reconstruction) is shown also for Scenarios 2 and 3, in Fig. 5.32. Again, the range of variation of central  $q$  with respect to the original  $q$  profile (the solid black line on this plot) indicates the flexibility in controlling  $q_0$  with counter-ECCD. For Scenario 3, the calculations have again been done for the full EC power of 20MW as well as for smaller fractions of it, to also account for possible system limitations. The  $q$  profiles obtained by injecting the full EC power are the blue and red

solid lines, while the red dashed curve indicates the safety factor obtainable if the counter-ECCD were driven only by one row of mirrors, corresponding to  $1/3$  only of the total EC power. Even with this 6.7 MW of cnt-ECCD,  $q$  could be raised above 1, therefore allowing the possibility to avoid sawteeth.

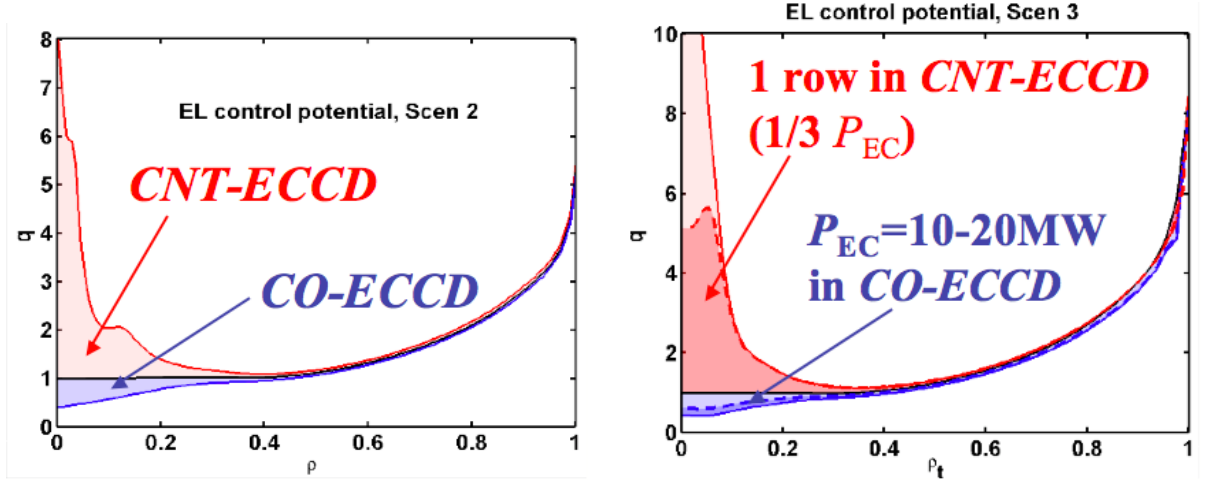


Figure 5.32: *CHEASE* reconstructions of the  $q$  profile control obtained with different mixtures of co-/counter-ECCD, for Scenarios 2 (a) and 3 (b).

## 5.8 Current redistribution

To provide an example of the time required to modify the  $j_p$  and  $q$  profiles, we have varied the ECCD profile from being sustained by 2 Eq. Launch. rows of co-ECCD to being sustained by 1 Eq. Launch. row of counter-ECCD (Fig. 5.33a). This variation in ECCD starts from a steady state and occurs in 5s. Following this change, a large inductive current component is generated, shown in Fig. 5.33b, and the  $q$  profile becomes more and more reversed, Fig. 5.34. Even though the whole time evolution before reaching another steady state takes about 1000s, the central  $j_{ohm}$  halves in  $\sim 200$ s. The initially positive magnetic shear becomes a zero shear in approximately 400s, then WRS  $\sim 100$ s later and finally SRS in the following  $\sim 200$ s.



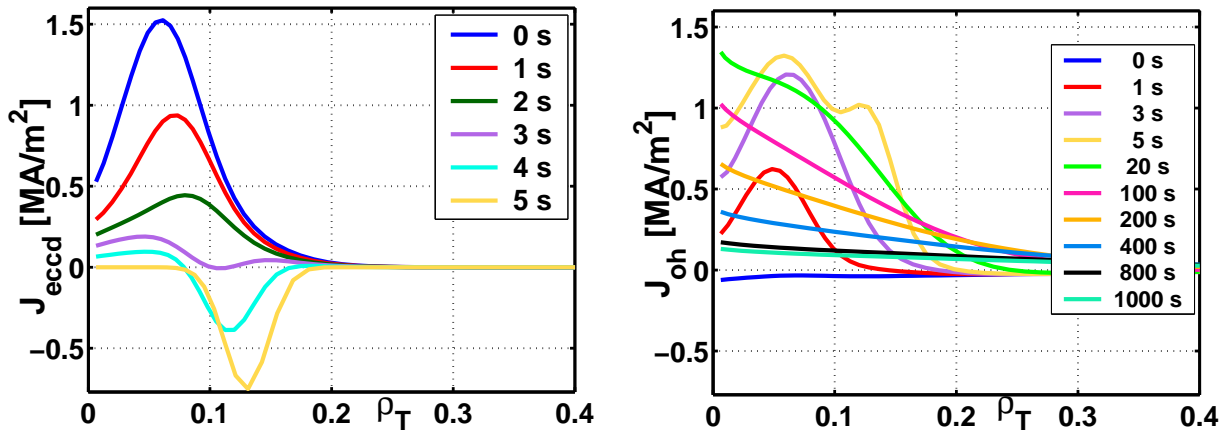


Figure 5.33: a) The ECCD component is varied from being sustained by 2 rows in co-ECCD to 1 row in counter-ECCD during 5s; b) inductive current density profiles following the ECCD modification.

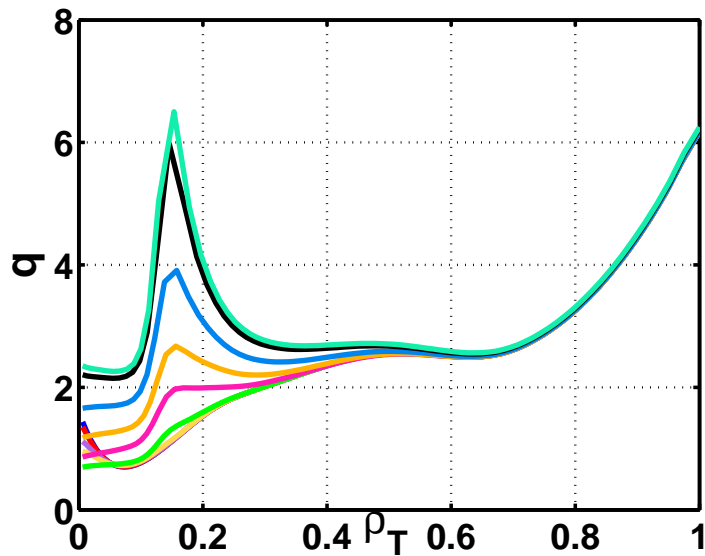


Figure 5.34: Safety-factor profiles following the ECCD modification. Note that the reconstruction is less accurate inside  $\rho_T = 0.1$ .

## 5.9 Summary and conclusions

The effect of the predicted local electron cyclotron current, driven by the optimized electron cyclotron system, on ITER has been discussed. A design variant was recently proposed to enlarge the physics program covered by the Up. and Eq. Launchers. The revised design of the ITER EC system maintains the original control capabilities with high ef-

iciency and, at the same time, allows for useful additional applications which are not foreseen at present, such as pure heating and counter-ECCD. This offers more flexibility to the EC system, without causing any loss in control.

By extending the functionality range of the Up. Launch., significant control capabilities of the sawtooth period can be obtained. The Up. Launch. improvement still allows enough margin to exceed the requirements for neoclassical tearing mode stabilization, for which it was originally designed. The analysis of the sawtooth control has been carried out with the ASTRA transport code, coupled with the threshold model by Porcelli, to study the control capabilities of the improved Up. Launch. on the sawtooth instability. The simulations take into account the significant stabilizing effect of the fusion alpha particles. The sawtooth period can be increased by a factor of 1.5 with co-ECCD outside the  $q = 1$  surface, and decreased by at least 30% with co-ECCD inside  $q = 1$ . Results from equilibrium reconstructions and a discussion on the relevant conditions for magnetic shear variation have also been presented.

The present ITER base-line design has the electron cyclotron launchers providing only co-ECCD. The Eq. Launch. can be modified in such a way that 1/3 of the power is injected in the counter-ECCD direction. Then, there is adequate flexibility between the Eq. Launch. and Up. Launch. to provide independent control of the driven current and heating ratios. The variant for the Eq. Launch. therefore proposes the possibility to drive counter-ECCD with 1 of the 3 rows of mirrors: the counter-ECCD can then be balanced with co-ECCD and provide pure ECH with no net driven current. The difference between full co-ECCD off-axis using all 20MW from the equatorial launcher and 20MW co-ECCD driven by 2/3 from the equatorial launcher and 1/3 from the upper launcher is shown to be negligible. Both the  $q$  and  $s$  profiles are similar. Cnt-ECCD also offers greater control of the plasma current density, therefore this analysis addresses the performance of the equatorial launcher to control the central  $q$  profile. The equatorial launcher is shown to control very efficiently the value of  $q_{0.2} - q_{\min}$  in advanced scenarios, if one row provides counter-ECCD.

In all, the proposal provides a greater potential for controlling MHD activity and the plasma current density profile, and access to essentially the entire plasma cross section. In particular, besides stabilizing NTMs, with the revised system one can also destabilize and stabilize the sawtooth instability, provide up to 20MW of “pure” central heating (without

additional CD) and control  $\Delta q$  in particular in advanced scenarios. Counter-ECCD offers greater control, because it allows accessing Strong Reversed Shear. Off-axis co-ECCD only enables Weakly Reversed Shear and without a clear gain over off-axis heating. Moreover, counter-ECCD can balance co-ECCD and provide pure central heating up to 20MW. We have also shown that with a combination of current driven from the USM and the EL, driving 20MW of co-ECCD is still possible at  $Q = 5$ , with a negligible difference (1%) in the steady state plasma current.

# Chapter 6

## Conclusions and perspectives

### 6.1 Conclusions

The current density profile is a fundamental quantity for the study of transport in the frame of tokamak research. The understanding of transport has become of primary importance for thermonuclear fusion because transport phenomena in tokamaks can impose strong limitations to magnetic plasma confinement. This thesis has presented extensive modeling of the current density profile in tokamak plasmas, investigating its control, and its relation to electron transport.

During this work, we have been mainly involved in the development and application of numerical tools which are intended for tokamak plasma simulations. The study has been carried out with the use of the existing equilibrium code CHEASE and the transport code ASTRA, in both steady state and transient tokamak scenarios. Three main topics have been tackled in this framework: firstly, the analysis and simulation of electron Internal Transport Barriers in TCV, principally focusing on their link with the appearance of a zero magnetic shear surface; secondly, the realization and analysis of Swing ECCD discharges, with particular interest in the different electron transport properties exhibited depending on the value of the modulated magnetic shear; finally, the modeling of the effects of local ECH&CD on the sawtooth period and current density profile in ITER.

During the first part of this work, we have especially regarded advanced TCV scenarios, characterized by an electron Internal Transport Barrier, and their relation to the magnetic shear profile. The results have shown that the formation of the electron internal trans-

port barrier is clearly linked with the reversal of the magnetic shear in all cases studied, regardless of the different heating and current drive schemes. No indications were found of discrete effects related to low order rational  $q$  surfaces. On the contrary, the increase of confinement along with the negative shear is gradual, but constant, indicating that the transition is smooth, although it can be very fast [81].

Generation of a Swing ECCD in L-mode plasmas, was done at TCV, in which the modulation of ECCD at various radial positions is the only actuator for the observed modifications in the electron transport properties [122]. These exhibit inverted behaviors depending on whether the co- and counter-ECCD are injected on- axis or off-axis, in agreement with gyrokinetic linear simulations, which ascribe an opposite transport dependence on the magnetic shear. The interpretative and transport numerical analysis confirms the strong link between the electron transport and magnetic shear, both of which are modulated around the EC deposition region.

Thirdly, the extensive study regarding the effects of local ECCD in ITER has pointed out that modifying the steering ranges of the Equatorial and Upper Launchers can provide improved access and avoid most of the EC systems limitations. If the Equatorial Launcher is modified with one steering row in the counter direction, adequate system flexibility will be provided. It will then be possible to inject 20MW of EC power ranging from pure heating to pure co-ECCD, as well as 6.7MW in counter-ECCD. This offers a decoupling of the heating and current drive functions of the EC system without increasing its complexity. The efficiency in decreasing the sawtooth period is still guaranteed, whereas the efficiency in increasing the sawtooth period would be greatly enhanced with the development of a real time control. In addition, counter-ECCD to co-ECCD in the core will allow a detailed control of the  $q$  profile for all scenarios, either for MHD control (Neoclassical Tearing Modes, Toroidicity-induced Alfvén Eigenmodes, sawteeth, infernal modes) or transport level control [123].

## 6.2 Perspectives

During this thesis, we have been involved in several research topics in the field of tokamak plasmas, from transport calculations up to the design and analysis of new experiments. The results, fruit of both individual work and collaborations with other theoretical and

experimental researchers, can be considered of relevance and utility for the design and operation of next devices towards a fusion reactor, and are of interest for the fusion physicists community. By definition, research work is never finished, since it constantly brings about new questions and open issues. This thesis has led to new research perspectives and suggests the following items:

- ◇ Determining the usefulness of ITBs for a reactor requires further knowledge on the electron, ion and impurity transport, therefore the effort concerning eITBs should be continued on TCV. New fully-noninductively sustained off-axis co-ECCD discharges should be realized at  $Z = 0$ , to include measurements of ion temperature and carbon density profile from CXRS. Having a full set of plasma parameters will be useful for an accurate modeling of the current density profile and for a complete comparison between theory and experiment as well.
- ◇ The analysis of Swing ECCD should be carried on by a fine shot-to-shot scan of the EC deposition location, in order to clearly identify the radial location at which the inversion in transport properties occur. This scan should be complemented by discharges characterized by different values in actuator parameters, such as the total injected power and the modulation frequency. This should allow a test of the dependence of the inversion location with the plasma parameters. Moreover, pure ECH discharges should accompany any successful pair of Swing ECCD discharges. Before carrying on this work, however, the origins of the heating misbalance should be assessed, by performing further deposition location tests.
- ◇ The transport study on the synergy between the Upper and Equatorial Launchers should be extended to further ITER scenarios, as well as operation at reduced magnetic field. Since a possible future power upgrade to 40MW is under discussion, the range of new capabilities achievable should be analyzed. The analysis could also be extended by taking into account the ramp-up phase, in order to provide more realistic information on the range of profiles that can be obtained at the start of burn, using localized heating, co- and/or counter-ECCD.

# Appendix A

## ITER model implemented in ASTRA

The transport model employed for ITER predictive simulations is based on the ITER-H98(y,2) empirical scaling (ELMy H-mode) [100].

### A.1 Ion densities

We take into account a D-T plasma with Ar and Be impurities, whose effective charges,  $Z_{Ar}$  and  $Z_{Be}$ , are prescribed in [124]. The impurity density distributions are assumed to be fixed fractions of the electron density:  $n_{Ar} = 0.12\% n_e$  and  $n_{Be} = 2\% n_e$ . Therefore, the total ion density is given by:  $n_i = n_D + n_T + n_\alpha + n_{Be} + n_{Ar}$ . For quasi-neutrality we have:  $n_e = \sum_i Z_i n_i = n_D + n_T + 2n_\alpha + Z_{Be} n_{Be} + Z_{Ar} n_{Ar}$ . Thus, assuming  $n_D = n_T$ , we find:

$$n_T = \frac{1}{2}(n_e - 2n_\alpha - Z_{Be} n_{Be} - Z_{Ar} n_{Ar}).$$

### A.2 Impurity radiation

In the following, we take into account the so-called “coronal approximation”, which consists in neglecting the finite population of electronically excited states of impurity ions, i.e. neglecting all collisional interactions of the electrons (and other particles) with the excited states regimes of the impurity ions. The effective ion charge is given by an average over the charge states of the ions:

$$Z_{\text{eff}} = \frac{n_D + n_T + 4n_\alpha + Z_{Be}^2 n_{Be} + Z_{Ar}^2 n_{Ar}}{n_e},$$

and in this context we have considered a flat  $Z_{\text{eff}}$  profile equal to 1.677. The total radiation power density (i.e. the total power lost by radiation) is given by the sum of the single impurities line radiation power densities, the electron Bremsstrahlung radiation power density and the electron synchrotron radiation power density.

$$P_{\text{rad}} = P_{\text{bol,Ar}} + P_{\text{bol,Be}} + P_{\text{brem}} + P_{\text{sync}}.$$

In a plasma, the free electrons are constantly losing power by Bremsstrahlung in collisions with all ion species (therefore D, T,  $\alpha$ , and impurities). The synchrotron radiation is emitted by the accelerating electrons through the magnetic field (like the electrons in a storage ring). We indicate with  $P_{\text{brem}}$  the total Bremsstrahlung radiation loss and with  $P_{\text{brem},i1}$  the Bremsstrahlung radiation loss due to impurity  $i1$  (Ar or Be) only:

$$P_{\text{brem}} = 5.06 * 10^{-5} n_e^2 \sqrt{T_e} Z_{\text{eff}}$$

$$P_{\text{br},i1} = 5.06 * 10^{-5} n_e \sqrt{T_e} n_{i1} Z_{\text{eff},i1}^2$$

To avoid accounting twice for the impurity Bremsstrahlung radiation loss, we subtract these terms to the total (bolometric) impurity radiation power density loss (as it is already taken into account in the main Bremsstrahlung term,  $P_{\text{brem}}$ ):  $P_{\text{bol},i1} = P_{\text{rad},i1} n_{i1} n_e - P_{\text{br},i1}$ .  $P_{\text{rad},i1}$  is again obtained from [124].

### A.3 NBI heating

ITER's negative NBI system consists at present of two heating and current drive injectors and one diagnostic neutral beam injector. Each H&CD injector will deliver a co-NBCD deuterium beam of 16.5 MW with energy of 1MeV [106]. The ASTRA NBI package takes into account various processes, such as the attenuation of the neutral beam during its passage through a plasma due to ionization and charge exchange, the capture and losses (including ripple losses) of the new-born ions by analysis of the ion drift trajectories, the thermalization of the suprathermal ions and their contribution to plasma heating, current drive and toroidal rotation. The latter problem requires solving the Fokker-Planck equation. The NBI routine provides various output quantities, among which the NBI driven current,  $j_{\text{NB}}$ , the beam power density absorbed by the electrons,  $P_e^{\text{NB}}$ , the



beam power density absorbed by the ions,  $P_e^{\text{NB}}$ , and source of electrons due to NBI,  $S_{\text{neBM}}$ .

## A.4 Gas puff neutrals

The ASTRA subroutine NEUT solves a kinetic equation for a neutral distribution function  $f_N$  in a slab geometry, provided such quantities as  $T_e, T_i, n_e, n_i, Z_{\text{eff}}$ , the cold and warm incoming neutrals energies and densities:

$$v \frac{\partial f_N}{\partial x} + \left( \sigma_{\text{ion}}^e n_e + \sigma_{\text{ion}}^i n_i + \sigma_{\text{cx}} n_i \right) f_N = \frac{\sqrt{3}}{2} n_i (\sigma_{\text{cx}} N + \sigma_{\text{rec}} n_e) \delta \left( v \pm \sqrt{\frac{2T_i m_i}{3}} \right),$$

where  $N$  is the density of neutral atoms of the working gas,  $\sigma_{\text{cx}}$  the charge exchange rate,  $\sigma_{\text{rec}}$  the recombination rate,  $\sigma_{\text{ion}}^e$  and  $\sigma_{\text{ion}}^i$  the rates of impact of ionization by electrons and ions, respectively. The outputs of the routine are the neutral relative density  $N(\rho)$  (normalized to the sum of the densities of the incoming neutrals) and the temperature  $T_N(\rho)$  of the neutral particles.

## A.5 Transport model (based on ITER-H98(y,2) empirical scaling)

The energy confinement time according to H98(y,2) scaling for ELMy H-mode is :

$$\tau_{E,H98(y,2)} = 0.0562 I_p^{0.93} B^{0.15} n_{19}^{0.41} R^{1.39} \kappa_a^{0.78} a^{0.58} M^{0.19} / P_{\text{input}}^{0.69},$$

while the actual energy confinement time is:

$$\tau_E(t) = \frac{3}{2} \frac{\int_V (n_e T_e + n_i T_i) dV}{P_{\text{input}}},$$

and  $W_e = 3/2 \int_V n_e T_e dV$  and  $W_i = 3/2 \int_V n_i T_i dV$  are the volume averaged electron and ion energies, respectively. The algorithm for the required energy confinement time reads:  $\tau_E(t) = \frac{W_e + W_i}{P} = HH \tau_{E,H98(y,2)}$ , and is obtained by scaling the electron heat diffusion coefficient. The ratio between the electron and ion heat diffusion coefficients is fixed (about a factor of 2), with parabolic profiles.

## A.6 Particle transport

The electron density is prescribed during the simulations, while the  $\alpha$ -particles density is determined by solving the corresponding helium transport equation, to account for the stabilizing effect of  $\alpha$ -particles in the sawtooth control studies. The  $\alpha$ -particles diffusion coefficient,  $D_\alpha$ , is here assumed equal to the electron diffusion coefficient,  $D_n$ , which one would need in order to obtain the  $n_e$  profile, consistently calculated from the various sources and sinks ( $D_\alpha = D_n$ ). The helium source is specified as:  $S_\alpha = n_D n_T \sigma_{v,DT}$ .

## A.7 Heat sources and sinks

The electron heat transport equation is solved with the following sources and sinks constituting the electron power  $P_e$ :  $P_e = P_e^{\text{NB}} + P_e^{\text{ECH}} + P_e^{\text{LH}} + P_{\text{oh}} + P_e^{\text{DT}} - P_{\text{ei}}^{\text{Coul}} - P_e^{\text{neu}} - P_{\text{rad}}$ , respectively the NBI power absorbed by the electrons, the electron heating due to ECH and LH, the ohmic heating power, the fusion power deposited to the electrons, the electron-ion heat exchange due to Coulomb collisions, the electron heat loss due to cold neutrals ionization and the radiation losses (described in A.2).

The ion heat transport equation is solved with the following sources and sinks constituting the ion power  $P_i$ :  $P_i = P_i^{\text{NB}} + P_i^{\text{DT}} + P_{\text{ei}}^{\text{Coul}} + P_i^{\text{ion}} - P_i^{\text{CX}}$ , respectively the NBI power absorbed by the ions, the fusion power deposited to the ions, the electron-ion heat exchange due to Coulomb collisions, the ion heat source due to cold neutrals ionization and the ion heat loss due to charge exchange with cold neutrals.

## A.8 Sawtooth oscillations

The sawtooth period is simulated with the Porcelli model [103], [109]. In this model, the sawtooth crash triggering conditions are determined by linear stability thresholds of the ideal and resistive internal kink. The model also provides prescriptions to determine the relaxed (post-crash) current density and pressure profiles. Once a crash condition is satisfied, the  $q$  profile is relaxed according to the Kadomtsev complete reconnection model. The density, temperature and pressure profiles are flattened within the mixing radius while keeping the total number of particles and energy conserved.

# Appendix B

## Fits for the ITER EC profiles

Gaussian fits of the  $j_{\text{eccd}}$  and  $P_{\text{EC}}$  profiles resulting from the GRAY modeling have been calculated for each of the radial deposition location,  $\rho_0$  [99]. Then, a cubic interpolation has been done for the values of the total ECCD current, the peak value and the width of the gaussian EC current density profile, as well as the peak value and the width of the gaussian EC power density profile. Specifically, the fitted gaussian distributions read (using the notation of Tables B.1-B.10):

$$j_{\text{eccd}}^{\text{1MW}} = J_{\text{cdphi}} \exp \left[ \frac{-2 (\rho_{\text{tor}} - \rho_0)}{\Delta \rho_{\text{tor\_Jphi}}} \right]^2, \quad P_{\text{EC}}^{\text{1MW}} = \frac{dP}{dV} \exp \left[ \frac{-2 (\rho_{\text{tor}} - \rho_0)}{\Delta \rho_{\text{tor\_dP}}} \right]^2.$$

The parameters arising from the interpolations have been reported in Tables B.1-B.10, for the cases of Scenarios 2 and 4-type I. The coefficients of the cubic interpolations are intended as:

$$f(\rho_{\text{tor}}) = c_0 + c_1 \rho_{\text{tor}} + c_2 \rho_{\text{tor}}^2 + c_3 \rho_{\text{tor}}^3,$$

where  $f(\rho_{\text{tor}})$  can be either of  $I_{\text{cd}}$ ,  $J_{\text{cdphi}}$ ,  $\Delta \rho_{\text{tor\_Jphi}}$ ,  $dP/dV$  or  $\Delta \rho_{\text{tor\_dP}}$ .

The values of the total ECCD and of the gaussian peaks are normalized to the total EC power. These parameters have been implemented in ASTRA, which now automatically determines the EC profiles when provided with the deposition location, the total EC power injected and the launcher used, greatly simplifying the ASTRA procedure. The tables are given below in order to keep the values used in the various simulations presented in this work. The up-to-date profiles should always be asked for from D. Farina and G. Ramponi [99] since the ITER EC design is evolving. Typical profiles are shown in Figs. 5.4–5.8.

**EPL\_USM -  $\beta=20^\circ$ , in the range:  $0.56 < \rho_{\text{tor}} < 0.8$**

$f(\rho_{\text{tor}})$	$c_0$	$c_1$	$c_2$	<b>R</b>
$I_{\text{cd}}$ (kA/MW)	3.5699	19.08	-20.74	0.99939
$J_{\text{cdphi}}$ (MA/m <sup>2</sup> /MW)	-0.0054224	0.058502	-0.050587	0.99552
$\Delta\rho_{\text{tor-Jphi}}$	0.098537	-0.18439	0.10672	0.99692
$dP/dV$ (MW/m <sup>3</sup> /MW)	0.018076	0.046578	-0.018822	0.98209
$\Delta\rho_{\text{tor-dP}}$	0.095212	-0.17476	0.10009	0.99694

**EPL\_USM -  $\beta=20^\circ$ , in the range:  $0.3 < \rho_{\text{tor}} < 0.56$**

$f(\rho_{\text{tor}})$	$c_0$	$c_1$	$c_2$	<b>R</b>
$I_{\text{cd}}$ (kA/MW)	16.015	-27.38	22.478	0.99987
$J_{\text{cdphi}}$ (MA/m <sup>2</sup> /MW)	0.034876	-0.093346	0.091762	0.99963
$\Delta\rho_{\text{tor-Jphi}}$	0.094208	-0.17017	0.095565	0.99923
$dP/dV$ (MW/m <sup>3</sup> /MW)	0.069263	-0.1535	0.17407	0.99806
$\Delta\rho_{\text{tor-dP}}$	0.094169	-0.17114	0.097455	0.99917

Figure B.1: GRAY-calculated fits for the EC profiles. Case of Scenario 2, Upper Steering Mirror of the Upper Launcher [99].

EOB2\_ref

EPL\_LSM -  $\beta=18^\circ$ , in the range range:  $0.55 < \rho_{\text{tor}} < 0.88$

$f(\rho_{\text{tor}})$	$c_0$	$c_1$	$c_2$	<b>R</b>
$I_{\text{cd}}$ (kA/MW)	1.5014	16.891	-15.964	0.99983
$J_{\text{cda}}$ (MA/m <sup>2</sup> /MW)	-0.029824	0.10741	-0.062832	0.99759
$\Delta\rho_{\text{tor-cda}}$	0.11529	-0.23386	0.12777	0.99868
$dP/dV$ (MW/m <sup>3</sup> /MW)	0.015764	-0.020612	0.12877	0.99921
$\Delta\rho_{\text{tor-dP}}$	0.11398	-0.23075	0.12615	0.99853

EPL\_LSM -  $\beta=18^\circ$ , in the range range:  $0.88 < \rho_{\text{tor}} < 0.96$

$f(\rho_{\text{tor}})$	$c_0$	$c_1$	$c_2$	<b>R</b>
$I_{\text{cd}}$ (kA/MW)	29.517	-46.167	19.472	0.99851
$J_{\text{cda}}$ (MA/m <sup>2</sup> /MW)	-0.50566	1.1208	-0.60065	0.98171
$\Delta\rho_{\text{tor-cda}}$	0.76925	-1.6562	0.89959	0.95097
$dP/dV$ (MW/m <sup>3</sup> /MW)	-2.9517	6.1808	-3.088	0.99885
$\Delta\rho_{\text{tor-dP}}$	0.75831	-1.6301	0.88411	0.94443

Figure B.2: GRAY-calculated fits for the EC profiles. Case of Scenario 2, Lower Steering Mirror of the Upper Launcher [99].

**EL\_TOP**  
**CNTR-CD in the radial range:  $0.12 \leq \rho_{\text{tor}} \leq 0.15$**

$f(\rho_{\text{tor}})$	$c_0$	$c_1$	$c_2$	$c_3$	<b>R</b>
$dP/dV(\text{MWm}^{-3}/\text{MW})$	0.20421	-1.118	0	0	1
$\Delta\rho_{\text{tor}_dP}$	-0.047255	0.95127	0	0	1
$I_{cd} (\text{kA}/\text{MW})$	-16.009	-71.921	0	0	1
$J_{cdphi} (\text{MA m}^{-2}/\text{MW})$	-0.19538	1.0346	0	0	1
$\Delta\rho_{\text{tor}_Jphi}$	-0.046875	0.94686	0	0	1

**EL\_TOP**  
**CNTR-CD in the radial range:  $0.15 \leq \rho_{\text{tor}} \leq 0.4$**

$f(\rho_{\text{tor}})$	$c_0$	$c_1$	$c_2$	$c_3$	<b>R</b>
$dP/dV(\text{MWm}^{-3}/\text{MW})$	0.12062	-0.84717	2.3474	-2.309	0.9992
$\Delta\rho_{\text{tor}_dP}$	-0.15292	3.0095	-11.279	14.308	0.99691
$I_{cd} (\text{kA}/\text{MW})$	-15.92	-121.18	354.98	-167.41	0.99997
$J_{cdphi} (\text{MA m}^{-2}/\text{MW})$	-0.11595	0.72458	-1.7875	1.64	0.99932
$\Delta\rho_{\text{tor}_Jphi}$	-0.12793	2.6709	-9.85117	12.409	0.99854

Figure B.3: *GRAY-calculated fits for the EC profiles. Case of Scenario 2, Top Steering Mirror of the Equatorial Launcher [99].*

**EL\_MID**  
**Co-CD in the radial range:  $0.001 \leq \rho_{\text{tor}} \leq 0.013$**

$f(\rho_{\text{tor}})$	$c_0$	$c_1$	$c_2$	$c_3$	<b>R</b>
$dP/dV(\text{MWm}^{-3}/\text{MW})$	0.33328	-11.797	0	0	1
$\Delta\rho_{\text{tor}_dP}$	-0.02503	7.8391	0	0	1
$I_{cd}(\text{kA}/\text{MW})$	22.889	266.56	0	0	1
$J_{cdphi}(\text{MA m}^{-2}/\text{MW})$	0.37288	-12.774	0	0	1
$\Delta\rho_{\text{tor}_Jphi}$	-0.010239	6.6161	0	0	1

**EL\_MID**  
**Co-CD in the radial range:  $0.013 \leq \rho_{\text{tor}} \leq 0.16$**

$f(\rho_{\text{tor}})$	$c_0$	$c_1$	$c_2$	$c_3$	<b>R</b>
$dP/dV(\text{MWm}^{-3}/\text{MW})$	0.20937	-2.19	6.8826	0	1
$\Delta\rho_{\text{tor}_dP}$	0.071815	0.27036	-0.66731	0	1
$I_{cd}(\text{kA}/\text{MW})$	26.012	22.873	-51.071	0	1
$J_{cdphi}(\text{MA m}^{-2}/\text{MW})$	0.24044	-2.5127	7.9032	0	1
$\Delta\rho_{\text{tor}_Jphi}$	0.070762	0.28831	-0.77067	0	1

**EL\_MID**  
**Co-CD in the radial range:  $0.16 \leq \rho_{\text{tor}} \leq 0.41$**

$f(\rho_{\text{tor}})$	$c_0$	$c_1$	$c_2$	$c_3$	<b>R</b>
$dP/dV(\text{MWm}^{-3}/\text{MW})$	0.089122	-0.51203	1.2544	-1.1877	0.99988
$\Delta\rho_{\text{tor}_dP}$	-0.024384	1.4902	-5.8175	8.1377	0.99925
$I_{cd}(\text{kA}/\text{MW})$	23.944	53.453	-157.96	-25.246	0.99993
$J_{cdphi}(\text{MA m}^{-2}/\text{MW})$	0.10786	-0.61401	1.4095	-1.2646	0.99972
$\Delta\rho_{\text{tor}_Jphi}$	-0.022839	1.4275	-5.433	7.4717	0.99985

Figure B.4: GRAY-calculated fits for the EC profiles. Case of Scenario 2, Mid Steering Mirror of the Equatorial Launcher [99].

**EL\_LOW**  
**Co-CD in the radial range:  $0.080 \leq \rho_{\text{tor}} \leq 0.095$**

$f(\rho_{\text{tor}})$	$c_0$	$c_1$	$c_2$	$c_3$	<b>R</b>
$dP/dV(\text{MWm}^{-3}/\text{MW})$	0.4078	-3.6857	0	0	1
$\Delta\rho_{\text{tor\_dP}}$	-0.040812	1.4653	0	0	1
$I_{\text{cd}}(\text{kA}/\text{MW})$	9.9586	176.49	0	0	1
$J_{\text{cdphi}}(\text{MA m}^{-2}/\text{MW})$	0.39096	-3.4412	0	0	1
$\Delta\rho_{\text{tor\_Jphi}}$	-0.039855	1.4567	0	0	1

**EL\_LOW**  
**Co-CD in the radial range:  $0.095 \leq \rho_{\text{tor}} \leq 0.4$**

$f(\rho_{\text{tor}})$	$c_0$	$c_1$	$c_2$	$c_3$	<b>R</b>
$dP/dV(\text{MWm}^{-3}/\text{MW})$	0.12747	-0.98464	2.983	-3.1549	0.99844
$\Delta\rho_{\text{tor\_dP}}$	0.037792	0.95191	-4.2013	6.5735	0.99477
$I_{\text{cd}}(\text{kA}/\text{MW})$	21.827	70.545	-205.93	19.14	0.99997
$J_{\text{cdphi}}(\text{MA m}^{-2}/\text{MW})$	0.13298	-0.95412	2.6971	-2.7471	0.99864
$\Delta\rho_{\text{tor\_Jphi}}$	0.04405	0.84432	-3.6635	5.7246	0.99484

Figure B.5: *GRAY-calculated fits for the EC profiles. Case of Scenario 2, Low Steering Mirror of the Equatorial Launcher [99].*



**EPL\_USM ( $\beta=20^\circ$ ,  $\alpha=44^\circ$ --- $68^\circ$ ), in the radial range:  $0.45 \leq \rho_{\text{tor}} \leq 0.85$**

$f(\rho_{\text{tor}})$	$c_0$	$c_1$	$c_2$	$c_3$	<b>R</b>
$I_{\text{cd}}$ (kA/MW)	-70.76	426.11	-662.64	312.74	0.9972
$J_{\text{cd}}$ (MA/m <sup>2</sup> /MW)	0.13099	-0.26953	0.15114	-0.0096177	0.99658
$\Delta\rho_{\text{tor-Jcd}}$	0.026006	-0.088878	0.26411	-0.18124	0.94676
$dP/dV$ (MW/m <sup>3</sup> /MW)	0.31172	-0.96416	1.107	-0.42614	0.99252
$\Delta\rho_{\text{tor-dP}}$	0.016909	-0.045303	0.19586	-0.14621	0.95366

Figure B.6: GRAY-calculated fits for the EC profiles. Case of Scenario 4, Upper Steering Mirror of the Upper Launcher [99].

**EPL\_LSM ( $\beta=18^\circ$ ,  $\alpha=34^\circ$ --- $58^\circ$ ) in the radial range range:  $0.58 \leq \rho_{\text{tor}} \leq 0.86$**

$f(\rho_{\text{tor}})$	$c_0$	$c_1$	$c_2$	<b>R</b>
$I_{\text{cd}}$ (kA/MW)	41.079	-62.388	22.66	0.99685
$J_{\text{cd}}$ (MA/m <sup>2</sup> /MW)	0.14354	-0.27123	0.13421	0.99749
$\Delta\rho_{\text{tor-Jcd}}$	0.010474	0.031769	-0.031069	0.98655
$dP/dV$ (MW/m <sup>3</sup> /MW)	0.19351	-0.3589	0.2367	0.94718
$\Delta\rho_{\text{tor-dP}}$	0.010699	0.029547	-0.028177	0.97988

Figure B.7: GRAY-calculated fits for the EC profiles. Case of Scenario 4, Lower Steering Mirror of the Upper Launcher [99].

**EL\_TOP**  
**CNTR-CD in the radial range:  $0.13 \leq \rho_{\text{tor}} \leq 0.16$**

$f(\rho_{\text{tor}})$	$c_0$	$c_1$	$c_2$	$c_3$	<b>R</b>
$dP/dV(\text{MWm}^{-3}/\text{MW})$	0.21915	-1.1508	0	0	1
$\Delta\rho_{\text{tor\_dP}}$	-0.1507	1.5556	0	0	1
$I_{\text{cd}}(\text{kA}/\text{MW})$	-25.785	-66.221	0	0	1
$J_{\text{cdphi}}(\text{MA m}^{-2}/\text{MW})$	-0.35162	1.843	0	0	1
$\Delta\rho_{\text{tor\_Jphi}}$	-0.15127	1.5576	0	0	1

**EL\_TOP**  
**CNTR-CD in the radial range:  $0.16 \leq \rho_{\text{tor}} \leq 0.43$**

$f(\rho_{\text{tor}})$	$c_0$	$c_1$	$c_2$	$c_3$	<b>R</b>
$dP/dV(\text{MWm}^{-3}/\text{MW})$	0.10762	-0.75409	1.964	-1.7689	0.99902
$\Delta\rho_{\text{tor\_dP}}$	-0.21319	3.1833	-9.2389	10.261	0.9994
$I_{\text{cd}}(\text{kA}/\text{MW})$	-34.485	4.4808	-189.44	480.69	0.99973
$J_{\text{cdphi}}(\text{MA m}^{-2}/\text{MW})$	-0.17443	1.2206	-3.1877	2.9188	0.99902
$\Delta\rho_{\text{tor\_Jphi}}$	-0.19857	3.0573	-9.0075	10.197	0.99966

Figure B.8: GRAY-calculated fits for the EC profiles. Case of Scenario 4, Top Steering Mirror of the Equatorial Launcher [99].

**EL\_MID**  
**Co-CD in the radial range:  $0.014 \leq \rho_{\text{tor}} \leq 0.03$**

$f(\rho_{\text{tor}})$	$c_0$	$c_1$	$c_2$	$c_3$	<b>R</b>
$dP/dV(\text{MWm}^{-3}/\text{MW})$	0.32544	-8.2559	0	0	1
$\Delta\rho_{\text{tor}_dP}$	-0.0016263	4.2588	0	0	1
$I_{cd}(\text{kA}/\text{MW})$	34.207	100.57	0	0	1
$J_{cdphi}(\text{MA m}^{-2}/\text{MW})$	0.58298	-14.986	0	0	1
$\Delta\rho_{\text{tor}_Jphi}$	-0.0059672	4.439	0	0	1

**EL\_MID**  
**Co-CD in the radial range:  $0.03 \leq \rho_{\text{tor}} \leq 0.4$**

$f(\rho_{\text{tor}})$	$c_0$	$c_1$	$c_2$	$c_3$	<b>R</b>
$dP/dV(\text{MWm}^{-3}/\text{MW})$	0.075493	-0.57591	1.7702	-1.9123	0.99958
$\Delta\rho_{\text{tor}_dP}$	0.088166	1.7609	-8.6201	13.17	0.99192
$I_{cd}(\text{kA}/\text{MW})$	37.887	-18.898	202.57	-485.75	0.99768
$J_{cdphi}(\text{MA m}^{-2}/\text{MW})$	0.12589	-0.92539	2.7449	-2.9212	0.99967
$\Delta\rho_{\text{tor}_Jphi}$	0.096201	1.5194	-7.4552	11.53	0.99322

Figure B.9: *GRAY-calculated fits for the EC profiles. Case of Scenario 4, Mid Steering Mirror of the Equatorial Launcher [99].*

**EL\_LOW**  
**Co-CD in the radial range:  $0.06 \leq \rho_{\text{tor}} \leq 0.1$**

$f(\rho_{\text{tor}})$	$c_0$	$c_1$	$c_2$	$c_3$	<b>R</b>
$dP/dV(\text{MWm}^{-3}/\text{MW})$	0.25934	-2.2967	0	0	1
$\Delta\rho_{\text{tor}_dP}$	-0.010784	1.5602	0	0	1
$I_{cd}(\text{kA}/\text{MW})$	32.428	44.258	0	0	1
$J_{cd\phi}(\text{MA m}^{-2}/\text{MW})$	0.38219	-2.9661	0	0	1
$\Delta\rho_{\text{tor}_J\phi}$	0.011035	1.2046	0	0	1

**EL\_LOW**  
**Co-CD in the radial range:  $\leq \rho_{\text{tor}} \leq$**

$f(\rho_{\text{tor}})$	$c_0$	$c_1$	$c_2$	$c_3$	<b>R</b>
$dP/dV(\text{MWm}^{-3}/\text{MW})$	0.086624	-0.64125	1.8157	-1.7731	0.99886
$\Delta\rho_{\text{tor}_dP}$	0.072255	0.93356	-2.9295	4.1889	0.99882
$I_{cd}(\text{kA}/\text{MW})$	36.229	0.23216	114.72	-342.25	0.99995
$J_{cd\phi}(\text{MA m}^{-2}/\text{MW})$	0.16194	-1.2306	3.5181	-3.479	0.99866
$\Delta\rho_{\text{tor}_J\phi}$	0.07776	0.79845	-2.4522	3.6902	0.99936

Figure B.10: GRAY-calculated fits for the EC profiles. Case of Scenario 4, Low Steering Mirror of the Equatorial Launcher [99].

# Bibliography

- [1] <http://www.worldenergy.com/>.
- [2] <http://www-fusion-magnetique.cea.fr/>.
- [3] <http://www.iea.org/>.
- [4] J. D. Lawson, Proc. of the Physical Society, Section B **70**, 6 (1957).
- [5] <http://www.iter.org/>.
- [6] E. J. Doyle *et al.*, Nucl. Fusion **47**, S18 (2007).
- [7] R. King, C. D. Challis, and D. Ciric, Fusion Engineering and Design **74**, 455 (2005).
- [8] M. E. Austin *et al.*, Phys. Plasmas **13**, 082502 (2006).
- [9] R. C. Wolf *et al.*, Plasma Phys. Control. Fusion **41**, B93 (1999).
- [10] M. Kuriyama *et al.*, J. Nucl. Sci. Technol. **35**, 739 (1998).
- [11] C. S. Liu and V. S. Chan, Phys. Scripta **T2/1**, 158 (1982).
- [12] N. Fisch and A. Boozer, Phys. Rev. Lett. **45**, 720 (1980).
- [13] N. Fisch, Plasma Phys. Control. Fusion **35**, A91 (1993).
- [14] J. G. Cordey, Plasma Phys. Control. Fusion **26**, 123 (1984).
- [15] A. Peeters, Plasma Phys. Control. Fusion **42**, B231 (2000).
- [16] S. Coda *et al.*, in Proc. 34th EPS Conference on Plasma Phys. and Control. Fusion (Warsaw, Poland), European Conference Abstracts (ECA) (Petit Lancy, Switzerland, 2007), Vol. 31F, D-1.008.

- [17] S. Coda *et al.*, in *Proc. of the 22nd IAEA Fusion Energy Conference, Geneva, Switzerland* (IAEA, Vienna, 2008), Vol. EX/2-3.
- [18] G. V. Pereverzev, Max Planck - IPP Report **5/42**, (1991).
- [19] S. Cirant *et al.*, Nucl. Fusion **46**, 500 (2006).
- [20] S. Coda, Nucl. Fusion **47**, 714 (2007).
- [21] O. Sauter *et al.*, Phys. Rev. Lett. **94**, 105002 (2005).
- [22] M. Henderson *et al.*, Fusion Engineering and Design **82**, 454 (2007).
- [23] S. von Goeler, W. Stodiek, and N. Sauthoff, Phys. Rev. Lett. **33**, 1201 (1974).
- [24] O. Sauter *et al.*, Phys. Plasmas **4**, 1654 (1997).
- [25] E. Joffrin *et al.*, Nucl. Fusion **43**, 1167 (2003).
- [26] J. Wesson, *Tokamaks* (Oxford University Press, 3rd edition, 2004).
- [27] F. M. Levinton *et al.*, Phys. Rev. Lett. **63**, 2060 (1989).
- [28] M. R. Siegrist, N. Hawkes, and H. Weisen, Rev. Sci. Instrum. **75**, 3465 (2004).
- [29] H. R. Koslowski and H. Soltwisch, Fusion Engineering and Design **34-35**, 143 (1997).
- [30] P. Blanchard, R. Behn, H. Weisen, and A. Zhuchkova, in *Proc. 16th Topical Conference on High-Temperature Plasma Diagnostics* (Williamsburg, Virginia, 2006).
- [31] M. Anton *et al.*, Plasma Phys. Control. Fusion **38**, 1849 (1996).
- [32] A. Sushkov *et al.*, in *Proc. 29th Conference on Plasma Phys. and Control. Fusion (Montreux, Switzerland), European Conference Abstracts (ECA)* (Petit Lancy, Switzerland, 2002), Vol. 26B, P-4.118.
- [33] G. Turri *et al.*, in *Proc. 33rd EPS Conference on Plasma Phys. and Control. Fusion (Roma, Italy), European Conference Abstracts (ECA)* (Petit Lancy, Switzerland, 2006), Vol. 30I, P-1.148.
- [34] L. L. Lao *et al.*, Nucl. Fusion **30**, 1035 (1990).

- [35] F. Hofmann and G. Tonetti, Nucl. Fusion **28**, 1871 (1988).
- [36] V. D. Shafranov, Rev. Plasma Phys. **2**, 103 (1966).
- [37] J.-M. Moret *et al.*, Phys. Rev. Lett. **79**, 2057 (1997).
- [38] J. B. Lister *et al.*, Fusion Engineering and design **74**, 633 (2005).
- [39] L. E. Zakharov and A. Pletzer, Phys. Plasmas **6**, 4693 (1999).
- [40] A. A. Ivanov, R. R. Khayrutdinov, S. Y. Medvedev, and Y. Y. Poshekhonov, *in Proc. 32nd EPS Conference on Plasma Phys. and Control. Fusion (Tarragona, Spain), European Conference Abstracts (ECA) (Petit Lancy, Switzerland, 2005), Vol. 29C, P-5.063.*
- [41] S. C. Jardin, N. Pomphrey, and J. L. DeLucia, J. Comput. Phys. **66**, 481 (1986).
- [42] L. L. Lao *et al.*, Nucl. Fusion **25**, 1421 (1985).
- [43] H. Lütjens, A. Bondeson, and O. Sauter, Comput. Phys. Commun. **97**, 219 (1996).
- [44] O. Sauter, C. Angioni, and Y. Lin-Liu, Phys. Plasmas **6**, 2834 (1999).
- [45] O. Sauter, C. Angioni, and Y. Lin-Liu, Phys. Plasmas **9**, 5140 (2002).
- [46] R. W. Harvey and M. G. McCoy, *in Proc. IAEA TCM on Advances in Simulation and Modeling of Thermonuclear Plasmas, Montreal, Canada (IAEA, Vienna, 1992), p. 527.*
- [47] G. R. Smith, *in Proc. 9th Joint Workshop on ECE and ECRH, Borrego Springs, CA (World Scientific, Singapore, 1995), p. 651.*
- [48] R. W. Harvey, O. Sauter, R. Prater, and P. Nikkola, Phys. Rev. Lett. **88**, 205001 (2002).
- [49] P. Nikkola *et al.*, Nucl. Fusion **43**, 1343 (2003).
- [50] E. Fable *et al.*, Plasma Phys. Control. Fusion **48**, 1271 (2006).
- [51] V. Basiuk *et al.*, Nucl. Fusion **43**, 822 (2003).

- [52] D. Boucher, Ph.D. thesis, Ecole Polytechnique de Paris, 1992.
- [53] G. Cennachi and A. Taroni, JET Report JET-IR(88)03 (1988).
- [54] C. E. Singer *et al.*, Comput. Phys. Commun. **49**, 275 (1988).
- [55] C. Angioni, Ph.D. thesis, EPFL, no. 2469, 2001.
- [56] J. W. Connor *et al.*, Nucl. Fusion **44**, R1 (2004).
- [57] R. C. Wolf, Plasma Phys. Control. Fusion **45**, R1 (2003).
- [58] X. Litaudon and the Equipe Tore Supra, Plasma Phys. Control. Fusion **38**, A251 (1996).
- [59] G. T. Hoang *et al.*, Phys. Rev. Lett. **84**, 4593 (2000).
- [60] C. Gormezano *et al.*, Phys. Rev. Lett. **80**, 5544 (1998).
- [61] M. A. Henderson *et al.*, Phys. Rev. Lett. **93**, 215001 (2004).
- [62] F. Hofmann *et al.*, Plasma Phys. Control. Fusion B277 (1994).
- [63] T. P. Goodman *et al.*, in *in Proc. 19th Symp. on Fusion Technology (Lisbon, Portugal, 1996)*, edited by C. Varandas and F. Serra (North-Holland, Amsterdam, 1997), p. 565.
- [64] J.-P. Hogge, S. Alberti, L. Porte, and G. Arnoux, Nucl. Fusion **49**, 1353 (2003).
- [65] T. P. Goodman, Plasma Phys. Control. Fusion **47**, B107 (2005).
- [66] S. Coda *et al.*, Phys. Plasmas **12**, 056124 (2005).
- [67] O. Sauter *et al.*, Phys. Rev. Lett. **84**, 3322 (2000).
- [68] O. Sauter *et al.*, in *Proc. 29th EPS Conference on Plasma Phys. and Control. Fusion (Montreux, Switzerland), European Conference Abstracts (ECA)* (Petit Lancy, Switzerland, 2002), Vol. 26B, P-2.087.
- [69] A. Bottino, O. Sauter, Y. Camenen, and E. Fable, Plasma Phys. Control. Fusion **48**, 215 (2006).



- [70] P. H. Rebut *et al.*, in *Proc. 12th Int. Conf. on Plasma Phys. and Controlled Nuclear Fusion Research, Nice* (IAEA, Vienna, 1988), p. 191.
- [71] J. Candy, R. E. Waltz, and M. N. Rosenbluth, *Phys. Plasmas* **11**, 1879 (2004).
- [72] O. Sauter *et al.*, *Phys. Plasmas* **8**, 2199 (2001).
- [73] T. A. Casper, R. J. Jayakumar, L. D. Pearlstein, and L. L. LoDestro, in *Proc. 31th EPS Conference on Plasma Phys. and Control. Fusion (London, UK), European Conference Abstracts (ECA)* (Petit Lancy, Switzerland, 2004), Vol. 28G, P-2.178.
- [74] N. Hawkes *et al.*, *Phys. Rev. Lett.* **87**, 115001 (2001).
- [75] B. C. Stratton *et al.*, *Plasma Phys. Control. Fusion* **44**, 1127 (2002).
- [76] T. Fujita *et al.*, *Phys. Rev. Lett.* **87**, 245001 (2001).
- [77] A. V. Chankin, V. S. Mukhovatov, T. Fujita, and Y. Miura, *Plasma Phys. Control. Fusion* **45**, 323 (2003).
- [78] Y. I. Pozdnyakov, *Phys. Plasmas* **12**, 084503 (2005).
- [79] A. A. Martynov, S. Y. Medvedev, and L. Villard, *Phys. Rev. Lett.* **91**, (2003).
- [80] P. Mantica *et al.*, *Phys. Rev. Lett.* **96**, 095002 (2006).
- [81] C. Zucca *et al.*, *Plasma Phys. Control. Fusion* **51**, 015002 (2009).
- [82] J. E. Kinsey, R. E. Waltz, and J. Candy, *Phys. Plasmas* **13**, 022305 (2006).
- [83] J. Candy and R. E. Waltz, *J. Comput. Phys.* **186**, 545 (2003).
- [84] K. Ikeda *et al.*, *Nucl. Fusion* **47**, S1 (2007).
- [85] <http://www.efda.org/>.
- [86] C. Gormezano *et al.*, *Nucl. Fusion* **47**, S285 (2007).
- [87] P. U. Lamalle *et al.*, *Fusion Engineering and Design* **74**, 359 (2005).
- [88] G. Ramponi *et al.*, *Nucl. Fusion* **48**, 054012 (2008).

- [89] H. Zohm *et al.*, Nucl. Fusion **39**, 577 (1999).
- [90] T. C. Hender *et al.*, Nucl. Fusion **47**, S128 (2007).
- [91] O. Sauter *et al.*, Phys. Rev. Lett. **88**, 105001 (2002).
- [92] H. Zohm *et al.*, Journal of Physics: Conference Series **25**, 234 (2005).
- [93] M. Henderson *et al.*, in *Proc. of the 21st IAEA Fusion Energy Conference, Chengdu, China* (IAEA, Vienna, 2006), Vol. IT/P2-15.
- [94] S. Guenter *et al.*, Nucl. Fusion **44**, 524 (2004).
- [95] T. A. Casper *et al.*, Nucl. Fusion **47**, 825 (2007).
- [96] M. E. Puiatti *et al.*, Phys. Plasmas **13**, 042501 (2006).
- [97] R. Neu *et al.*, Plasma Phys. Control. Fusion **44**, 811 (2002).
- [98] R. Goldston, J. Fusion Energy **21**, 61 (2002).
- [99] D. Farina and G. Ramponi, CNR-Milano, private communication, 2008.
- [100] D. J. Campbell, Plasma Phys. Control. Fusion **41**, B381 (1999).
- [101] A. R. Polevoi *et al.*, in *Proc. of the 19th IAEA Fusion Energy Conference, Lyon, France* (IAEA, Vienna, 2002), Vol. CT/P-08.
- [102] A. R. Polevoi, M. Shimada, and V. Mukhovatov, Plasma Phys. Control. Fusion **48**, A449 (2006).
- [103] F. Porcelli, D. Boucher, and M. N. Rosenbluth, Plasma Phys. Control. Fusion **38**, 2163 (1996).
- [104] C. M. Roach *et al.*, Nucl. Fusion **48**, 125001 (2008).
- [105] E. Joffrin, Plasma Phys. Control. Fusion **49**, B629 (2007).
- [106] Technical Basis for the ITER Final Design - ITER EDA Documentation Series (IAEA, Vienna) no. 24, 2002.
- [107] X. Litaudon *et al.*, Plasma Phys. Control. Fusion **46**, A19 (2004).

- [108] D. Farina, *Fusion Science and Technology* **52**, 154 (2007).
- [109] O. Sauter *et al.*, in *Proc. Joint Varenna-Lausanne International Workshop on Theory of Fusion Plasmas (Varenna, Italy)*, edited by J. W. Connor, E. Sindoni, and J. Vaclavik (Società Italiana di Fisica, Ed. Compositori, Bologna, 1998), p. 403.
- [110] C. Angioni, T. P. Goodman, M. A. Henderson, and O. Sauter, *Nucl. Fusion* **43**, 455 (2003).
- [111] A. Mück *et al.*, *Plasma Phys. Control. Fusion* **47**, 1633 (2005).
- [112] O. Sauter and H. Zohm, in *Proc. 32nd EPS Conference on Plasma Phys. and Control. Fusion (Tarragona, Spain), European Conference Abstracts (ECA)* (Petit Lancy, Switzerland, 2005), Vol. 29C, P-2.059.
- [113] R. W. Harvey and F. V. Perkins, *Nucl. Fusion* **41**, 1847 (2001).
- [114] A. Merkulov *et al.*, in *Proc. Joint Varenna-Lausanne International Workshop on Theory of Fusion Plasmas (Varenna, Italy)*, edited by J. W. Connor, O. Sauter, and E. Sindoni (Società Italiana di Fisica, Ed. Compositori, Bologna, 2004), p. 279.
- [115] H. Weisen *et al.*, *Plasma Phys. Control. Fusion* **48**, A457 (2006).
- [116] T. A. Casper *et al.*, in *Proc. 29th EPS Conference on Plasma Phys. and Control. Fusion (Montreux, Switzerland), European Conference Abstracts (ECA)* (Petit Lancy, Switzerland, 2002), Vol. 26B, P-2.065.
- [117] C. Angioni *et al.*, *Phys. Rev. Lett.* **90**, 205003 (2003).
- [118] H. Weisen *et al.*, *Nucl. Fusion* **45**, L1 (2005).
- [119] C. Angioni *et al.*, *Nucl. Fusion* **47**, 1326 (2007).
- [120] C. Angioni *et al.*, *Nucl. Fusion* **44**, 827 (2004).
- [121] H. Weisen, I. Furno, and the TCV team, *Nucl. Fusion* **41**, 1227 (2001).
- [122] S. Cirant *et al.*, *Proc. of the 21st IAEA Fusion Energy Conference, Chengdu, China* (IAEA, Vienna, 2006), Vol. EX/P3-3.

[123] C. Zucca *et al.*, Theory of Fusion Plasmas, AIP Conference Proceedings **1069**, 361 (2008).

[124] D. E. Post and R. V. Jensen, Atomic Data and Nuclear Tables **20**, 397 (1977).

# Acknowledgements

I am extremely grateful to anyone who helped me out during my work on the present thesis, which means so much to me. First of all, to my thesis supervisor, Dr. Olivier Sauter: your extraordinary scientific and human qualities are going to be an enduring example for me, no matter where life will take me. Merci, merci de tout mon cœur !

I would like to acknowledge the great CRPP team - direction, secretaries, technicians, and scientific staff. Particularly, I feel very lucky to have had the opportunity of discussing and learning from Drs. Mark Henderson, Tim Goodman, Stefano Coda, Stefano Alberti, Roland Behn, Gabriella Ramponi, Gabriella Saibene, Daniela Farina, Alexei Polevoi, and Sante Cirant. Special thanks to all the youngsters who spent many working and partying hours with me: the now doctors Alberto, Paolo, Sergi, Yann, Gilles, Marco; the soon-to-be doctors Ale & Ale, Barbora, Martin, Xavier, Janos, Nicolas; the one-day doctors Mattia, Francesco, Federico; and the engineers Anna, Francisco, Andrés. “Arigatō”, Séb, for sharing a lot more than the office for the past 4 years.

I would like to dedicate this thesis to our family friend Sergio Scarsi: this is likely the closest I can get to the revolutionary physics discovery I once promised to name after you! The warmest thank you’s to my best friends, partners in crime and Swiss family, Alice and GP, but also Riccino, Elaine, Izzy, Chants, Crissy, Fede, Andre, Ettore, Carlos, Rui, Sophie, Jo, Vero, Ed, Tyler, Ele, and too many others to be all listed. The blame is yours for persuading me to stay in Switzerland...

Last, but certainly not least, I will never thank enough my parents and sister, for supporting me even when my decisions were not fully shared, for understanding me even when I myself felt a bit lost, and for plenty of other reasons that I do not know how to explain here.

This work was supported in part by the Swiss National Science Foundation and by a Fusion for Energy (f4e) contract.

# Curriculum Vitae

**Costanza ZUCCA**

Place and date of birth: Genoa (Italy), October 5<sup>th</sup> 1980.

- 06/2004 – 01/2009:** PhD in Plasma Physics  
at the Centre des Recherches en Physique des Plasmas,  
Ecole Polytechnique Fédérale de Lausanne (Switzerland).
- 08/2002 – 12/2003:** MSc in Physics at Uppsala University (Sweden).
- 10/1999 – 08/2002:** BSc in Physics at Genoa University (Italy),  
110/110 summa cum laude.

# List of publications

## Refereed Publications

- 15) F. Piras *et al.*, including **C. Zucca**,  
*Snowflake divertor plasmas on TCV*,  
Plasma Phys. Control. Fusion **51** (2009) 055009.
- 14) **C. Zucca** *et al.*,  
*Current density evolution during electron internal transport barrier discharges in TCV*,  
Plasma Phys. Control. Fusion **51** (2009) 015002.
- 13) V. S. Udintsev *et al.*, including **C. Zucca**,  
*Global plasma oscillations in electron internal transport barriers in TCV*,  
Plasma Phys. Control. Fus. **50**, 124052 (2008).
- 12) A. Fasoli *et al.*, including **C. Zucca**,  
*Overview of physics research on the TCV Tokamak*,  
Proc. 22<sup>st</sup> IAEA Fusion Energy Conference, Geneva, Switzerland (IAEA, Vienna, 2008),  
OV/1-1.
- 11) G. Turri *et al.*, including **C. Zucca**,  
*The role of MHD in the sustainment of electron internal transport barriers and H-mode in TCV*,  
J. Phys.: Conf. Ser. **123** (2008) 012038.
- 10) M. A. Henderson *et al.*, including **C. Zucca**,  
*Overview of the ITER EC upper launcher*,  
Nucl. Fusion **48** (2008) 054013.

- 9) G. Ramponi *et al.*, including **C. Zucca**,  
*Physics analysis of the ITER ECW system for an optimized performance*,  
Nucl. Fusion **48** (2008) 054012.
- 8) S. Coda *et al.*, including **C. Zucca** and the TCV team,  
*The physics of electron internal transport barriers in the TCV tokamak*,  
Nucl. Fusion **47** (2007) 714-720.
- 7) **C. Zucca** *et al.*,  
*Nonlinear dynamics of flute modes and self-organization phenomena in turbulent magnetized plasma*,  
Plasma Phys. Contr. Fusion **49** (2007) A249-A258.
- 6) E. Fable *et al.*, including **C. Zucca**,  
*Inward thermodiffusive particle pinch in electron internal transport barriers in TCV*,  
Plasma Phys. Contr. Fusion **48** 1271-1283 (2006).
- 5) A. Fasoli *et al.*, including **C. Zucca**,  
*Overview of TCV results*,  
Nucl. Fusion **48** 034001 (2006).
- 4) S. Coda, *et al.*, including **C. Zucca**,  
*High-bootstrap, noninductively sustained electron internal transport barriers in the tokamak configuration variable*,  
Phys. Plasmas **12**, 056124 (2005).
- 3) O. Sauter *et al.*, including **C. Zucca**,  
*Inductive current density perturbations to probe electron internal transport barriers in tokamaks*,  
Phys. Rev. Lett. **94**, 105002 (2005).
- 2) T. P. Goodman *et al.*, including **C. Zucca**,  
*Safety factor profile requirements for electron ITB formation in TCV*,



Plasma Phys. Contr. Fusion **47**, B107-120 (2005).

1) M. A. Henderson *et al.*, including **C. Zucca**,

*Rapid electron internal transport barrier formation during magnetic shear reversal in fully non-inductive TCV discharges,*

Nucl. Fusion **45**, 1642-1649 (2005).

## First author conference contributions

4) **C. Zucca** *et al.*,

*Safety-factor profile tailoring by improved EC system for sawtooth control and reverse shear scenarios in ITER,*

Theory of Fusion Plasmas, AIP Conference Proceedings **1069** (2008) 361-367.

3) **C. Zucca** *et al.*,

*Studies of electron transport and current diffusion in switched ECCD experiments on TCV,*

Proc. 33<sup>rd</sup> EPS Conference on Plasma Phys. and Control. Fusion (Rome, Italy), European Conference Abstracts (ECA) (Petit Lancy, Switzerland, 2006), Vol. **30I** (2006) P-1.150.

2) **C. Zucca** *et al.*,

*Simulations of inductive current perturbations to electron internal transport barriers in TCV,*

Proc. Joint Varenna-Lausanne International Workshop on Theory of Fusion Plasmas (Varenna, Italy), edited by J. W. Connor, O. Sauter and E. Sindoni (Societ Italiana di Fisica, Ed. Compositori, Bologna, 2004), p. 449.

1) **C. Zucca** *et al.*,

*Predator-prey phenomena in interchange mode turbulence,*

Proc. 31<sup>st</sup> EPS Conference on Plasma Phys. and Control. Fusion (London, UK), European Conference Abstracts (ECA) (Petit Lancy, Switzerland, 2004), Vol. **28G**, (2004) P-5.189.